UNIVERSITY OF CALIFORNIA

Santa Barbara

Heterogeneous Nonlinear Photonics

A dissertation submitted in partial satisfaction of the

requirements for the degree

Doctor of Philosophy

in

Electrical and Computer Engineering

by

Lin Chang

Committee in charge:

Professor John E. Bowers, Chair

Professor Larry A. Coldren

Professor Nadir Dagli

Professor Jon A. Schuller

March 2019

The dissertation of Lin Chang is approved.

_____

Larry Coldren

_____

Nadir Dagli

_____

Jon Schuller

_____

John Bowers, Committee Chair

March 2019

Heterogeneous nonlinear photonics

by

Lin Chang

ACKNOWLEDGEMENTS

During my 5 years' PhD time, I always feel very fortunate to work in the field of photonics, along with many excellent scientists and engineers. None of the work in this dissertation would have been possible without the suggestions and help from them.

I first need to thank my advisor, Prof. John Bowers. It is difficult to find a few sentences to fully acknowledge John. Without his limitless resource and fully support, I wouldn't be able to pursue any of the research and make any projects successful. Besides all the lessons I learned from him in research, the thing impresses me most is his skill as a great manager and successful businessman. The capability of him to transfer the research from lab to the level which can benefit the whole world is what I will be learning in my whole research career.

I also need to thank many other professors in ECE and material department at UCSB, particularly, my committee members, Prof. Larry Cold, Prof. Nadir Dagli and Prof. Jon Schuller. The knowledge I learned from their classes is the fountain of new ideas and most useful tools for me to explore new areas.

During my PhD, I was working in a big Darpa's project, DODOS, so that I got the chance to work with many leading groups and experts in this field. I give my special acknowledgement to Dr. Scott Papp at NIST. Through the discussions with whom, I gained a deeper understanding of nonlinear photonics and got lots of inspiration. The collaborations with Prof. Kippenberg's group at EPFL, Dr. Kartik's team at NIST and Prof. Kerry Vahala's group at Caltech are all very fruitful and will continue in the future.

It is a very nice experience to work in Bowers' group, where I met many brilliant people and made friends with them. Tony and Minh joined the group at the same time with me, went

through all the phases of PhD and finally we all graduated at the same time. There is nothing more valuable than the experience of learning and encouraging each other among friends over such a long journey. Chong, Chao, Xinru and Paolo gave me a lot of favor, both in life and research. I have learned many thing from and enjoyed spending time with each of the rest of you: Mike, Daryl, Sudha, Jared, Alan, Jock, Di, Geza, Molly, Emmett, Tin, Alex, Eric, Justin, Yichen, Akhilesh, Robert, Aditya M, Christos, Daehwan, Songtao, Sahngjian, Nick, Yating, Kaiyin, Andy N., Aditya J, Jenny, Ruilin, Chen, Joel, Noelle, Mario, Jinxi, Daisuke.

Good research is always accomplished by collaborations. I am very proud of the team in our group working on nonlinear photonics. Andy B. gave me lots of help and constructive suggestions in both my LNOI and GaAsOI work. Xiaowen, as my intern, assisted in the simulation and measurement, which sped up the progress a lot. Recently, Weiqiang and Warren also got involved in and are trying to expand our research. I would give the credit to the whole team's efforts.

We work very closely with Prof. Dan Blumenthal's group. They did fantastic work and I really learned a lot from Sarat, as well as other group members: Michael, Rena, Grant, Zhenlin, Taran, Micheal, Mark.

For the research of photonics, the most important part is always the fabrication. I give my special thanks to Jon Peters, who always finish the process for us very efficiently with high quality. MJ solved many difficult problems for us in fabrication based on his rich experience. Alfredo taught me many useful lessons in cleanroom.

The Nanofab staff are fundamental to any fabrication-heavy thesis. Thank you Tom, Brian, Aidan, Don, Demis, Tony, Mike, Mike, Luis, Ning, Biljana, Bill, and Brian.

For the hero behind the scenes, Tina and Ceanna helped us deal with many paper works. Staff in IEE and ECE did great job in organizing events and saved us tremendous amount of time by handling the purchase and packages.

Finally, the most important ones, my father and mother. It was indeed a long time of the whole PhD time, during which there were many hard times for me. They always support me no matter what happens, both mentally and financially. Without them, I wouldn't have been able to overcome those difficulties and finally make this happen.

Curriculum Vitæ

Lin Chang

EDUCATION

Bachelor of Engineering, Optical Science and Technology department, Shandong University, June 2013

Master of Science, Electrical and Computer Engineering department, University of California, Santa Barbara, June 2015

Doctor of Philosophy, Electrical and Computer Engineering, University of California, Santa Barbara, March 2019 (expected)

JOURNAL PUBLICATIONS

Lin Chang, Andreas Boes, Paolo Pintus, Jon D. Peters, MJ. Kennedy, Xiaowen Guo, Supeng Yu, Nicolas Volet, Scott B. Papp, John E. Bowers, "*Strong frequency conversion in heterogeneous integrated GaAs resonators*", APL Photonics, Volume 4, Issue 3 (2019) **(Editor's pick)**

Lin Chang, Andreas Boes, Xiaowen Guo, Daryl T. Spencer, MJ. Kennedy, Jon D. Peters, Nicolas Volet, Jeff Chiles, Abijith Kowligy, Nima Nader, Daniel D. Hickstein, Eric J. Stanton, Scott A. Diddams, Scott B. Papp, John E Bowers, "*Heterogeneously integrated GaAs waveguides on insulator for efficient frequency conversion*", Laser & Photonics Reviews, Volume 12, Issue 10, (2018) **(Inside cover)**

Lin Chang, Y Li, N Volet, L Wang, J Peters, JE Bowers, "*Thin film wavelength converters for photonic integrated circuits*", Optica, Vol. 3, Issue 5 (2016)

Lin Chang, Martin HP Pfeiffer, Nicolas Volet, Michael Zervas, Jon D Peters, Costanza L Manganelli, Eric J Stanton, Yifei Li, Tobias J Kippenberg, John E Bowers, "*Heterogeneous integration of lithium niobate and silicon nitride waveguides for wafer-scale photonic integrated circuits on silicon*", Optics Letters, Volume 42, Issue 4 (2017)

Daryl T Spencer, Tara Drake, Travis C Briles, Jordan Stone, Laura C Sinclair, Connor Fredrick, Qing Li, Daron Westly, B Robert Ilic, Aaron Bluestone, Nicolas Volet, Tin Komljenovic, **Lin Chang**, Seung Hoon Lee, Dong Yoon Oh, Myoung-Gyun Suh, Ki Youl Yang, Martin HP Pfeiffer, Tobias J Kippenberg, Erik Norberg, Luke Theogarajan, Kerry Vahala, Nathan R Newbury, Kartik Srinivasan, John E Bowers, Scott A Diddams, Scott B Papp, "*An optical frequency synthesizer using integrated photonics*", Nature, Volume 557, Issue 7703, (2018)

Leiran Wang, **Lin Chang (co-first author)**, Nicolas Volet, Martin HP Pfeiffer, Michael Zervas, Hairun Guo, Tobias J Kippenberg, John E Bowers, "*Frequency comb generation in the green using silicon nitride microresonators*", Laser & Photonics Reviews, Volume 10, Issue 4 (2016)

Andreas Boes, Bill Corcoran, **Lin Chang**, John Bowers, Arnan Mitchell, "*Status and Potential of Lithium Niobate on Insulator (LNOI) for Photonic Integrated Circuits*", Laser & Photonics Reviews, Volume 12, Issue 4, (2018)

Daniel D Hickstein, Grace C Kerber, David R Carlson, **Lin Chang**, Daron Westly, Kartik Srinivasan, Abijith Kowligy, John E Bowers, Scott A Diddams, Scott B Papp, "*Quasi-Phase-Matched Supercontinuum Generation in Photonic Waveguides*", Physical review letters, Volume 120, Issue 5 (2018)

Nicolas Volet, Alexander Spott, Eric J Stanton, Michael L Davenport, **Lin Chang**, Jon D Peters, Travis C Briles, Igor Vurgaftman, Jerry R Meyer, John E Bowers, "*Semiconductor optical amplifiers at 2.0 micron wavelength on silicon*", Laser & Photonics Reviews, Volume 11, Issue 2 (2017)

Michael L Davenport, **Lin Chang**, Duanni Huang, Nicolas Volet, John E Bowers, "*Heterogeneous Photonic Integration by Direct Wafer Bonding*", ECS Transactions, Volume 75, Issue 9 (2016) **(invited)**

CONFERENCE PUBLICATIONS

Lin Chang and John Bowers, "*Aluminium Gallium Arsenide on insulator platform for efficient nonlinear processes*", Nonlinear Optics (NLO), (2019) **(invited talk)**

Lin Chang, Andreas Boes, Paolo Pintus, Jon Peters, MJ Kennedy, Warren Jin, Xiaowen Guo, Supeng Yu, Scott B. Papp, John Bowers, "*High Q resonators in the GaAs and AlGaAs on insulator platform*", Conference on Lasers and Electro-Optics (CLEO), SF2I.2, (2019)

Lin Chang, Andreas Boes, Paolo Pintus, Xiaowen Guo, Jon Peters, MJ. Kennedy, Xiaowen Guo, Nicolas Volet, Supeng Yu, Scott A. Diddams, Scott B. Papp, John E. Bowers, "*High efficiency SHG in heterogenous integrated GaAs ring resonators*", IEEE Photonics Conference (IPC), (2018) **(postdeadline)**

Lin Chang, Xiaowen Guo, Daryl T. Spencer, Jeff Chiles, Abijith Kowligy, Nima Nader, Daniel Hickstein, MJ. Kennedy, Andreas Boes, Nicolas Volet, Scott A. Diddams, Scott B. Papp, John E. Bowers, "*A gallium arsenide nonlinear platform on silicon*", CLEO, STu3F. 5, (2018) **(invited talk)**

Lin Chang, Martin HP Pfeiffer, Nicolas Volet, Michael Zervas, Jon D Peters, Costanza L Manganelli, Eric J Stanton, Yifei Li, Tobias J Kippenberg, John E Bowers, "*A lithium niobate-Si3N4 platform on silicon by heterogeneous wafer bonding*", CLEO, SM4O.2, (2017)

Lin Chang, Nicolas Volet, Yifei Li, Jon Peters, John E Bowers, "*A thin-film PPLN waveguide for second-harmonic generation at 2 micron*", IPC, WE2.4, (2016)

Lin Chang, Yifei Li, Nicolas Volet, Leiran Wang, Jon Peters, John E Bowers, "*Sub-micron periodically-poled lithium niobate waveguide for integrated nonlinear optics*", CLEO, STh3P. 2, (2016)

ABSTRACT

Heterogeneous Nonlinear Photonics

by

Lin Chang

Nonlinear optics is the study of the interaction between light and matters. It originated from the first observation of second harmonic generation by Franken and coworkers in 1961. Since then, interest in this area has been continuously growing. Now nonlinear optics has been extended to numerous applications such as diversified lasers, communications, sensing and different quantum technologies, in both industry and the research of fundamental science.

Recently, with many breakthroughs in the demonstrations of nonlinear devices at chip-scale, the area of nonlinear photonics has evolved and went through rapid progress. For example, frequency comb generation, the Nobel-winning technology, has been enabled by micro-resonators on multi photonic platforms. Other advanced nonlinear processes, such as second harmonic generation, optical parametric oscillation, as well as many opto-mechanics processes, have also been realized in different on-chip devices.

However, even though those demonstrations open up many new possibilities for nonlinear applications by using photonics approach, currently the nonlinear photonic technologies still have some major problems at both individual device and system level. The efficiency of nonlinear process on chip is still not high enough to enable strong frequency conversion at the pump power level of integrated lasers, which is usually around a few milli-watts. Another

challenge is that current nonlinear devices are not integration compatible with other active photonic components, which prevents the realization of fully integrated nonlinear systems on chip.

To address those problems, we proposed and developed the heterogeneous integration technology for nonlinear photonics. Heterogeneous integration has been widely used in silicon photonics to transfer III-V or other material layers on Si waveguides by wafer- or die-bonding. Introducing it into nonlinear photonics enables the access to high quality single crystalline films, which can have much higher nonlinearities compared to the materials used for previous nonlinear devices. Furthermore, it also offers the possibilities to integrate nonlinear and active photonic components together, which paves the way to the revolutionary nonlinear photonic integrated circuits (PICs) in the future.

This thesis presents two nonlinear platforms we developed based on heterogeneous integration: the (Al)GaAs on insulator platform as well as the lithium niobate ($LiNbO_3$) on insulator platform. Multiple efficient nonlinear processes on those platforms, including second harmonic generation by waveguides and micro-resonators, as well as frequency comb generation, have been realized. We also demonstrated CMOS compatible platforms with nonlinear functionalities by heterogeneously integrating silicon nitride with either (Al)GaAs or $LiNbO_3$. The design considerations, fabrication processes, and the performance of each nonlinear device are discussed in details. Furthermore, we discuss a system level demonstration, an optical frequency synthesizer based on efficient nonlinear devices, and the possibility to fully integrate those nonlinear systems in PICs based on the heterogeneous integration technology.

TABLE OF CONTENTS

1. Introduction.....1

1.1. Nonlinear photonics.....1

1.2. Heterogeneous integration.....2

1.3. Second order nonlinear process.....3

1.4. Third order noninear process.....4

1.5. Nonlinear photonic integrated circuits.....5

1.6. Overview of thesis.....7

Reference.....7

2. Theory.....12

2.1. Second order nonlinear process.....12

2.1.1. Coupled mode equations.....12

2.1.2 Phase match conditions.....16

2.1.3 Second harmonic generation.....17

2.1.4 Resonators for SHG and OPO.....19

2.2. Third order nonlinear process.....22

2.2.1. Physics of Kerr-comb formation process.....22

2.2.2. Nonlinear coupled mode equation.....23

2.2.3. Dissipative Kerr solitons.....25

2.3. Summary.....27

Reference.....27

3. Lithium niobate on insulator platform.....29

3.1. Background 29
3.2. Platform design 31
3.3. Fabrication 33
3.3.1. Heterogeneous bonding 34
3.3.2. Waveguide process 34
3.3.3. Thin film lithium niobate poling 36
3.4. Low loss LNOI waveguides 40
3.5. PPLN waveguides for frequency conversion 41
3.6. Summary and outlook 45
Reference 46
4. (Aluminium) Gallium Arsenide on insulator platform 48
4.1. Background 48
4.2. Fabrication 51
4.2.1. Heterogeneous bonding 51
4.2.2. (Al)GaAsOI waveguide process 53
4.2.3. Surface passivation 54
4.3. Waveguides for SHG 55
4.4. Micro-resonators for SHG and OPO 63
4.5. Micro-resonators for frequency comb generation 71
4.6. High Q resonators 74
4.7. Summary and outlook 80
Reference 81
5. CMOS compatible nonlinear platforms 85
5.1. Background 85

5.2. Silicon nitride nonlinear platform 86
5.2.1. Introduction 86
5.2.2. Frequency comb generation 87
5.2.3. Supercontinuum generation 96
5.3. Si_3N_4-$LiNbO_3$ platform 101
5.4. Si_3N_4-GaAs platform 107
5.5. Summary and outlook 110
Reference 111
6. Nonlinear photonic systems 113
6.1. Background 113
6.2. Optical frequency synthesizers based on integrated photonics 114
6.2.1. Introduction 114
6.2.2. Experiments 116
6.2.3. Devices 125
6.2.4. Integration of the system 129
6.3. Other nonlinear photonic systems 130
6.4. Summary and outlook 131
Reference 131
7. Conclusions 135
7.1. Review 135
7.2. Prospects 136

LIST OF FIGURES

Figure. 2.1: SHG under different phase match conditions (upper) and the schematic drawing for periodic domain inversion for QPM. 16

Figure. 2.2: Schematic of coupling into and out of a resonator. 19

Figure. 2.3: Universal Kerr-comb formation processes. 23

Figure. 3.1: Schematic drawing of different LN waveguides 30

Figure. 3.2: (a) Schematic cross-section of the waveguide; (b) and (c): Simulated fundamental TE mode profiles of the waveguide at 1550 nm and 775 nm, respectively..... 31

Figure. 3.3: Simulated effective waveguide area (*Aeff*) for the fundamental TE mode at 775 nm and at 1550 nm, and *Seff* between these two modes as a function of the SiN ridge width. 33

Figure. 3.4: SEM image taken after the sample is polished and then dipped in BHF for 1 min for improving the contrast..... 35

Figure. 3.5: (a)-(d) Schematic illustration of the evolution of inverted domain using a long poling pulse; (e)-(h) Schematic illustration of the evolution of inverted domains using multi-pulse waveform with short pulse duration. 36

Figure. 3.6: (a) Schematic of cross-section of the device obtained after ion milling to visualize the periodically-poled region; (b) Top-view micrograph of the cross-section of a poled device after 10 min 48 % HF etch at room temperature. The dashed line corresponds to the cross-section in which the bright part is the poled area; (c) SEM image of inverted domain. 38

Figure. 3.7: Processing flow of PPLN waveguide fabrication. 39

Figure. 3.8: Transmission spectrum for a 5-mm long waveguide whose SiN ridge is 2 μm wide and 400 nm tall on a 700 nm thick LN film. 41

Figure. 3.9: PPLN waveguide characterized as a wavelength converter using SHG: (a) normalized efficiency as a function of the pump wavelength; (b) peak generated SH power under different pump powers (red crosses), compared to theoretical predictions from (S7), assuming ηnor = 160 % $W^{-1} \cdot cm^{-2.}$ 42

Figure. 3.10: Effective index difference between the TE waveguide mode and the TM slab mode. Waveguide with $\Delta n_{eff} < 0$ can suffer from lateral leakage. 43

Figure. 3.11: (a) fundamental and SHG power as a function of the pump wavelength; (b) SHG efficiency and fitted curve. 44

Figure. 4.1: Process flow for GaAs waveguide device fabrication. 52

Figure. 4.2: Bonded GaAs thin film on SiO2 after substrate removal (left), and the AFM results for surface roughness before and after bonding. 53

Figure. 4.3: SEM image of GaAs waveguide with SiO2 hard mask on top after GaAs etch (left) and SEM image of the waveguide cross section (right). 54

Figure. 4.4: Nonlinear waveguide design: (a) Waveguide cross section geometry; (b) Mode distribution of fundamental TE mode at 2 μm wavelength; (c) Mode distribution of fundamental TM mode at 1 μm wavelength. 55

Figure. 4.5: (a) Required waveguide width to achieve phase matching for SHG at a fundamental wavelength of 2 μm as a function of the GaAs thickness; (b) Effective indices of the pump and SH modes as a function of the waveguide width for a GaAs thickness of 150 nm at wavelengths of 2 μm and 1 μm. 56

Figure. 4.6: Schematic of the SH characterization setup. 57

Figure. 4.7: Experimental results: (a) SHG and pump power as a function of the pump wavelength for a 1.4-mm-long waveguide with inverse taper input; (c) Single pass conversion efficiency extracted from (a). 58

Figure. 4.8: Dependence of phase matching wavelength on the GaAs waveguide (a) thickness and (b) width; (c) Phase matching wavelength of waveguides with different widths - the black diamonds represent measurements, the blue dashed line represents simulation results; (d) Calculated efficiency over propagation loss of SH light for 1.4-mm-long waveguide, assuming 2 dB/cm loss at pump wavelength. 60

Figure. 4.9: (a) Cross section of GaAs on insulator waveguide; (b) and (c) electric field distributions for fundamental TE mode at a wavelength of 2 μm and TM mode at a wavelength of 1 μm; (d) schematic structure of ring resonator with pulley coupler. 63

Figure. 4.10: Experimental results and analysis: (a) pump and SHG spectrum for the ring resonator, the embedded figure shows the zoomed in resonance and fitting curve; (b) dependence of external SHG conversion efficiency on the pump power, experimental results and calculation from Eq. 5, the embedded figure shows the SHG power as a function of the pump power, experimental results are compared to the case of no depletion (red dash line).65

Figure. 4.11: Energy bandgap of AlGaAs [31]. 71

Figure. 4.12: (a) Schematic drawing of the waveguide for comb generation; (b) Simulated dispersion results under different waveguide widths. 72

Figure. 4.13: (a) SEM image of the resonator; (b) Spectrum of the resonace for the resonator by using old fabrication process; (b) Frequency comb generation under 4 mW pump power inside bus waveguide. 73

Figure. 4.14: Frequency comb generation by the resonator with optimized fabrication process. Green and red plots correspond to pump power of 1 mW and 220 μW inside bus waveguide. The inset is the resonance transmission spectrum. 74

Figure. 4.15: (a) Schematic drawing of waveguide cross section; (b) Simulated effective index contour for GaAs waveguides; (c) Simulated bending loss for GaAs waveguide in this work..... 75

Figure. 4.16: Characteristic images of the device: (a) Microscopic top view of the resonator; (b) SEM image of the cross section of the Al0.2Ga0.8As waveguide. 77

Figure. 4.17: Experimental results: (a) Resonance of GaAs on insulator resonator; (b) Zoomed in transmission spectrum the resonators in (a). 77

Figure. 4.18: (a) Experimental results of the resonance of Al0.2Ga0.8As on insulator resonator; (b) Calculated waveguide loss for SOI waveguide (blue line) and AlGaAs on insulator waveguide (orange line) as a function of power intensity taking TPA at 1550 nm into account..... 78

Figure. 5.1: (a) Top-view schematic and (b) SEM picture of the ring microresonator with the bus waveguide. The features visible in the central and the top left parts of (b) are remains of the stress relax checkerboard pattern. (c) Transmission spectrum measured at low EDFA power (−13 dBm) for a TE input polarization, and (d) fitting (in red) of the resonance near 192.8 THz (corresponding to a wavelength of ∼1555 nm). (e) Fitting (in red) of a resonance measured for a TM input polarization. 87

Figure. 5.2: Simulated spectra of the second-order dispersion D2/(2π) for the fundamental TE (in red) and TM (in black) modes. The vertical dashed line indicates the 1.55-μm wavelength. 88

Figure. 5.4: Generation process of the IR Kerr comb (left column) and the simultaneously emitted GLC (right column), by gradually tuning the TE-polarized IR pump to the resonance near fp ∼= 191.9 THz. 91

Figure. 5.5: (a) IR Kerr comb generated with a TE pump and (b) the corresponding GLC with 18 spectral lines. In (b), the inset shows a photograph of the probed device. The pump frequency fp = 191.7 THz and both IR and green combs have FSR ∼= 992.6 GHz. 93

Figure. 5.6: (a) IR Kerr comb generated with a TM pump and (b) the corresponding GLC with 30 spectral lines. In (b), the inset shows a photograph of the probed device. 95

Figure. 5.7: (a) Quasi-phase-matching of supercontinuum generation in on-chip photonic waveguides can be achieved via waveguide-width modulation; (b) When the effective index of the soliton in the TE00 mode ("soliton index") intersects the effective index of a waveguide mode (black curves), phase matching to dispersive waves is achieved (green squares) and a spectrum with several peaks (c) is generated. The periodic modulation of the waveguide can enable numerous QPM orders, both positive and negative, which can allow QPMDW generation to the fundamental mode and to higher-order modes (circles), producing a spectrum with many peaks (d). Note that the index curvature is exaggerated to better show phase matching. 98

Figure. 5.8: (a) The spectrum of supercontinuum generation from a width-modulated waveguide as a function of input power. The arrow indicates the QPM DW to the TE20 mode. (b) The effective refractive index of various modes of the waveguide as a function of wavelength. When the index of the soliton including a first order grating effect from the 6.2-μm width-modulation (red line) crosses the TE20 mode, a QPM DW is generated. (c) The calculated spectral location of the TE20 QPM DW as a function of the width-modulation

period is in agreement with experimental results. The slight difference in slope may arise from irregularities in the dimensions of the waveguides. 100

Figure. 5.9: Schematic structure of tapered mode converter connecting the two types of waveguides. The top and bottom areas show schematics of the waveguide cross-sections and simulated profiles of the fundamental TE modes at 1540 nm. Inset is the simulated confinement factor in the LN layer for LN-Si3N4 hybrid waveguides calculated as a function of the Si3N4 rib width. 102

Figure. 5.10: Fabrication procedure for the LN-Si3N4 platform. 103

Figure. 5.11: (a) SEM cross-section of the Si3N4 waveguide. (b) Roughness testing results after SiO2 deposition and repolishing. (c) Top-view of integrated LN- Si3N4 chip. (d) Bonded area after substrate and BOX layer removal. 105

Figure. 5.12: Spectra of total insertion loss for the reference waveguide (blue) and heterogeneous waveguide (red). 106

Figure. 5.13: (a) illustrates the device design of the integration of a GaAs waveguides for frequency doubling onto SiN waveguides for the optical frequency comb generation and the transitioning between the layers. (b) and (c) present the results for the generated frequency comb of the SiN ring resonator and the GaAs frequency doubler on the same chip, respectively. 108

Figure. 6.1: **Accurate optical synthesis with an integrated laser and DKS dual-comb system.** a, Conceptual integrated optical-frequency synthesizer with digital control and f–2 f stabilization, using the microcombs and tunable laser of this work. PD, photodetector. b, Our optical synthesizer is composed of an integrated tunable laser and chip-based Kerr-comb generators. Green boxes indicate the tabletop subsystems including the chips, and how they connect. The CW pumping laser for some experiments is a second integrated laser;

see Methods. The tunable laser is synthesized by phase-locking to the stabilized combs, using a look-up table (LUT) and FPGA. QPSK, quadrature phase shift key modulator. c, Optical spectra of the laser across 32 nm. d, e, Measurements of the synthesizer output as it is stepped. The data indicate the deviation between the synthesizer output vout and its setpoint for mode-hopping across the 22-GHz SiO2 modes (d) and for application of precise frequency steps of 15.36Hz (e). f, Scanning electron microscope (SEM) image of the heterogeneous III–V/Si tunable laser with false colour electrodes (yellow) and waveguides (blue). g, Photograph of the SiO2-based wedge microresonator. h, SEM image of the Si3N4 THz resonator with false colour imposed on the waveguide regions. 116

Figure. 6.2: **Optical spectra of the integrated devices.** a, Schematic diagram of spectral combination with the integrated devices, and the frequency chain used to multiply the 10-MHz clock to the optical domain. b, Combined spectrum of the SiO2 22-GHz wedge microcomb and the heterogeneously integrated iii–v/Si tunable laser in the telecommunication C-band. c, Combined spectrum of the octave-spanning Si3N4 THz microcomb and the 22-GHz SiO2 wedge microcomb, as measured on two optical spectrum analysers. 119

Figure. 6.3: **Stable optical synthesis with out-of-loop verification.** a, Tunable laser locking, and frequency counting with the auxiliary comb. HNLF, highly nonlinear fibre. b, Measured overlapping Allan deviation (ADEV) and modified Allan deviation (MDEV) of the frequency synthesizer. In comparing 10-ms counter-gate time acquisitions, the $1/\tau$ slope is consistent with a stable, phase-locked synthesizer, and the histograms of 500 s of data (inset for relative mode m=−28 only) show a Gaussian profile. Error bars indicating 95% confidence intervals are derived using flicker noise estimates. c, Table of nominal frequencies and uncertainty at 200 s as the synthesizer is stepped across the C-band. d, Overview of the accuracy and precision of the synthesizer frequency. The ADEV at 100 s is used to estimate

the uncertainty of each synthesizer output, and the weighted mean of the seven data points is reported with a 95% (t distribution) confidence interval. 121

Figure. 6.4: **Arbitrary control of the optical-frequency synthesizer.** a, Stepwise control of the tunable-laser offset phase-lock to the DKS comb and frequency counting. b, Deviation between the synthesizer output vout and constant setpoint for 500 s at a 10-ms gate time. c, Bidirectional linear ramp of the synthesizer via step control of the laser offset PLL setpoint (100-ms gate). d, Arbitrary frequency control of the synthesizer across 40 frequency setpoints to write “NIST”. A 30-ms gate time is used to oversample each frequency setpoint by 5 (150-ms pause per point), and every fifth data point is displayed.....124

Figure. 6.5: **Integration of an optical frequency synthesizer.** (a) Schematic drawing of the system; (b) Interposer chip combing multi photonic components together; (c) A compact optical frequency synthesizer in a package. 130

LIST OF TABLES

Table 4.1. Comparison of nonlinear optical coefficients and mode sizes of waveguides among commonly used nonlinear materials. 49

Chapter 1

Introduction

1.1. Nonlinear photonics

The field of nonlinear optics has a long history since the discovery of second-harmonic generation by Peter Franken in 1961 [1], shortly after the first demonstration of the laser. Through more than half a century of development, it has become one of the most important branches of optics. Now, nonlinear optics is the backbone of numerous fields, ranging from fundamental studies of light-matter interaction [2] to applications such as optical signal processing in communication [3] and nonlinear microscopy [4] .

Recently, an important turning point of nonlinear optics is the transfer from bench-top, bulky devices to photonics chip level components, leading to advances in the new area of nonlinear photonics [5]. By applying the fabrication technology in photonics, nonlinear devices can be made on chip, with micron or even sub-micron scales. Besides all of the benefits brought by photonics, e.g., the footprint, scalable and the low-cost production [6], the nonlinear photonic devices also gain a significant improvement in terms of performance [7], due to the much smaller mode volume of the waveguide for enhancing nonlinear efficiencies, and the freedom for engineering the geometry of waveguides for different nonlinear processes.

One of the main efforts of the developments in nonlinear photonics is frequency comb generation based on third order nonlinear ($\chi^{(3)}$) effect by micro-resonators or supercontinuum waveguides [8], which has been realized on multiple material platforms such as SiO_2, Si_3N_4, Si and on. Another essential direction is frequency conversions based on the second order

nonlinear ($\chi^{(2)}$) processes [9]. This thesis will mainly focus on the discussions and demonstrations in those two directions. However, other important fields of nonlinear photonics, such as the Stimulated Brillouin Scattering [10], Raman effect [11], high harmonic generation [12], are also seeing great progresses and will play significant roles in the future.

1.2. Heterogeneous integration

Heterogeneous integration is to combine separately manufactured components into a higher-level assembly which can provide enhanced functionality and improved operating characteristics [6]. It originated from electronics and then was widely applied in photonics in the last decade. Previously, the main motivation of it for photonics was in the silicon photonics industry [13]. This is because, even though silicon photonics has great potential to bring large scale, high volume and cost reduction of silicon manufacturing to photonic components, the most important photonic component—light source—is missing in photonic integrated circuits (PICs) on pure silicon-on-insulator (SOI) platform. By heterogeneously integrating III-V semiconductor material onto SOI waveguide, electrically pumped efficient light emitting devices, as well as other active photonic components, can be integrated in silicon photonics.

The key method of heterogeneous photonics integration is wafer or die bonding [14], which offers a great advantage that different epitaxial stacks can be integrated together on the same wafer and further processed simultaneously. Besides the III-V materials, other exotic media, such as $LiNbO_3$ [15], diamond [16], and Ce:YIG [17], can also be added into PICs, bringing advanced functions in high speed modulator, quantum application and optical isolators.

The motivation of applying heterogeneous integration in nonlinear photonics first originated from the demand of introducing $\chi^{(2)}$ based process into photonics [5]. The difficulty of achieving that comes from the fact that usually only materials with noncentrosymmetric crystal structures have second order nonlinearity, which excludes most of commonly used photonic material platforms such as SOI, Si_3N_4, silica and so on. Nonlinear materials with strong $\chi^{(2)}$ like GaAs, GaP, GaN, usually have to be grown on native substrate [18], which prevents the realization of high index contrast which is necessary for nonlinear applications.

Heterogeneous integration offers a good solution to address this problem. Besides the advantage of introducing high quality thin film crystalline, great flexibility can be obtained in choosing the waveguide and cladding materials because there is no limitation of lattice match at the interface between different materials. Early work were done by bonding Lithium niobate film onto SiO_2 for frequency conversion and constructing modulators [19]. This area started to boom after the commercialization of wafers with such stacks by several companies [7]. More details about the development and our demonstration of the lithium niobate on insulator (LNOI) platform are in Chapter 3. Recently, driven by the demand for ultra-efficient nonlinear processes, as well as integration between active and nonlinear devices, III-V semiconductor on insulator platforms, especially based on (Al)GaAsOI [20], have been demonstrated and hold the promise for nonlinear PICs in the future, which will be discussed in Chapter 4 in this thesis.

1.3. Second order nonlinear process

The second order nonlinear effect is one of the strongest optical nonlinear effect. It includes sum frequency generation, differential frequency generation, optical parametric

oscillation and so on [21], and has been widely applied to a broad range of applications. In quantum optics, the second-order nonlinearity is often used for generating entangled photon pairs by spontaneous parametric down-conversion (SPDC) and for providing continuous variables entanglement in an OPO configuration [22]. In classical photonics, it plays key roles in various applications, such as nonlinear microscopy [4], optical frequency references [23] and light source at various wavelength [24], among others.

Important materials for $\chi^{(2)}$ based processes include dielectrics such as $LiNbO_3$, BBO, KTP, and compound semiconductors like (Al)GaAs and GaP, which have strong nonlinear coefficients [21]. Previously, most of the nonlinear devices are on native substrates, where the waveguides suffered from weak index contrast and thus large mode size on the order of tens of μm^2 [25]. The low photon intensity in such big waveguides limited the efficiency of the frequency conversion.

Another important requirement for efficient second order nonlinear effect is the phase match condition. One commonly used approach is birefringent phase match, including type I and type II [21]. Another widely applied method is quasi-phase matching, usually based on periodic domain inversion, which has been applied to lithium niobate, BBO and (Al)GaAs by either periodic poling technology or regrowth [26], [27]. For integrated $\chi^{(2)}$ waveguides with small mode volume, to achieve phase-match is usually more challenging compared to bulky waveguides due to the stronger dispersion.

1.4. Third order nonlinear process

Third order nonlinear effect is also called optical Kerr effect. It occurs when intense light propagates in mediums, whose refractive index get modified by the intensity of the light beam [21]. The time- and frequency- dependent refractive index change leads to the effect of self-

phase modulation and Kerr lensing. And among different frequencies of light beam, it also causes cross-phase modulation.

A particularly interesting area based on Kerr effect, which has witnessed remarkable breakthroughs in last decades, is the development of frequency comb generation on chip, either by micro-ring resonators or supercontinuum waveguides [8]. Those compact, chip-scale comb sources have dramatically extended the applications in photonics, such as terabit optical coherent communications [28], optical frequency synthesizers [23], dual-comb spectroscopy [29] and on-chip optical atomic clocks [30].

So far, frequency comb generation has been demonstrated in different material platforms. Specially, the silica and silicon nitride micro-resonators are most commonly used [31], [32]. Efficient comb generation pumped at the power level of few to tens of milliwatts can be achieved, though the requirement of quality factor for those resonators is strict, usually beyond the order of millions. This adds difficulties to the fabrication and makes them not compatible with industry level massive production at low cost.

Heterogeneous integration provides a good solution to address this problem by introducing highly nonlinear materials. For example, compound semiconductor materials, e.g. AlGaAs, usually have strong third order nonlinear coefficients which are orders of magnitude higher than dielectric insulators [21]. Because of this, the quality factor required for micro-resonator based on those semiconductors can be dramatically relieved, and the fabricated can be greatly simplified as well.

1.5. Nonlinear photonic integrated circuits

With the development of many advanced individual devices, the ultimate goal of nonlinear photonics is to implement the nonlinear components into PICs on the same chip, along with

all the other photonic devices. Such fully integrated nonlinear PICs will enable numerous new applications, and transition the nonlinear system to platforms which are scalable and at low cost. Furthermore, the integration will also lead to an improvement in terms of performance, due to the reduced coupling loss and facet reflections, which are critical to nonlinear processes.

However, there are big problems existing in current nonlinear platforms, which prevent the realization of fully integrated nonlinear devices. First, the power levels that are achievable with integrated lasers are usually not high enough to drive current on-chip nonlinear optical processes efficiently. Typical on-chip laser powers are in the order of tens of milliwatt or lower [6]. However, most demonstrated integrated nonlinear devices do not meet the efficiency requirements to work at these power levels. One example is OPOs. So far the lasing of an integrated OPO based on $\chi^{(2)}$ nonlinearity, which is pumped by an on-chip laser, has not been demonstrated due to the high threshold power requirements [18]. Another difficulty is that most nonlinear materials used for PICs are not compatible with the integrated active devices, either in design, fabrication, or integration. As a result, the nonlinear components are still far from being integrated together with lasers, amplifiers and photodetectors on the same chip, but have to be connected by either fiber coupling or chip-to-chip butt coupling.

Heterogeneous nonlinear photonics projects to solve all the problems mentioned above. The introduction of high quality nonlinear crystal can boost the efficiency of nonlinear process. In the meanwhile, because heterogeneous integration is not limited by the lattice match of the materials, active and nonlinear devices can be bridged on the same platform. Particularly, when using III-V semiconductor materials, the integration of nonlinear

waveguide and active layers can be accomplished at the same time, which offers the most promising approach to construct fully integrated nonlinear PICs in the future.

1.6. Overview of thesis

In this thesis, we focus on our developments in heterogeneous nonlinear photonics. In Chapter 2, theories of second and third order nonlinear process are discussed. Chapter 3 and 4 present two major nonlinear material platforms we developed based on heterogeneous integration, the lithium niobate on insulator (LNOI) and (aluminum) gallium arsenide on insulator ((Al)GaAsOI) platforms, respectively. State of the art nonlinear devices for second harmonic generation and frequency comb generation are presented. Chapter 5 shows the developments of CMOS compatible nonlinear platforms by using heterogeneous integration. Chapter 6 takes one of our system level demonstrations, optical frequency synthesizer as an example, to illustrate how the nonlinear system works based on integrated photonics. Broader areas of the applications and outlook for nonlinear PICs in the future are also discussed.

References

[1] P. A. Franken, A. E. Hill, C. W. Peters, and G. Weinreich, "Generation of Optical Harmonics," *Phys. Rev. Lett.*, vol. 7, no. 4, pp. 118–119, Aug. 1961.

[2] G. Günter *et al.*, "Sub-cycle switch-on of ultrastrong light–matter interaction," *Nature*, vol. 458, no. 7235, pp. 178–181, Mar. 2009.

[3] A. E. Willner, S. Khaleghi, M. R. Chitgarha, and O. F. Yilmaz, "All-Optical Signal Processing," *J. Light. Technol.*, vol. 32, no. 4, pp. 660–680, Feb. 2014.

[4] X. Chen, O. Nadiarynkh, S. Plotnikov, and P. J. Campagnola, “Second harmonic generation microscopy for quantitative analysis of collagen fibrillar structure,” *Nat. Protoc.*, vol. 7, no. 4, pp. 654–669, 2012.

[5] S. Fathpour, “Heterogeneous Nonlinear Integrated Photonics,” *IEEE J. Quantum Electron.*, vol. 54, no. 6, pp. 1–16, Dec. 2018.

[6] T. Komljenovic *et al.*, “Heterogeneous Silicon Photonic Integrated Circuits,” *J. Light. Technol.*, vol. 34, no. 1, pp. 1–1, 2015.

[7] A. Boes, B. Corcoran, L. Chang, J. Bowers, and A. Mitchell, “Status and Potential of Lithium Niobate on Insulator (LNOI) for Photonic Integrated Circuits,” *Laser Photonics Rev.*, vol. 12, no. 4, pp. 1–19, 2018.

[8] A. L. Gaeta, M. Lipson, and T. J. Kippenberg, “Photonic-chip-based frequency combs,” *Nat. Photonics*, vol. 13, no. 3, pp. 158–169, Mar. 2019.

[9] I. Breunig, “Three-wave mixing in whispering gallery resonators,” *Laser Photonics Rev.*, vol. 10, no. 4, pp. 569–587, 2016.

[10] N. T. Otterstrom, R. O. Behunin, E. A. Kittlaus, Z. Wang, and P. T. Rakich, “A silicon Brillouin laser.,” *Science*, vol. 360, no. 6393, pp. 1113–1116, Jun. 2018.

[11] X. Liu *et al.*, “Integrated continuous-wave aluminum nitride Raman laser,” *Optica*, vol. 4, no. 8, p. 893, Aug. 2017.

[12] D. D. Hickstein *et al.*, “Non-collinear generation of angularly isolated circularly

polarized high harmonics," *Nat. Photonics*, vol. 9, no. 11, pp. 743–750, Nov. 2015.

[13] T. Komljenovic, D. Huang, P. Pintus, M. A. Tran, M. L. Davenport, and J. E. Bowers, "Photonic Integrated Circuits Using Heterogeneous Integration on Silicon," *Proc. IEEE*, vol. 106, no. 12, pp. 2246–2257, Dec. 2018.

[14] M. L. Davenport, L. Chang, D. Huang, N. Volet, and J. E. Bowers, "(Invited) Heterogeneous Photonic Integration by Direct Wafer Bonding," *ECS Trans.*, vol. 75, no. 9, pp. 179–183, Sep. 2016.

[15] P. O. Weigel *et al.*, "Lightwave Circuits in Lithium Niobate through Hybrid Waveguides with Silicon Photonics," *Sci. Rep.*, vol. 6, no. 1, p. 22301, Apr. 2016.

[16] I. Aharonovich, A. D. Greentree, and S. Prawer, "Diamond photonics," *Nat. Photonics*, vol. 5, no. 7, pp. 397–405, Jul. 2011.

[17] D. Huang, P. Pintus, C. Zhang, Y. Shoji, T. Mizumoto, and J. E. Bowers, "Electrically Driven and Thermally Tunable Integrated Optical Isolators for Silicon Photonics," *IEEE J. Sel. Top. Quantum Electron.*, vol. 22, no. 6, pp. 271–278, Nov. 2016.

[18] M. Savanier *et al.*, "Near-infrared optical parametric oscillator in a III-V semiconductor waveguide," *Appl. Phys. Lett.*, vol. 103, no. 26, p. 261105, Dec. 2013.

[19] G. Poberaj, H. Hu, W. Sohler, and P. Günter, "Lithium niobate on insulator (LNOI) for micro-photonic devices," *Laser Photon. Rev.*, vol. 6, no. 4, pp. 488–503, Jul. 2012.

[20] A. K. Y. MINHAO PU, LUISA OTTAVIANO, ELIZAVETA SEMENOVA, "Efficient frequency comb generation in AlGaAs-on-insulator," *Optica*, vol. 3, no. 8, pp. 823–826, 2016.

[21] R. W. Boyd, *Nonlinear optics*. Burlington: Academic Press, 2008.

[22] J. U. Fürst *et al.*, "Low-threshold optical parametric oscillations in a whispering gallery mode resonator," *2011 Conf. Lasers Electro-Optics Eur. 12th Eur. Quantum Electron. Conf. CLEO Eur. 2011*, vol. 263904, no. December, pp. 2–5, 2011.

[23] D. T. Spencer *et al.*, "An optical-frequency synthesizer using integrated photonics," *Nature*, vol. 557, no. 7703, pp. 81–85, 2018.

[24] M. Savanier *et al.*, "Integrated cavity for a GaAs-based OPO," *CLEO Sci. Innov.*, p. JW4A.66, 2012.

[25] L. Scaccabarozzi, M. M. Fejer, Y. Huo, S. Fan, X. Yu, and J. S. Harris, "Enhanced second-harmonic generation in AlGaAs/Al_xO_y tightly confining waveguides and resonant cavities," *Opt. Lett.*, vol. 31, no. 24, p. 3626, Dec. 2006.

[26] K. Nakamura, J. Kurz, K. Parameswaran, and M. M. Fejer, "Periodic poling of magnesium-oxide-doped lithium niobate," *J. Appl. Phys.*, vol. 91, no. 7, pp. 4528–4534, Apr. 2002.

[27] K. L. Vodopyanov *et al.*, "Terahertz-wave generation in quasi-phase-matched GaAs," *Appl. Phys. Lett.*, vol. 89, no. 14, p. 141119, Oct. 2006.

[28] H. Hu *et al.*, “Single-source chip-based frequency comb enabling extreme parallel data transmission,” *Nat. Photonics*, vol. 12, no. 8, pp. 469–473, Aug. 2018.

[29] M.-G. Suh, Q.-F. Yang, K. Y. Yang, X. Yi, and K. J. Vahala, “Microresonator soliton dual-comb spectroscopy.,” *Science*, vol. 354, no. 6312, pp. 600–603, Nov. 2016.

[30] Z. L. Newman *et al.*, “Photonic integration of an optical atomic clock,” Nov. 2018.

[31] K. Y. Yang *et al.*, “Bridging ultrahigh-Q devices and photonic circuits,” *Nat. Photonics*, vol. 12, no. 5, pp. 297–302, May 2018.

[32] M. H. P. Pfeiffer, J. Liu, A. S. Raja, T. Morais, B. Ghadiani, and T. J. Kippenberg, “Ultra-smooth silicon nitride waveguides based on the Damascene reflow process: fabrication and loss origins,” *Optica*, vol. 5, no. 7, p. 884, Jul. 2018.

Chapter 2

Theory

2.1. Second order nonlinear process

In this section, the theory for second order nonlinear process is discussed. The coupled mode method is used to describe the nonlinear interactions including SHG/OPO process in both waveguide and resonators. Based on that the phase match condition is also derived, including both the concepts of quasi phase match (QPM) and model phase match (MPM).

2.1.1 Coupled mode equations

Considering a nonlinear medium, if there is a polarization $\vec{P}$ induced by the electric field of an optical wave $\vec{E}$. $\vec{P}$ can be expressed as [1], [2]:

$$\vec{P} = \varepsilon_0\{\chi^{(1)}\vec{E} + \chi^{(2)}\vec{E}\vec{E} + \chi^{(3)}\vec{E}\vec{E}\vec{E} + ...\} \tag{2.1.1}$$

Where ε_0 is the permittivity in vacuum, and $\chi^{(n)}$ correspond to the *n*-th order susceptibility tensor. $\chi^{(1)}$ is the linear response which determines the refractive index materials. $\chi^{(2)}$ determines the second order nonlinearity while $\chi^{(3)}$ is the third order nonlinear effect and so on. Here we focus on the second order polarization term $\vec{P} = \chi^{(2)}\vec{E}\vec{E}$, which means that three waves (ω_1, ω_2 and ω_3) get involved in this process. Such so-called three wave mixing processes include sum frequency generation (SFG) when $\omega_1 + \omega_2 = \omega_3$, and differential frequency generation (DFG) when $\omega_1 - \omega_2 = \omega_3$.

Generally, when calculating the second order nonlinear polarization term, a tensor *d* is introduced, which has a relation with $\chi^{(2)}$ as $d_{ijk} = \frac{1}{2}\chi^{(2)}_{ijk}$. The tensor of *d* can be expressed

as a 3×6 matrix due to the Kleinman symmetry [3]. Different crystal structures have different number of independent parameters in the matrix; details will be discussed later.

For simplicity, here we assume that all the modes have pure transverse field distribution. In waveguide, it means that the mode is either pure TE or pure TM. Then the electric field of the mode at one frequency ω can be written as:

$$\overrightarrow{E_\omega}(x,y,z,t)=\frac{1}{2}\{A(z)E(x,y)\exp[i(\omega t-\beta z)]+c.c.\} \tag{2.1.2}$$

In which *A(z)* represents the slowly varying amplitude, *E(x,y)* stands for the electrical field distribution of the mode, β is the wave vector and *c.c.* represents the complex conjugation.

For three wave mixing, usually two waves get involved and generate a new one. Thus the second order polarization can be written as:

$$\begin{aligned}
P^{(2)} &= \varepsilon_0 d_{eff}(\overrightarrow{E_{\omega 1}}+\overrightarrow{E_{\omega 2}})^2 \\
&= \varepsilon_0 d_{eff}(\frac{1}{4}A_1^2(z)E_1^2(x,y)e^{i(2\omega_1 t-2\beta_1 z)}+\frac{1}{4}A_2^2(z)E_2^2(x,y)e^{i(2\omega_2 t-2\beta_2 z)} \\
&+\frac{1}{2}A_1(z)A_2(z)E_1(x,y)E_2(x,y)e^{i((\omega_1+\omega_2)t-(\beta_1+\beta_2)z)} \\
&+\frac{1}{2}A_1(z)A_2^*(z)E_1(x,y)E_2^*(x,y)e^{i((\omega_1-\omega_2)t-(\beta_1-\beta_2)z)} \\
&+\frac{1}{2}A_1(z)A_1^*(z)E_1(x,y)E_1^*(x,y)+\frac{1}{2}A_2(z)A_2^*(z)E_2(x,y)E_2^*(x,y) \\
&+c.c.)
\end{aligned} \tag{2.1.3}$$

It can be found that for three wave mixing process, only one term in Eq. (2.1.3) contributes to the generation of wave at a certain frequency: the third term corresponds to SFG ($\omega_3=\omega_1+\omega_2$) and the forth term is related with DFG ($\omega_3=\omega_1-\omega_2$). The fact that those nonlinear polarizations are the origin of the generated new waves, indicates that the second order nonlinear behavior can be described by plugging the nonlinear polarization into the propagation equation of an electromagnetic wave:

$$\nabla^2 \vec{E} - \frac{1}{c^2}\frac{\partial^2}{\partial t^2}\vec{E} = \frac{1}{\varepsilon_0 c^2}\frac{\partial^2 \vec{P}^{(2)}}{\partial t^2} \tag{2.1.4}$$

where c is the speed of light in vacuum. Then the coupled mode equation can be derived by replacing $\vec{P}^{(2)}$ by the specific term in Eq. (2.1.3). Here we take the DFG as an example, assuming that ω_1 is the frequency of pump light, ω_2 and ω_3 are the frequency of signal and idler wavelength, respectively, then the coupled mode equations become the following form:

$$\begin{aligned}
\frac{\partial A_1}{\partial z} &= -\frac{\alpha_1}{2}A_1 - i\kappa_1 A_2 A_3 e^{+i\Delta\beta z} \\
\frac{\partial A_2}{\partial z} &= -\frac{\alpha_2}{2}A_2 - i\kappa_2 A_3^* A_1 e^{-i\Delta\beta z} \\
\frac{\partial A_3}{\partial z} &= -\frac{\alpha_3}{2}A_3 - i\kappa_3 A_2^* A_1 e^{-i\Delta\beta z}
\end{aligned} \tag{2.1.5}$$

Where α_i (i = 1, 2, 3) is the propagation loss of the waveguide at different wavelengths, respectively. The parameter of $\Delta\beta$ is defined as:

$$\Delta\beta = \beta_1 - \beta_2 - \beta_3 \tag{2.1.6}$$

And the coupling coefficient κ_i is expressed as:

$$\kappa_i = \frac{d_{eff}\omega_i}{cn_i} \bullet \frac{\iint E_1(x,y)E_2(x,y)E_3(x,y)dxdy}{\iint E_i^2(x,y)dxdy}, i = 1,2,3 \tag{2.1.7}$$

Eq. (2.1.5) can only be solved in the way of numerical integration. Here for simplicity, we consider the case where waveguide has no loss, and the pump power is undepleted, which also means that the power of generated wave is much lower compared to the pump. Assuming that $A_3(0) = 0$, then the solution can be simplified as:

$$
\begin{aligned}
A_1(L) &= A_1(0) \\
A_2(L) &= e^{i\frac{\Delta\beta}{2}L} A_2[\cosh gL + i\frac{\Delta\beta}{2g}\sinh gL] \\
A_3(L) &= -i\kappa_3 e^{-i\frac{\Delta\beta}{2g}L}\frac{1}{g}A_3(0)\sinh gL \\
g &= \sqrt{\kappa_2\kappa_3|A_1|^2 - (\frac{\Delta\beta}{2})^2}
\end{aligned}
\tag{2.1.8}
$$

Then based on the amplitude of the field, we can calculate the optical power:

$$
P_i = \frac{\varepsilon_0 c n_i |A_i|^2}{2}\iint E_i^2(x,y)dxdy \tag{2.1.9}
$$

At the position L of the wavelength for each wave, the power turns out to be:

$$
\begin{aligned}
P_1(L) &= P_1(0) \\
P_2(L) &= P_2(0)\cosh^2 gL \\
P_3(L) &= \frac{\omega_3}{\omega_2}\frac{1}{g^2}\eta_{norm}P_1(0)P_2(0)\sinh^2 gL
\end{aligned}
\tag{2.1.10}
$$

$$
g = \sqrt{\eta_{norm}P_1(0) - (\frac{\Delta\beta}{2})^2} \tag{2.1.11}
$$

$$
\eta_{norm} = \frac{2{d_{eff}}^2\omega_2\omega_3}{\varepsilon_0 c^3 n_1 n_2 n_3 S_{eff}} \tag{2.1.12}
$$

$$
S_{eff} = \frac{\iint E_1^2(x,y)dxdy\iint E_2^2(x,y)dxdy\iint E_3^2(x,y)dxdy}{(\iint E_1(x,y)E_2(x,y)E_3(x,y)dxdy)^2} \tag{2.1.13}
$$

Here η_{norm} is called the normalized efficiency, and S_{eff} is known as the effective cross section. The absolute conversion efficiency of the DFG is defined as:

$$
\eta_{DFG} = \frac{P_3}{P_1(0)} = \frac{\omega_3}{\omega_2}\frac{\eta_{norm}}{g^2}P\sinh^2 gL \approx \frac{\omega_3}{\omega_2}\eta_{norm}L^2P_1(0)\sin c^2\frac{\Delta\beta}{2}L \tag{2.1.14}
$$

2.1.2 Phase match condition

From Eq. (2.1.14), it can be found that for achieving the highest conversion efficiency, the mismatch of propagation constant $\Delta\beta$, needs to be set to 0, which is called the phase match condition. However, usually this is not the case in either bulk nonlinear crystals or integrated nonlinear waveguides, because of the dispersion. One way to overcome this problem is to take advantage of material birefringence. The waves involved in the nonlinear process should have different polarizations. For waveguide with high confinement, the geometry can also introduce birefringence and compensate the dispersion. Those phase match methods are called direct phase match ($\Delta\beta = 0$).

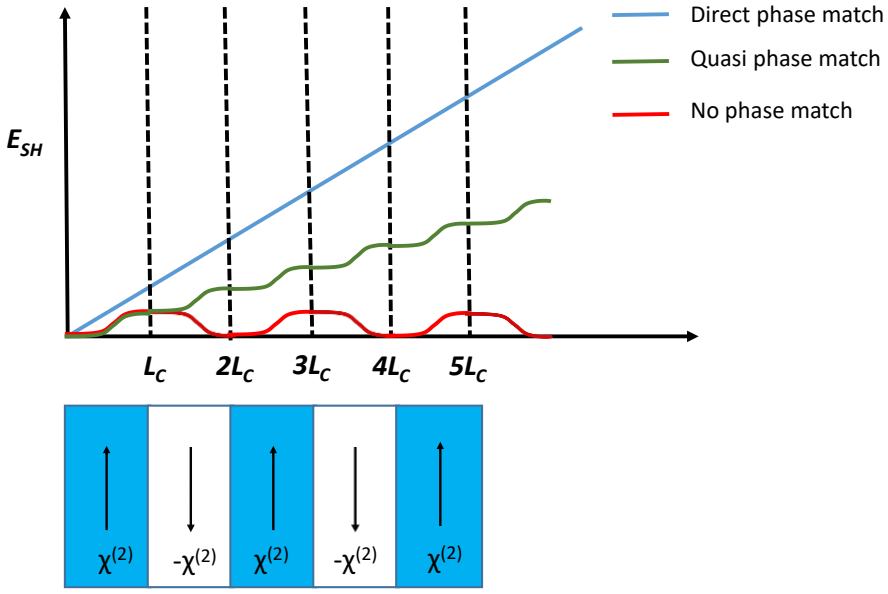

Figure. 2.1: SHG under different phase match conditions (upper) and the schematic drawing for periodic domain inversion for QPM.

Even though the direct phase match is the most straightforward and efficient phase match method for three wave mixing as shown in Fig. 2.1, in most situations it cannot be satisfied. Usually either the dispersion is too strong or the birefringence doesn't exist in many materials. As a result, another approach, which is called quasi phase match (QPM) was developed. In QPM, the mismatch of propagation constant is allowed to be nonzero, which lead to a π phase shift between wavefronts of the generated light after a propagation distance of $L_c = \frac{\pi}{\Delta\beta}$, called coherence length. A QPM structure usually has a special periodic modulation of the nonlinear coefficient d, which can be expressed as:

$$d(z) = \sum_m d_m \exp(-imKz), K = \frac{2\pi}{\Lambda}, m = 1, 2, 3, \ldots \tag{2.1.15}$$

Where Λ is the period of the modulation and *m* refers to *m*th Fourier component of *d(z)*. Therefore, an 'artificial' wavevector can be introduced into (2.1.6) to compensate the mismatch when:

$$\Delta\beta = mK \tag{2.1.17}$$

In actual applications, e.g. the $LiNbO_3$ waveguide, usually the first order grating is used because it is the most efficient. The period Λ is set to be the twice of the coherent length L_c. The modulation method is to flip the domain, so that the sign of *d* can be inverted. Details about this approach will be discussed in Chapter 3.

2.1.3 Second harmonic generation

This thesis will mainly focus on the demonstration of second harmonic generation (SHG), which is a special process of SFG where two photons with the same frequency

($\omega_1 = \omega_2 = \omega_P$) in Eq. (2.1.3) get involved as the pump light and generate a new photon with doubled frequency ($\omega_3 = \omega_{SH} = 2\omega_P$). Then according to the coupled mode theory:

$$\begin{aligned} \frac{\partial A_P}{\partial z} &= -\frac{\alpha_P}{2} A_P - i\kappa_f A_{SH} A_P^* e^{-i\Delta\beta z} \\ \frac{\partial A_{SH}}{\partial z} &= -\frac{\alpha_{SH}}{2} A_{SH} - i\kappa_{SH} A_P^2 e^{-i\Delta\beta z} \end{aligned} \tag{2.1.18}$$

Here we assume that the pump power is undepleted. The solution of SHG becomes:

$$\begin{aligned} A_P(L) &= e^{-\frac{\alpha_P}{2} z} A_p(0) \\ A_{SH}(L) &= -i\kappa_{SH} A_P^2(0) \frac{e^{(i\Delta\beta + \frac{\alpha_{SH}}{2} - \alpha_f)L} - 1}{i\Delta\beta + \frac{\alpha_{SH}}{2} - \alpha_f} e^{-\frac{\alpha_{SH}}{2} L} \end{aligned} \tag{2.1.19}$$

Then the efficiency of SHG can be obtained as:

$$\eta_{SHG} = \frac{P_{SH}}{P_P} = \frac{8 d_{eff}^2}{\varepsilon_0 c n_{SH} n_P^2 \lambda_{SH}^2 S_{eff}} g(L) P_P(0) \tag{2.1.20}$$

Where

$$\begin{aligned} S_{eff} &= \frac{(\iint E_P^2(x,y)dxdy)^2 \iint E_{SH}^2(x,y)dxdy}{(\iint E_P^2(x,y) E_{SH}(x,y)dxdy)^2} \\ g(L) &= e^{-2\alpha_P L} \frac{(e^{\Delta\alpha L} + 1)^2 - 4\cos^2(\frac{\Delta\beta L}{2}) e^{\Delta\alpha L}}{\Delta\alpha^2 + (\Delta\beta)^2} \\ \Delta\alpha &= \alpha_P - \frac{\alpha_{SH}}{2} \end{aligned} \tag{2.1.21}$$

If the propagation losses of the pump and SH light are negligible, Eq. (2.1.20) get simplified as:

$$\eta_{SHG} = \eta_{Nor} \sin c^2(\frac{\Delta\beta}{2}) L^2 P_P(0) \tag{2.1.22}$$

Where the normalized efficiency is:

$$\eta_{Nor} = \frac{8d_{eff}^2}{\varepsilon_0 c n_{SH} n_P^2 \lambda_{SH}^2 S_{eff}} \tag{2.1.23}$$

In the case of quasi phase match, instead of Eq. (2.1.6), $\Delta\beta$ becomes:

$$\Delta\beta = 2\beta_P - \beta_{SH} - \frac{2\pi}{\Lambda} \tag{2.1.24}$$

2.1.4 Resonators for SHG and OPO

The discussions above are all for the three wave mixing process in straight waveguides. Another important structure for nonlinear process is a resonance cavity. The intensity of light can get significantly enhanced at the resonance and thus improve the nonlinear conversion efficiency. Here we still take the SHG as an example to illustrate the second order nonlinear process in resonators.

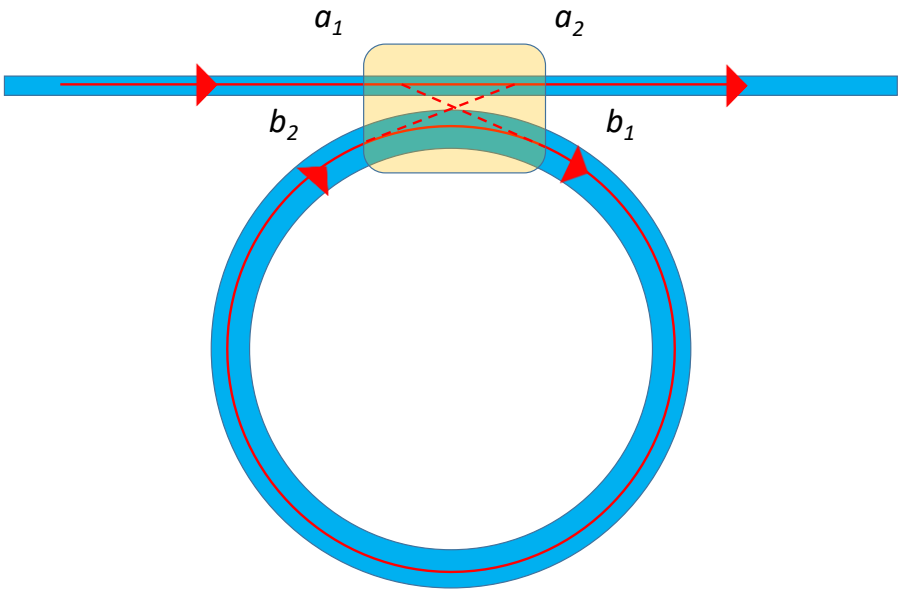

Figure. 2.2: Schematic of coupling into and out of a resonator.

Consider a resonator coupled to a bus waveguide as shown in Fig.2.2 [4], assuming the coupler is linear and lossless, the input and output amplitude can be expressed in the following matrix:

$$\begin{pmatrix} a_2 \\ b_1 \end{pmatrix} = \begin{pmatrix} t & \kappa_R \\ -\kappa_R^* & t^* \end{pmatrix} \begin{pmatrix} a_1 \\ b_2 \end{pmatrix} \tag{2.1.25}$$

Here t and κ are the transmission and coupling coefficients, respectively. Because there is no loss of the coupler, $|\kappa_R|^2 + |t|^2 = 1$. In this work, we are dealing with high quality resonators so $|\kappa_R| \ll |t| \simeq 1$.

For SHG, the amplitude of pump and SHG are indicated as $a_{P1,P2}$, $a_{SH1,SH2}$ and $b_{P1,P2}$, $b_{SH1,SH2}$, respectively. Then the input and output of SHG light can be linked as:

$$\begin{aligned} a_{SH2} &= \kappa_{R\_SH} b_{SH2} \\ b_{SH1} &= t_{SH}^* b_{SH2} \end{aligned} \tag{2.1.26}$$

To get the internal circulation relations taking the nonlinear interaction into account, we introduce the slowly varying amplitude $\hat{b}_i = b_i \exp(-ik_i z)$, where i = *SH, P,* then the coupled mode equation is:

$$\begin{aligned} \frac{\partial \hat{b}_P}{\partial z} + \frac{a_P \hat{b}_P}{2} + i\kappa \hat{b}_{SH} \hat{b}_P &= 0 \\ \frac{\partial \hat{b}_{SH}}{\partial z} + \frac{a_{SH} \hat{b}_{SH}}{2} + i\kappa \hat{b}_P^2 &= 0 \end{aligned} \tag{2.1.27}$$

Then by plugging in the relation $\hat{b}_{SH2} = \hat{b}_{SH}(L)$ and $\hat{b}_{P2} = \hat{b}_p(L)$, we obtain the equation:

$$\begin{aligned} \hat{b}_{SH2} &= (1 - \frac{\alpha_{SH} L}{2}) b_{SH1} - i\kappa L b_{P1}^2 \\ \hat{b}_{P2} &= (1 - \frac{\alpha_P L}{2}) b_{P1} - i\kappa L b_{SH1} b_{P1}^* \end{aligned} \tag{2.1.28}$$

Then by combining Eq. (2.1.25) and (2.1.28), we can obtain:

$$\hat{b}_{SH2} = -\frac{2i\kappa L b_{P1}}{|\kappa_{SH}|^2 + \alpha_{SH} L}$$
$$\frac{(|\kappa_P|^2 + \alpha_P L) b_{P1}}{2} + i\kappa L b_{P1}^* b_{SH1} = -|\kappa_P| a_{P1} \tag{2.1.29}$$

Then b_{SH1} can be eliminated and we can get the relation:

$$b_{P1}\left(\frac{1}{f_P} + \frac{f_{SH}\kappa^2 L^2 |b_{P1}|^2}{\pi^2}\right) = -\frac{|\kappa_P|}{\pi} a_{P1} \tag{2.1.30}$$

Where $f_i = (\alpha_i L + |\kappa|^2)/2\pi$ is the finess of the resonator.

With Eq. (2.1.30), we can express $|b_{P1}|$ as a function of $|a_{P1}|$, and then $|b_{SH1}|$ as a function of $|a_{P1}|$ by Eq. (2.1.29). Then we can get the following relation:

$$X(1+X)^2 = \frac{r_P}{1+r_P}\frac{P_P}{P_0}$$
$$\eta_{SH} = \frac{P_{SH}}{P_P} = 4\frac{r_{SH}}{1+r_{SH}}\frac{r_P}{1+r_P}\frac{X}{(1+X)^2} \tag{2.1.31}$$
$$r_{P,SH} = \kappa_{P,SH}^2 / \alpha_{P,SH}$$
$$P_0 = v_P \frac{\pi\varepsilon_0 n_P^4 n_{SH}^2}{8d^2}\frac{1}{Q_{oP}^2 Q_{0SH}}\frac{V_P^2 V_{SH}}{V_{PPSH}^2}(1+r_P)^2(1+r_{SH})$$

This method can also be easily extended to our three wave mixing process in resonators. For example, for the optical parametric oscillator (OPO), which has one pump light at frequency ω_P and generate signal and idler waves with frequency ω_S and ω_i, respectively. The threshold for OPO can be calculated as:

$$P_{th} = v_{P\_OPO}\frac{\pi\varepsilon_0 n_s^4 n_{P\_OPO}^2}{16d^2}\frac{1}{Q_{os}^2 Q_{0P}}\frac{V_s^2 V_{P\_OPO}}{V_{PSS}^2}\times\ldots$$
$$\times\frac{(1+r_{P\_OPO})^2(1+r_s)^2}{r_{P\_OPO}} \tag{2.1.32}$$

Here we need to point out that the calculation for the resonators above is based on the assumption that the nonlinear coefficient over the whole cavity is constant. However, this may not be the case due to the anisotropy of second order nonlinear tensor, e.g. <001> oriented GaAs. The treatment in that case will be discussed in Chapter 4.

2.2. Third order nonlinear process

In this section, the theory for third order nonlinear process is discussed. We will mainly focus on the frequency comb generation in micro-resonator, which has been one of the most important demonstrations in integrated nonlinear photonics. We will start with the physical explanation for the formation of Kerr comb and use the Lugiato-Lefever equation (LLE) to describe the comb generation analytically. Furthermore, temporal dissipative soliton generation will also be discussed.

2.2.1 Physics of Kerr-comb formation process

The Kerr-comb generation in microresonator is based on a so-called four wave mixing (FWM) process [5]–[7]. With CW pump light coupled into the resonator, the degenerate FWM happens and provides parametric gain symmetrically spaced at both sides of the pump frequency. Once the gain exceeds the loss, a pair of sidebands light can be generated at the resonances adjacent to the pumped resonance, as shown in Fig.2.3. With the increasing of pump power, a subsequent cascade non-degenerate FWM processes take place and generate more sidebands as shown in Fig.2.3. The spacing between between neighnoring comb lines is determined by the free spectrum range of the resonator. However, dispersion can cause mismatch between the sidebands and the resonance, which limits the bandwidth of the comb generation. In next section we will use nonlinear coupled mode equations to depict the temporal model for Kerr comb generation in micro-resonators.

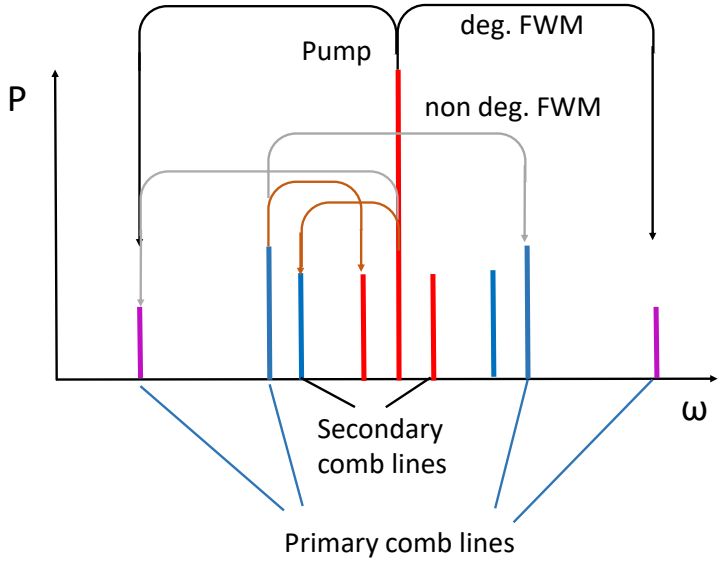

Figure. 2.3: Universal Kerr-comb formation processes.

In the early micro-comb demonstrations, unexpected noise phenomena were observed in various material platforms. This is due to the fact that during the formation of sidebands shown in Fig.2.3. It is not guaranteed that primary spacing's value is multi-time of the spacing of sub sidebands, which causes multi comb lines in a single resonace and thus leads to inconsistant combs. To address this problem, regimes where broadband coherent comb exist has been explored. In this state, all the comb lines get phase locked to each other, which is called Disspative Kerr Solitons (DKS).

2.2.2 Nonlinear coupled mode equations

Similar to what we did before for second order nonilenar process, we analyze the formation of frequency comb based on nonlinear coupled mode equations, which is the equation in conjunction with the quantum Langevin equations [8]:

$$\frac{\partial A_m}{\partial t} = -\frac{\kappa_m}{2} A_m + \delta_{m,m_0} \sqrt{\frac{\kappa_{ex,m} P_{in}}{\hbar \omega_0}} e^{-i(\omega_P - \omega_0)t}$$
$$+ \quad ig \cdot \sum_{m',m'',m'''} \Lambda_m^{m'm''m'''} D_m^{m'm''} A_{m'} A_{m''} A_{m'''}^* e^{-i(\omega'_m + \omega''_m - \omega'''_m - \omega_m)t} \tag{2.2.1}$$
$$+ \quad \sqrt{\kappa_{i,m}}\, \delta s_{i,m}(t) + \sqrt{\kappa_{ex,m}}\, \delta s_{ex,m}(t)$$

Here A_m is slowing varying amplitude of mode m in a resonator, κ_m refers to the decay rate of the cavity of that mode, which includes the intrinsic decay rate $\kappa_{i,m}$ and the external decay rate $\kappa_{ex,m}$. The mode of the pump (m_0, ω_0) is driven by a CW power P_{in} at the frequency of ω_P. $\delta s_{i,m}$ and $\delta s_{ex,m}$ denotes the quantum Langevin input noise with commutation relation $\left[\delta s_j(t), \delta s_j^\dagger(t')\right] = \delta(t - t')$ and zero mean. The term of summation is over all the modes of the resonators and satisfy the momentum conservation: $m' + m'' - m''' = m$. $D_m^{m'm''}$ is the factor of degeneracy, whose value is 2 when $m' \neq m''$ for the cross-phase modulation and non-degenerate FWM, and 1 for self-phase modulation and degenerate FWM. The coupling factor among different mode is:

$$\Lambda_m^{m'm''m'''} = \frac{\int e_{m'} e_{m''} e_{m'''}^* e_m^* dV}{\int |e_0|^4 dV} \frac{\chi^{(3)}(\omega_m = \omega_{m'} + \omega_{m''} - \omega_{m'''})}{\chi^{(3)}(\omega_0 = \omega_0 + \omega_0 - \omega_0)} \tag{2.2.2}$$

Where e_m is the distribution of the electric field vector for mode m.

In Eq. (2.2.1), the modes are normalized in the way that $|A_m|^2$ corresponds to the photon numbers for that mode. And the coupling constant g indicates the Kerr frequency shift per photon, and can be expressed as [9]:

$$g = \frac{3\hbar\omega_0^2 \chi^{(3)}(\omega_0)}{4\varepsilon_0 n^4(\omega_0) V_0} = \frac{\hbar\omega_0^2 c n_2(\omega_0)}{n^2(\omega_0) V_0} \tag{2.2.3}$$

Where V_m is the effective nonlinear volume of the mode, defined as:

$$V_m = \frac{(\int |e_m|^2 dV)^2}{\int |e_m|^4 dV} \tag{2.2.4}$$

The methods for solving Eq. (2.2.1) has been well studied. A key in those approaches is determine the eigen-frequency ω_m so that the dispersions can be found:

$$\omega_\mu \approx \omega_0 + D_1\mu + \frac{1}{2!}D_2\mu^2 + \frac{1}{3!}D_3\mu^3 ... \tag{2.2.5}$$

Where $\mu = m - m_0$ is the mode order relative to the pump mode. D_m denotes the m-th order of the dispersion, where D_2 is related to the group velocity dispersion (GVD) $\beta_j = \frac{\partial^j \beta}{\partial \omega^j}$.

In practice, an analytic solution to Eq. (2.2.1) is extremely challenging. However, based on certain approximations, the formation of comb generation can be modeled numerically. More details can be referred to Ref. [5].

2.2.3 Dissipative Kerr solitons

The generation of stable tempoeral soliton in microresonators based on Kerr-nonlinearity is a significant form of optical self-organization. The requirment for soliton generation, besides the third order nonlinear medium, is the anomolous dispersion of the waveguide. A big difference between the general Kerr comb and the temporal DKS is that the latter can lead to a stable pulse in time domain, whose duration is usually in femtosecond region, indicating broad spectrum with same line spacing.

To describe the formation of DKS, we still use LLE equation:

$$\frac{\partial A}{\partial t} - i\frac{1}{2}D_2\frac{\partial^2 A}{\partial \phi^2} - ig|A|^2 A = -(\frac{\kappa}{2} + i(\omega_0 - \omega_P))A + \sqrt{\frac{\kappa\eta P_{in}}{\hbar\omega_0}} \tag{2.2.6}$$

In which $A(\phi,t)=\sum_{\mu}A_{\mu}e^{i\mu\phi-i(\omega_{\mu}-\omega_{P})t}$ is the slowly varying field amplitude and $\phi\in[0,2\pi]$ is the angular coordinate inside the resonator with periodic boundary conditions. Eq. (2.2.6) can also be written in a dimensionless way as:

$$i\frac{\partial\psi}{\partial\tau}+\frac{1}{2}\frac{\partial^2\psi}{\partial\theta^2}+|\psi|^2\psi=(-i+\zeta_0)\psi+if \tag{2.2.7}$$

Where $\psi(\tau,\phi)=\sum a_{\mu}(\tau)e^{i\mu\phi}$ is the waveform, and we use dimensionless longitudinal coordinate $\theta=\phi\sqrt{\frac{1}{2d_2}}$. This equation is similar to the Nonlinear Schrodinger Equation (NLS) but driven and damped [10]. By using Lagrangian perturbation approach, the dissipative soliton can be solved. To do that, we introduce Lagrangian density, whose variation over ψ^* (Landau-Euler equation) leads to an unperturbed NLS equation:

$$\frac{\delta\xi}{\delta\psi^*}\equiv\frac{\partial\xi}{\partial\psi^*}-\frac{\partial}{\partial\tau}\frac{\partial\xi}{\partial\psi_{\tau}^*}-\frac{\partial}{\partial\theta} \tag{2.2.8}$$

$$\xi=\frac{i}{2}(\psi^*\frac{\partial\psi}{\partial\tau}-\psi\frac{\partial\psi^*}{\partial\tau})-\frac{1}{2}\left|\frac{\partial\psi}{\partial\theta}\right|^2+\frac{1}{2}|\psi|^4-\zeta_0|\psi|^2 \tag{2.2.9}$$

The detailed information for solving this equation can be found in Ref. [11]. The solution can be expressed as:

$$\begin{aligned}\psi(t)&=\sqrt{2\zeta_0}\,\mathrm{sech}(t/\Delta t)\\ \Delta t&=\frac{1}{D_1}\sqrt{\frac{D_2}{\zeta_0}}\end{aligned} \tag{2.2.10}$$

And the minimum pulse duration can be obtained as:

$$\Delta t_{\min}=\frac{1}{\pi D_1}\sqrt{\frac{\kappa D_2 n_0^2 V_{eff}}{\eta P_{in}\omega_0 c n_2}} \tag{2.2.11}$$

2.3. Summary

Besides the theoretical treatment we discussed in this chapter, in practice usually more factors need to be taken into account. In most cases, an analytical solution to describe a system would be impossible. Instead, numerical simulations under certain approximations can provide powerful tools to estimate the nonlinear process. In the later chapters, different kind of theoretical analysis will be used and discussed.

Reference

[1] Li Gui, "Periodically Poled Ridge Waveguides and Photonic Wires in LiNbO3 for Efficient Nonlinear Interactions," University of Paderborn, 2010.

[2] R. W. Boyd, *Nonlinear optics*. Burlington: Academic Press, 2008.

[3] D. A. Kleinman, "Nonlinear Dielectric Polarization in Optical Media," *Phys. Rev.*, vol. 126, no. 6, pp. 1977–1979, Jun. 1962.

[4] B. Sturman and I. Breunig, "Generic description of second-order nonlinear phenomena in whispering-gallery resonators," *J. Opt. Soc. Am. B*, vol. 28, no. 10, p. 2465, Oct. 2011.

[5] T. Herr, M. L. Gorodetsky, and T. J. Kippenberg, "Dissipative Kerr solitons in optical microresonators."

[6] R. Summary, "Dissipative Kerr solitons in optical microresonators," *Science (80-.).*, vol. 8083, 2018.

[7] T. J. Kippenberg, A. L. Gaeta, M. Lipson, and M. L. Gorodetsky, "Dissipative Kerr solitons in optical microresonators.," *Science*, vol. 361, no. 6402, p. eaan8083, Aug. 2018.

[8] Y. K. Chembo and N. Yu, "Modal expansion approach to optical-frequency-comb

generation with monolithic whispering-gallery-mode resonators," *Phys. Rev. A*, vol. 82, no. 3, p. 033801, Sep. 2010.

[9] P. Del'Haye, K. Beha, S. B. Papp, and S. A. Diddams, "Self-Injection Locking and Phase-Locked States in Microresonator-Based Optical Frequency Combs," *Phys. Rev. Lett.*, vol. 112, no. 4, p. 043905, Jan. 2014.

[10] I. V. Barashenkov and Y. S. Smirnov, "Existence and stability chart for the ac-driven, damped nonlinear Schrödinger solitons," *Phys. Rev. E*, vol. 54, no. 5, pp. 5707–5725, Nov. 1996.

[11] S. V. F . Zakharov, A. B, "Exact theory of two-dimensional selffocusing and one-dimensional self-modulation of waves in nonlinear media," *J. Exp. Theor. Phys.*, vol. 34, no. 1, p. 62, 1972.

Chapter 3

Lithium niobate on insulator platform

3.1. Background

$LiNbO_3$ is one of the most important materials which has been widely used in nonlinear optics [1]–[4]. Several advantages make $LiNbO_3$ an excellent candidate in nonlinear applications: First, it has relatively large second order nonlinear coefficients (d_{33} ~ *30 pm/V* at 1550 nm wavelength) and electro-optic effect (r_{33} ~ *30.8 pm/V at 630 nm wavelength*) [5], which enables efficient three wave mixing process as well as electrooptic modulation; Second, it has very wide transparent window ranging from 350 nm to 4.5 μm wavelength [6], which enables low material loss for both the fundamental and generated waves in nonlinear process. Furthermore, the well established techniques on $LiNbO_3$ fabrication and the mature foundry production provides the convenience to transfer the new demonstrations in research from lab scale to industry level [5].

However, even though the $LiNbO_3$ based nonlinear devices, e.g. periodically poled lithium niobate (PPLN) waveguides, provided good solutions to frequency conversions, they also have big limitations. The traditional $LiNbO_3$ waveguides are usually bulky, by using either proton exchange or Titanium diffusion [1], [7], [8] to create weak index contrast at the order of 0.1, whose schematic drawing is shown in Fig. 3.1 (a) and (b). Such weak index contrast leads to large waveguide modes, which significantly constrain the nonlinear efficiencies. Besides that, a more severe problem is that such waveguide structure is not compatible with photonic integration along with other components in PICs [9].

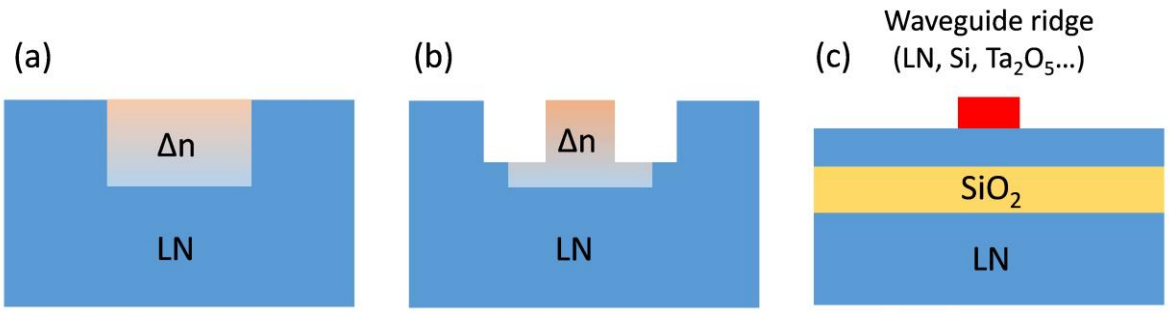

Figure. 3.1: Schematic drawing of different LN waveguides

The heterogeneous integration for $LiNbO_3$ was developed to address those problems [10], [11]. It is one of the early attempts in heterogeneous nonlinear photonics. Similar to the smart cut technology used in the fabrication of silicon on insulator (SOI) wafer [12], [13], a structure called LN on insulator (LNOI) was developed by heterogeneously integrating LN film onto SiO_2 layer. By doing this, a high index contrast in vertical direction (~ 0.6) can be obtained, which can lead to a much smaller mode volume for enhancing nonlinear processes. The photonic devices with compact waveguides are also more integration compatible in PICs. More encouragingly, this technology was soon commercialized to deliver with reliable wafers supplies, which greatly promote the prosperity of this field in the last 5 years [5].

In this chapter, we will discuss an integrated platform on LNOI wafer for nonlinear photonics. Such platform led to the first low loss thin film LN waveguides. Concurrently, we developed a new periodic poling technology for this platform, which enables the first demonstration of thin film PPLN waveguides. Those breakthroughs open the door for high performance LN integrated photonics in the future.

3.2 Platform design

A central question for the LNOI platform is the way to construct waveguide, specifically, how to introduce index contrast along the horizontal direction. Previous there were many papers about LNOI waveguides, either by using direct etch or introduce other kinds of materials to form ridge structures for light guiding [14], [15], as shown in Fig. 3.1(c). However, prior to our work, the propagation losses of those waveguides are much higher (on the order of few dB/cm) [10] compared to those of bulky waveguides by proton exchange and Ti diffusion. The reason is due to the extra loss introduced during the processing for the waveguide ridge.

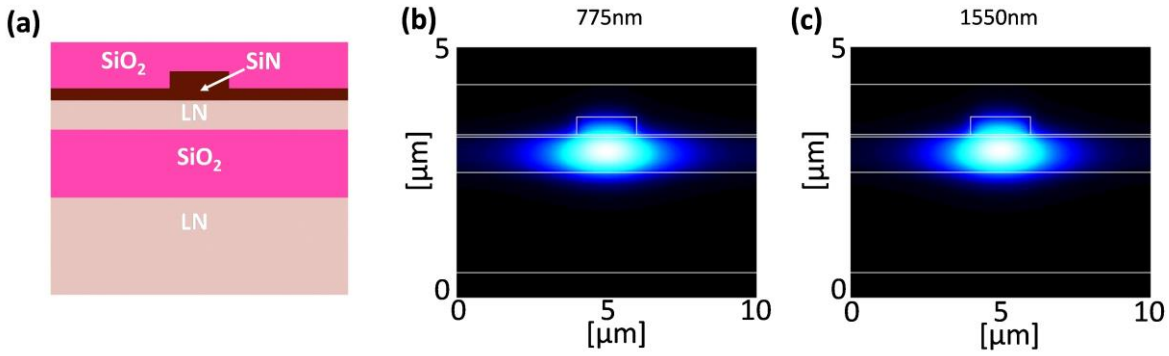

Figure. 3.2: (a) Schematic cross-section of the waveguide; (b) and (c): Simulated fundamental TE mode profiles of the waveguide at 1550 nm and 775 nm, respectively

In this work, we chose a waveguide structure with silicon nitride (SiN) rib standing on the LN film, as shown in Fig. 3.2 (a) [16]. There are several advantages of using SiN: First, SiN has lower material loss, a broader transparency window (0.4-6.7 μm), and does not suffer from two-photon absorption. Low loss SiN waveguides are popular for nonlinear photonics, like Kerr frequency comb and soliton generations. Second, the refractive index of

Si_3N_4 (1.98) is slightly smaller than that of LN, so the mode of the hybrid waveguide can be highly confined in the LN core for efficient nonlinear processes. Furthermore, SiN is a widely used CMOS compatible material in photonic foundry, which leads to the convenience for future integration in PICs.

The orientation of the LN film is set to be X-cut, instead of previously commonly used Y-cut crystal. In the X-cut layer, the largest nonlinear coefficient d_{33} is in the plane of the surface so that can be aligned with TE polarization, whose fundamental mode is of particular interest in PICs. This choice of crystal orientation enables a surface poling technology that we developed for thin film domain engineering, which will be discussed later in this chapter.

One factor which needs to be taken into account for ridge waveguide design is the lateral leakage. This effect was first observed in silicon on insulator ridge/rib waveguides, where the TM optical waveguide mode couples to an orthogonally polarized TE slab mode, which has a higher effective refractive index. The angle under which the TM optical waveguide mode couples to the TE slab modes depends thereby on the phase matching ($n_{TE} \sin\theta = n_{TM}$). The light that leaks into slab modes can be seen as a contribution to optical waveguide loss, which is unwanted. X-cut LN ridge waveguides are more prone to this problem due to birefringence. As the result, the thickness of the LN layer needs to be carefully designed. Detailed discussion is included in the testing and results section.

One of the devices we designed is the thin film PPLN waveguide. Fig. 3.2 (b) and Fig. 3.2 (c) depict the simulated TE waveguide mode profile at the fundamental (1550 nm) and the SHG (775 nm) signals, respectively, simulated with FIMMWAVE. The SiN layer is set to be 400 nm and LN thickness is set to be 700 nm. Due to the high index contrast structure (~0.6) and the sub-micron thickness of the LN film, the waveguide modes are confined into an area that is more than one order of magnitude smaller than obtained with proton exchange

or with Ti in-diffusion. This directly relates to more than an order of magnitude improvement for the efficiency of nonlinear effect. For both modes, over 90 % of the power is confined in the LN film.

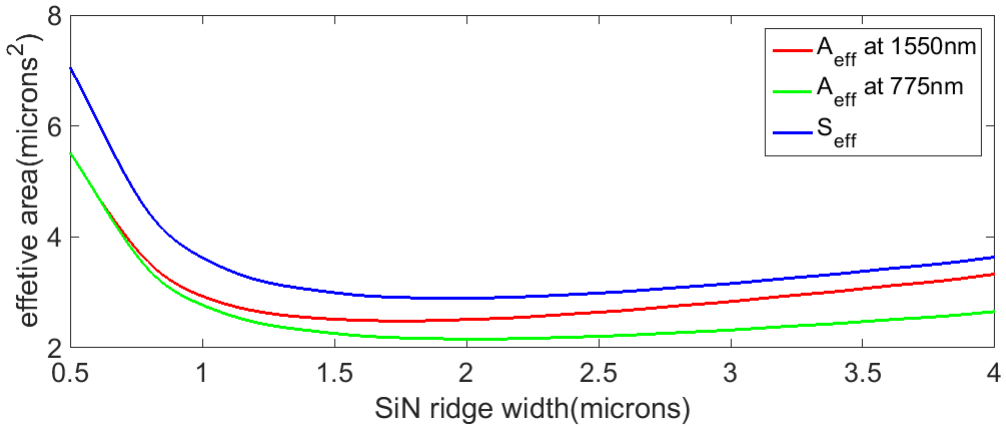

Figure. 3.3: Simulated effective waveguide area (A_{eff}) for the fundamental TE mode at 775 nm and at 1550 nm, and S_{eff} between these two modes as a function of the SiN ridge width.

As shown in Fig. 3.3, by tailoring the size of the SiN ridge, the effective mode size A_{eff} at both the telecom band (1550 nm), and the corresponding second harmonic light, (775 nm), can be reduced to around 2 μm^2. Also, the effective area of S_{eff} between these two modes for SHG, is close to the effective waveguide areas for both wavelengths, suggesting good overlap. This is critical for achieving high conversion efficiency.

3.3 Fabrication

In this section, process of LNOI nonlinear platform will be discussed. We will mainly focus on two key technologies we developed: the low loss waveguide process and thin film LN periodic poling.

3.3.1 Heterogeneous bonding

The heterogeneous bonding to build LNOI is similar with the smart cut technology used for fabricating SOI wafers. The general process is illustrated in Ref. [2]. At first ion implantation is applied to a donor LN wafer to create a defect layer. Then the crystal is bonded onto SiO_2 layer, which is on a handle wafer, assisted by plasma activation. After that, the bonded wafer go through high temperature annealing, which not only slice a LN layer from donor wafer from the implanted region, but also enhance the bonding strength. Once the thin film LN is left on the wafer with SiO_2 layer, a following CMP is applied to smooth the surface.

The heterogeneous LNOI technology has been well developed since the first demonstration and soon was commercialized. Now, 3- or 4- inch LNOI wafers, either with LN native or silicon substrate, can be provided by several companies. This dramatically relieves the requirements for fabrication of LNOI based photonic devices because usually the heterogeneous bonding is usually not available to most research labs or industries.

Other than wafer-to-wafer bonding, another approach for building integrated nonlinear device is to bond small LN dies, directly to waveguides, which has already been constructed, e.g. Si or SiN, to form PICs. This approach is particularly suitable to add the nonlinear functionality offered by LN into CMOS compatible chips for large scale and high volume production. More details will be discussed in Chapter 5.

3.3.2 Waveguide process

For making low loss LN-SiN waveguide, the key is to introduce high quality SiN and apply etch with low roughness. For SiN layer deposition, a common used method is low-pressure chemical vapor deposition (LPCVD), plasma-enhanced chemical vapor deposition

(PECVD) and sputtering. However, LPCVD requires a high deposition temperature (~ 800 $^{\circ}C$), which leads to cracking of the LN film due to the mismatch of thermal expansion coefficient between LN and SiO_2. For PECVD nitride, due to the reaction $SiH_x + NH_x \rightarrow SiN_x(+H_2)$, there are N-H bonds in deposited SiN films, which leads to absorption at C band. As a result, in this work we use sputtering for SiN deposition, which is done at room temperature without Hydrogen.

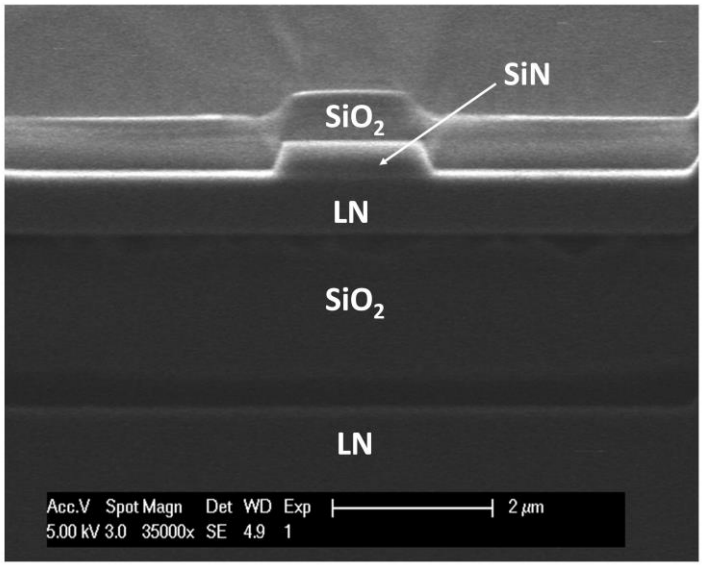

Figure. 3.4: SEM image taken after the sample is polished and then dipped in BHF for 1 min for improving the contrast.

The lithography is done by an i-line stepper to define the waveguide pattern. An inductively coupled plasma (ICP) etch is used to etch SiN. The gas flow for the etch is CHF3/CF4/O2. After the dry etch, the waveguides are coated with SiO_2 top cladding by sputtering as well. The cross section of the waveguide is shown in Fig. 3.4.

3.3.3 Thin film lithium niobate poling

Compared to traditional poling for bulky Z-cut LN crystal [17], the thin film poling for X-cut LN film requires the domain inversion along instead of vertical to the surface, so that both the positive and negative electrode should be put on the top of the LN layer. A more challenging part for thin film poling is the much shorter poling period, at the order of a few microns, which is caused by the stronger dispersion of compact mode size of SiN-LN waveguide [16].

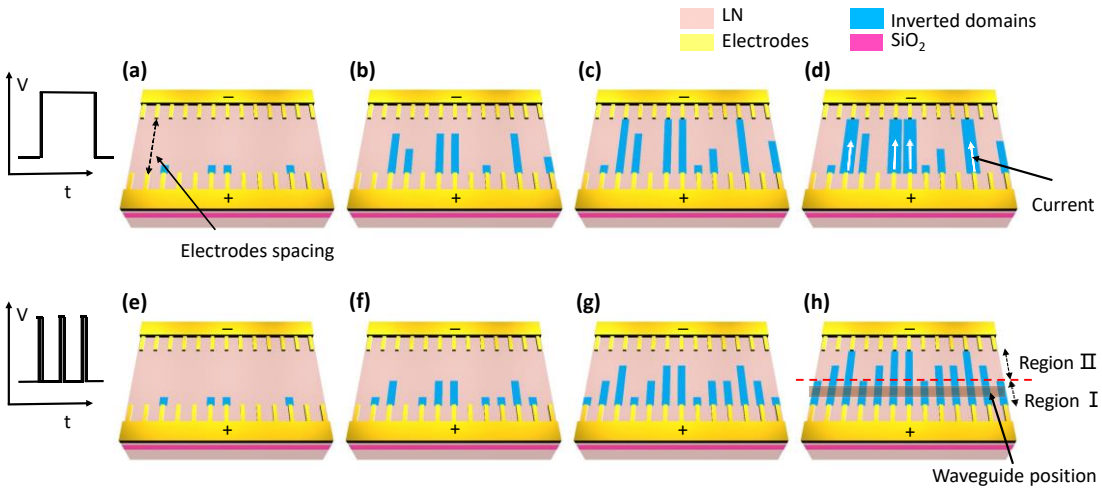

Figure. 3.5: (a)-(d) Schematic illustration of the evolution of inverted domain using a long poling pulse; (e)-(h) Schematic illustration of the evolution of inverted domains using multi-pulse waveform with short pulse duration.

The poling step is shown in Fig.3.5. In order to prevent the domain walls to merge together in the presence of short poling period, a small electrode spacing of 20 μm is used, with 30 μm long electrode teeth and 25 % duty cycle. Under this condition, we have achieved

a poling period as short as 2.4 μm, only limited by minimum feature size (600nm) of our lithography. We believe that switching to DUV or e-beam lithography can help us reach sub-micron periods.

The electric field needed for thin film poling is found to be higher than that for bulk poling. Indeed, domain inversion starts to occur with an electrical field greater than 30 kV/mm, while the threshold field for bulk LN [17] is ~21 kV/mm. This increase of threshold for poling can be attributed to the bonding interface between the thin film LN and the SiO_2 buffer layer, which hinders the domain inversion. At the same time, a high electric field is helpful to improve the poling yield, but it also speeds up the spread of the domain wall. Therefore, a trade-off should be found for the value of the field to be applied for actual poling.

As schematically illustrated in Fig. 3.5(a)-(d), the thin film LN poling may suffer from low yield and bad uniformity using traditional long-pulse poling. This is due to severe random domain growth and domain wall spread from the heating of the current channel [18]. To mitigate this, a multi-pulse voltage waveform with short pulse duration (~10 ms) is applied. We notice that, most nucleation sites where domain inversion starts from are generated at the beginning of a poling voltage pulse. Repeating the pulses thus allows the generation of more nucleation sites. This helps improve the uniformity of domain growth. The short pulse terminates before the temperature rises, thus minimizing the domain wall spread. Fig. 3.5(e)-(h) show the schematic evolution of the inverted domain using this method.

To further improve the poling quality of the device, the waveguide location is carefully designed. It was found that the best poling profile is achieved if the waveguide is defined closer to the positive electrode, shown in Fig. 3.5(h). The width of this region [labeled "Region I"] increases with the number of poling pulses, which should be set enough for

yielding a large number of nucleation sites. However, too many pulses may also increase the leakage current, spread or even merge the inverted domain and destroy the uniformity of the duty cycle. In this work, the poling conditions are optimized so that the width of Region I is ~4 μm. This allows the waveguide mode to fully overlap with the inverted domains, without significantly influencing duty cycle uniformity. In order to visualize the inverted domain, we use ion milling to create a cross section and let the z-surface of crystal exposed. By using HF etch, which attacks inverted and non-inverted domain differently, the poling position can be visualized. Fig. 3.6(b) shows the poling profiles in Region I for the actual device, which has ~100% yield and good duty cycle uniformity. Fig.3.6(c) shows a zoomed-in picture of inverted domain under SEM. The etched thickness by ion milling is 500 nm and the poling profile fully penetrated this thickness with almost constant duty cycle.

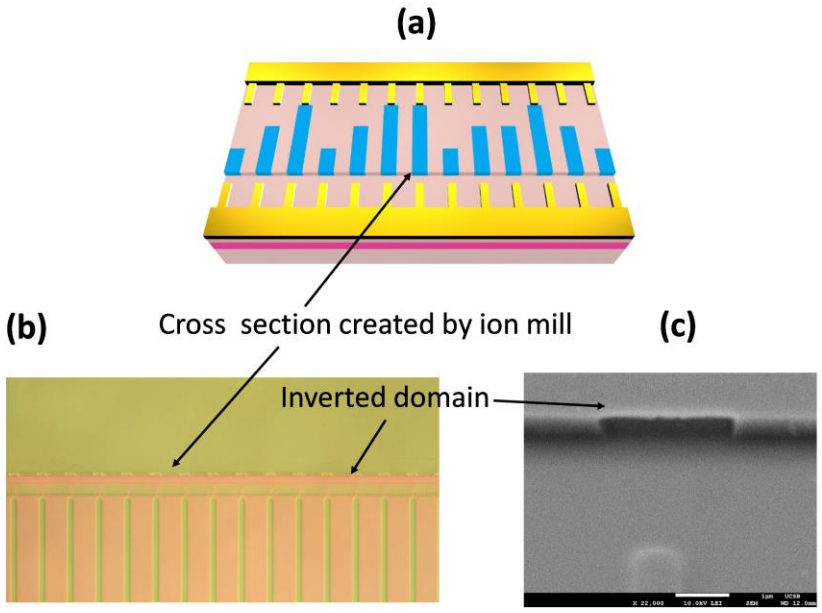

Figure. 3.6: (a) Schematic of cross-section of the device obtained after ion milling to visualize the periodically-poled region; (b) Top-view micrograph of the cross-section of a poled device after 10 min

48 % HF etch at room temperature. The dashed line corresponds to the cross-section in which the bright part is the poled area; (c) SEM image of inverted domain.

For a 700 nm thick LN film poling, we chose a relatively high electric field (48 kV/mm) to improve the poling yield. A pulse duration of 10 ms leads to good poling profile. We use 2 pulses, resulting in a duty cycle of (40 ± 10) % and almost 100 % yield. The interval between each pulse is 10 s to reduce thermal issues. These conditions result in a poling quality that is comparable to bulk LN poling [17].

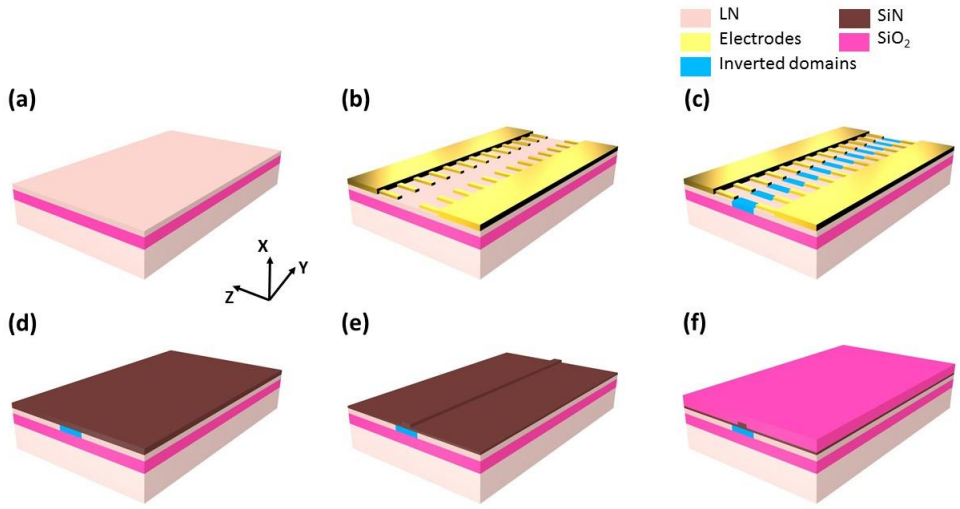

Figure. 3.7: Processing flow of PPLN waveguide fabrication.

The periodic poling technology, combined with the waveguide fabrication process, can enable the demonstration of thin film PPLN on chip. The processing flow is shown in Fig. 3.7.

3.4 Low loss waveguide

The propagation loss of waveguides is the key factor that influences the nonlinear performance. For PPLN waveguides, a lower loss enables a longer interaction length for nonlinear process. For resonator designs, it leads to a high quality factor to enhancing the light intensity inside cavities, which can significantly improve the efficiencies of frequency conversion.

In this work, the loss of LNOI waveguide is extracted from the Fabry-Perot fringes arising from facet-to-facet reflections in the waveguide. The values of loss are obtained from standard Hakki-Paoli methods:

$$L\alpha = \ln\left(\sqrt{R1R2}\,\frac{\sqrt{K}+1}{\sqrt{K}-1}\right) \tag{3.4.1}$$

Where L is the length of the cavity, α is the propagation loss, $R1$ and $R2$ are the reflectivities of the input and output facet, which is calculated by FDTD simulations, K is the extinction ratio of the Fabry-Perot ripples.

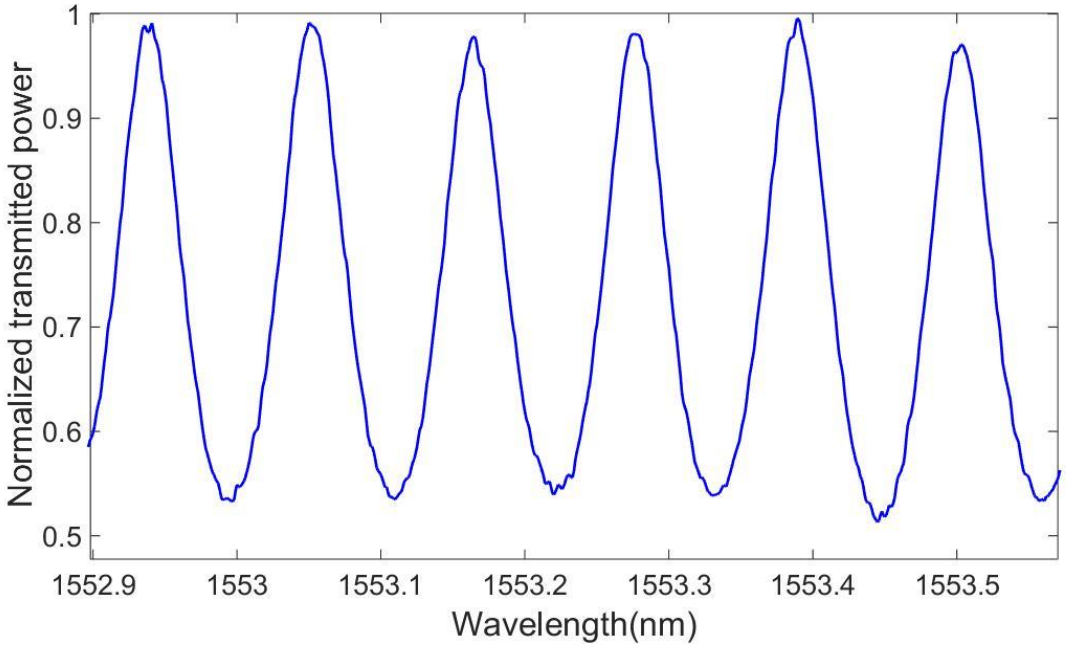

Figure. 3.8: Transmission spectrum for a 5-mm long waveguide whose SiN ridge is 2 μm wide and 400 nm tall on a 700 nm thick LN film.

For a 5-mm long waveguide, the transmission is plotted in Fig. 3.8. Based on Eq. (3.4.1), it can be estimated that the propagation loss of the waveguide near 1550 nm wavelength is $\alpha_\omega \cong (0.3 \pm 0.2)$ dB/cm. The uncertainly is caused by the variation of the extinction ratio *K* over the spectrum. For the first time, the ultra-low loss of LNOI waveguide is comparable to the best results obtained with proton exchange and Ti in-diffused waveguides, which is essential for building long PPLN devices.

3.5 PPLN waveguides for frequency conversion

PPLN waveguides are previously the most commonly used devices for three-wave mixing process, in optical communication networks, single-photon generation and multi-laser sources. Here we successfully transfer this technology to LNOI platform.

The performance of the PPLN is evaluated in terms of SHG. A tunable single-frequency CW laser (Agilent 81642A, typical linewidth: ~0.1 MHz, spectral range: 1510-1640 nm) is used as the seed. An erbium-doped fiber amplifier (EDFA, IPG EAR-2K-C) is used during high-power testing. Light is passed through a polarization controller to excite the TE-polarized mode of the waveguide. Tapered lensed fibers couple the light in and out of the PPLN device. A wavelength-division multiplexer (WDM) is placed at the output to split the pump light and the SH light. A telecom-wavelength optical power meter and a Si-PIN photo-detector are used to monitor the pump and SH power, respectively. Finally, the output spectra are recorded by an optical spectrum analyzer (Yokogawa AQ6370C).

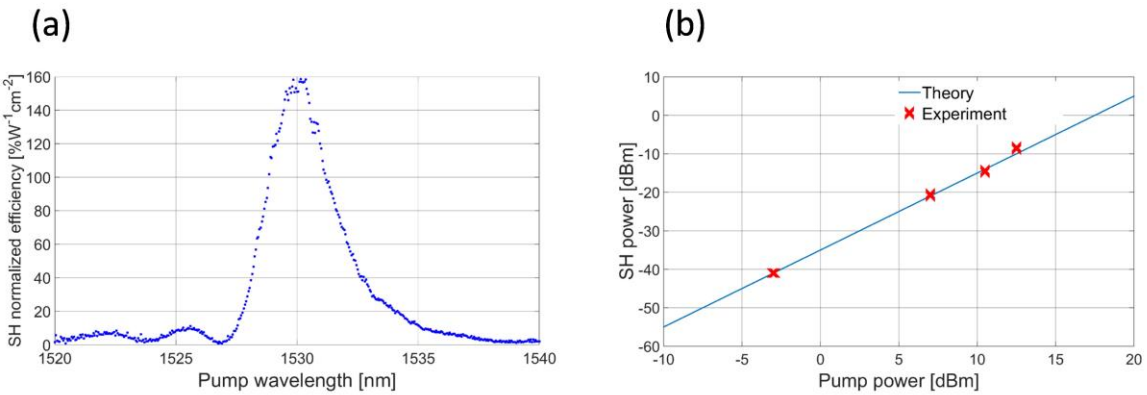

Figure. 3.9: PPLN waveguide characterized as a wavelength converter using SHG: (a) normalized efficiency as a function of the pump wavelength; (b) peak generated SH power under different pump powers (red crosses), compared to theoretical predictions from (S7), assuming η_{nor} = 160 % $W^{-1}\cdot cm^{-2}$.

For a waveguide with 700 nm thick LN film, the poling period is around 6.6 μm. The normalized SHG efficiency for a 5-mm long PPLN waveguides is shown in Fig. 3.9(a). The peak normalized efficiency η_{nor} we achieved is ~160 % $W^{-1}\cdot cm^{-2}$ at 1530 nm pumping wavelength. This is more than 4 times larger than that of typical PPLNs (30-40 % $W^{-1}\cdot cm^{-2}$) [1]. The SH power generated is 80 nW at a pump power of 0.5 mW. Fig. 3.9(b) shows the peak SH power under different pump powers. A good agreement is obtained with the theoretical predictions, assuming η_{nor} = 160 % $W^{-1}\cdot cm^{-2}$. The coupling loss at telecom band is ~6 dB per facet. For SH light the coupling loss plus the propagation loss in lensed fiber is ~14 dB. The relative high insertion losses at input and output are mainly due to the much smaller mode size, and to the fact that lensed fibers are multi-mode for SH light, which increases both the coupling and propagation loss of the fiber. This influences the external conversion efficiency. However, adding waveguide tapers at both input and output to match the spot size can help reduce the coupling losses. Moreover, switching to free space coupling

may also reduce the loss caused by the lensed fiber, in particular for the SH light. We would expect that finally the coupling loss is comparable with bulk PPLN waveguides.

The theoretical predicted normalized efficiency is 1600% $W^{-1}cm^{-2}$, ten times higher than the one mentioned above. One reason for that difference is the leakage of light for the SHG light, which was first observed in silicon on insulator ridge/rib waveguides, where the TM optical waveguide mode couples to an orthogonally polarized TE slab mode, which has a higher effective refractive index. The angle under which the TM optical waveguide mode couples to the TE slab modes depends thereby on the phase matching ($n_{TE} \sin\theta = n_{TM}$).

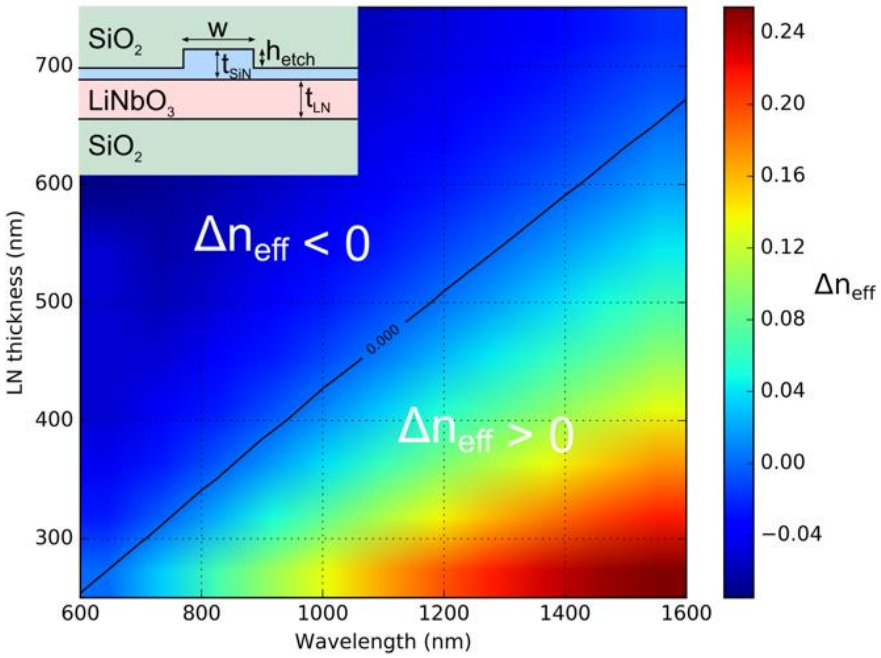

Figure. 3.10: Effective index difference between the TE waveguide mode and the TM slab mode. Waveguide with $\Delta n_{eff} < 0$ can suffer from lateral leakage.

Ridge waveguides in LNOI, such as the illustrated one in the inset of Fig. 3.10, are prone to the same effect, because the TM slab mode that surrounds the ridge waveguide, can be higher than the TE waveguide mode (as the ordinary refractive n_o index is higher than the extraordinary refractive n_e index in lithium niobate). Fig. 3.10 shows the difference between the effective index of the TE waveguide mode and the TM slab mode ($\Delta n_{eff} = n_{eff,TE\_waveguide} - n_{eff,TM\_slab}$) as a function of wavelength and lithium niobate thickness, using the following parameters: the silicon nitride (SiN) thickness was 400 nm, the etch depth (h_{etch}) was 350 nm and the waveguide width (w) was 2 µm. The black line in the graph indicates a refractive index difference between the modes of zero ($\Delta n_{eff} = 0$), which means that waveguides that are above the black line can suffer from lateral leakage. One can see that the lithium niobate thin-film thickness needs to be thinner for waveguides that are designed for shorter wavelengths.

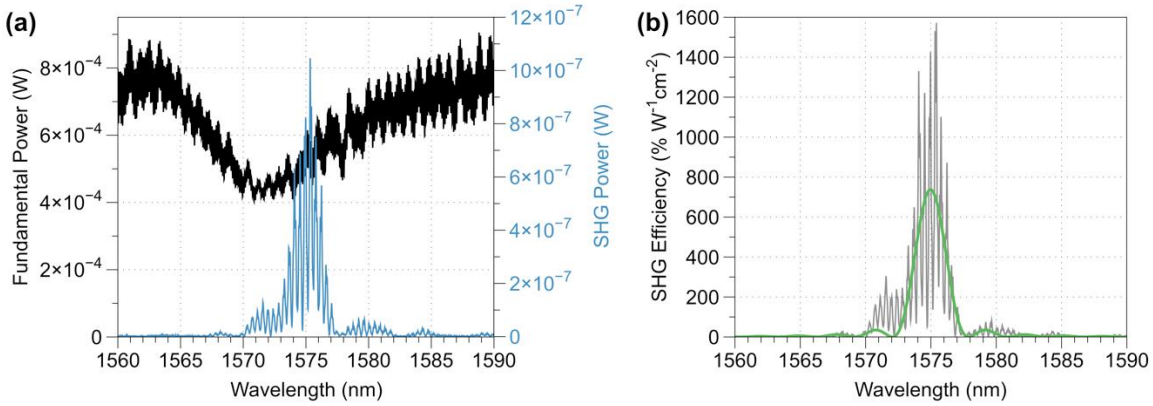

Figure. 3.11: (a) fundamental and SHG power as a function of the pump wavelength; (b) SHG efficiency and fitted curve.

To address this problem, we chose a lithium niobate thin-film thickness of 300 nm, in order to avoid lateral leakage at the SH wavelength, when pumping the waveguide at C-band

wavelengths. The thinner lithium niobate thickness requires us to adapt the poling period of the quasi-phase matching structure to 4.98 μm. The length of the periodically poled waveguide was 4.8 mm. Fig. 3.11(a) shows the fundamental and SHG power on the chip as a function of the pump wavelength. It can be seen that the SHG power is highest around a wavelength of 1.575 μm. The periodic oscillations in the fundamental and SH power can be explained by the Fabry-Perot effect from the end faces of the waveguide. Fig. 3.11(b) shows the SHG efficiency as a function of the pump wavelength, where the green curve is a fitted $sinc^2$ function. The peak normalized conversion efficiency we demonstrated is ~780% $W^{-1}cm^{-2}$.

3.6 Summary and outlook

Besides SHG, PPLN also play important roles in other nonlinear applications such as OPO and DFG. Moreover, building resonant cavities based on PPLN waveguides can further enhance the nonlinear efficiencies. Another interesting area for LNOI in nonlinear optics is the frequency comb generation, either by the Kerr or cascaded $\chi^{(2)}$ effect. Besides our low loss structures, recently there have been many works of low loss LNOI waveguide by using direct etch, which can also enable high Q resonators for those demonstrations.

Another important application for LN is electro-optic (EO) modulators. For decades, diffused waveguide based lithium niobate modulators were one of the standard optical modulators in telecommunication applications. LN modulators in LNOI can achieve very high modulation frequencies with moderately low voltage-length product ($V_\pi L$). The low voltage-length product can be important in both the energy consumption of the device, but also in allowing for compact device size. It can be envisaged to have the same compact dimensions as the InP modulators that are now displacing traditional in-diffused LN waveguide based

modulators in coherent optical transceivers. Moreover, the fast response time of LNOI modulators (up to 110 GHz) [19], [20] makes their modulation bandwidth more than sufficient for future 400 Gb/s channels running at over 60 Gbaud.

Reference

[1] Li Gui, "Periodically Poled Ridge Waveguides and Photonic Wires in LiNbO3 for Efficient Nonlinear Interactions," University of Paderborn, 2010.

[2] G. Poberaj, H. Hu, W. Sohler, and P. Günter, "Lithium niobate on insulator (LNOI) for micro-photonic devices," *Laser Photon. Rev.*, vol. 6, no. 4, pp. 488–503, Jul. 2012.

[3] K. Nakamura, J. Kurz, K. Parameswaran, and M. M. Fejer, "Periodic poling of magnesium-oxide-doped lithium niobate," *J. Appl. Phys.*, vol. 91, no. 7, pp. 4528–4534, Apr. 2002.

[4] E. L. Wooten *et al.*, "A review of lithium niobate modulators for fiber-optic communications systems," *IEEE J. Sel. Top. Quantum Electron.*, vol. 6, no. 1, pp. 69–82, Jan. 2000.

[5] A. Boes, B. Corcoran, L. Chang, J. Bowers, and A. Mitchell, "Status and Potential of Lithium Niobate on Insulator (LNOI) for Photonic Integrated Circuits," *Laser Photonics Rev.*, vol. 12, no. 4, pp. 1–19, 2018.

[6] R. W. Boyd, *Nonlinear optics*. Burlington: Academic Press, 2008.

[7] F. Généreux, G. Baldenberger, B. Bourliaguet, and R. Vallée, "Low-voltage tunable second-harmonic generation in an x-cut periodically poled lithium niobate waveguide," *Opt. Lett.*, vol. 32, no. 9, p. 1108, May 2007.

[8] K. R. Parameswaran, R. K. Route, J. R. Kurz, R. V. Roussev, M. M. Fejer, and M.

Fujimura, “Highly efficient second-harmonic generation in buried waveguides formed by annealed and reverse proton exchange in periodically poled lithium niobate,” *Opt. Lett.*, vol. 27, no. 3, p. 179, Feb. 2002.

[9] S. Fathpour, “Heterogeneous Nonlinear Integrated Photonics,” *IEEE J. Quantum Electron.*, vol. 54, no. 6, pp. 1–16, Dec. 2018.

[10] H. Hu, R. Ricken, and W. Sohler, “Lithium niobate photonic wires,” *Opt. Express*, vol. 17, no. 26, p. 24261, Dec. 2009.

[11] S. Kurimura, Y. Kato, M. Maruyama, Y. Usui, and H. Nakajima, “Quasi-phase-matched adhered ridge waveguide in LiNbO3,” *Appl. Phys. Lett.*, vol. 89, no. 19, p. 191123, Nov. 2006.

[12] T. Komljenovic *et al.*, “Heterogeneous Silicon Photonic Integrated Circuits,” *J. Light. Technol.*, vol. 34, no. 1, pp. 1–1, 2015.

[13] M. L. Davenport, L. Chang, D. Huang, N. Volet, and J. E. Bowers, “(Invited) Heterogeneous Photonic Integration by Direct Wafer Bonding,” *ECS Trans.*, vol. 75, no. 9, pp. 179–183, Sep. 2016.

[14] L. Chen, Q. Xu, M. G. Wood, and R. M. Reano, “Hybrid silicon and lithium niobate electro-optical ring modulator,” *Optica*, vol. 1, no. 2, p. 112, Aug. 2014.

[15] P. Rabiei, J. Ma, S. Khan, J. Chiles, and S. Fathpour, “Heterogeneous lithium niobate photonics on silicon substrates,” *Opt. Express*, vol. 21, no. 21, p. 25573, Oct. 2013.

[16] L. Chang, Y. Li, N. Volet, L. Wang, J. Peters, and J. E. Bowers, “Thin film wavelength converters for photonic integrated circuits,” *Optica*, vol. 3, no. 5, p. 531, 2016.

[17] Gregory David Miller, “Periodically Poled Lithium Niobate: Modeling, Fabrication, and Nonlinear-Optical Performance,” Stanford, 1998.

[18] K. Mizuuchi, A. Morikawa, T. Sugita, and K. Yamamoto, "Electric-field poling in Mg-doped LiNbO3," *J. Appl. Phys.*, vol. 96, no. 11, pp. 6585–6590, Dec. 2004.

[19] A. J. Mercante, P. Yao, S. Shi, G. Schneider, J. Murakowski, and D. W. Prather, "110 GHz CMOS compatible thin film LiNbO3 modulator on silicon," *Opt. Express*, vol. 24, no. 14, p. 15590, Jul. 2016.

[20] C. Wang *et al.*, "Integrated lithium niobate electro-optic modulators operating at CMOS-compatible voltages," *Nature*, vol. 562, no. 7725, pp. 101–104, Oct. 2018.

Chapter 4

(Aluminum) Gallium Arsenide on insulator platform

4.1. Background

In last chapter, we discussed the heterogeneous LNOI as a promising nonlinear platform. However, LNOI, as well as many other nonlinear dielectric nonlinear platforms, also suffers from many problems when integrating nonlinear components into PICs, which are due to the intrinsic properties of the dielectric material itself.

One major challenge for nonlinear dielectric nonlinear devices is the efficiency. The power levels that are achievable with integrated lasers are usually not high enough to drive current on-chip nonlinear optical processes efficiently. Typical on-chip laser powers are in the order of tens of milliwatt or lower [1]. However, current most demonstrated integrated nonlinear devices do not meet the efficiency requirements to work at these power levels. One example is OPOs. So far the lasing of an integrated OPO based on $\chi^{(2)}$ nonlinearity, which is pumped by an on-chip laser, has not been demonstrated due to the high threshold power requirements

[2]. Even though a lot of research has been put in increasing the quality factor of dielectric resonators to overcome this difficulty, the intrinsic low nonlinear coefficients prevent the realization of ultra-high efficiencies of those devices.

Another difficulty is that currently the dielectric nonlinear materials used for integrated photonics are not compatible with the integrated active devices [3], [4], either in design, fabrication, or integration. As a result, the nonlinear components are still far from being integrated together with lasers, amplifiers and photodetectors on the same chip, but have to be connected by either fiber coupling or chip to chip butt coupling [5]. This dilemma not only drops the conversion efficiency of the nonlinear optical process by orders of magnitude due to the power lost in coupling, but also introduces degradation to the whole system performance due to the coupling instabilities and reflections of the facets.

Material	d ($\frac{1}{2}\chi^{(2)}$) [pm/V]	$\chi^{(3)}$ [cm^2/W]	Mode size [μm^2]
$LiNbO_3$	30	5.3×10^{-15}	~2
AlN	1	2.3×10^{-15}	~1
Si_3N_4	-	2.5×10^{-15}	~1
Si	-	6.5×10^{-14}	~0.25
GaAs (AlGaAs)	119	1.6×10^{-13}	~0.25

Table 4.1. Comparison of nonlinear optical coefficients and mode sizes of waveguides among commonly used nonlinear materials.

The key to solve those problems is to find materials that can be used for ultra-high efficient nonlinear processes and as active devices simultaneously. GaAs and the closely related AlGaAs alloy turn out to be the perfect candidate, as they have one of the largest second ($\chi^{(2)}$) and third order nonlinear optical coefficients ($\chi^{(3)}$) [6], orders of magnitude higher than those of other commonly used nonlinear optical materials (see Table 4.1). However, previously, most GaAs (AlGaAs) waveguides used GaAs (AlGaAs) thin films on native substrates due to the epitaxial growth requirements [7]. Those waveguides have a relative weak vertical refractive index contrast ($\Delta n \approx 0.2$), which limits the achievable optical intensity and hampers waveguide designs that fulfill the phase matching condition or allow dispersion engineering. Several techniques have been demonstrated to overcome these issues, such as thermally oxidizing of AlGaAs cladding layers or suspending the waveguides [7]–[9]. However, those approaches suffer from high optical waveguide losses, which prevent the use of such designs for long waveguides or high Q resonators to boost the nonlinear process. Furthermore, most of these waveguide designs are difficult to integrate in common PIC platforms. These limitations can be overcome by heterogeneous integration [10], which enables a convenient way to integrate high quality nonlinear materials into PICs [11]. Heterogeneous integration also enables the use of low-index claddings, e.g. SiO_2 for high optical confinement, which enhances the nonlinear optical interaction due to the higher intensity.

In this work, we present a (Al)GaAs on insulator ((Al)GaAsOI) waveguide nonlinear optical platform. The waveguide structure is achieved by heterogeneous bonding a (Al)GaAs thin-film onto an oxidized Si substrate and coating it with SiO_2. This platform enables highly efficient nonlinear optical processes, thanks to the high material nonlinearity of (Al)GaAs, the strong refractive index contrast and the low propagation loss of the waveguides. In later

sections of this chapter, we will show many ultra-efficient nonlinear processes on this platform: a record high SHG nomalized efficiency of 13,000%$W^{-1}cm^{-2}$ from waveguide, 65,000 %/W absolute SHG conversion efficiency inside resonators, and record low threshold of 220 μW for frequency comb generation. We will also show the high Q resonators demonstrated with beyond 1 million Q. Furthermore, the future for a fully integrated nonlinear PICs offered by this platform will also be discussed.

4.2. Fabrication

In this section, processing of the (Al)GaAs nonlinear platform will be discussed, including the heterogeneous integration of (Al)GaAs and the fabrication of low loss waveguides.

4.2.1 Heterogeneous bonding

Heterogeneous bonding for (Al)GaAs is a mature technique widely applied in silicon photonics to integrate gain medium onto Si waveguide [1]. However, to transfer this technology onto insulator didn't originate until recently. The first attempt for this approach was done by depositing PECVD SiO_2 on the epi surface and then doing BCB bonding afterwards onto an InP handling wafer [10]. Even though it offers the high index contrast required for nonlinear applications, the BCB bonding post stability problems to the process. In the meanwhile, the InP handling wafer may have difficulties for high volume and low cost production.

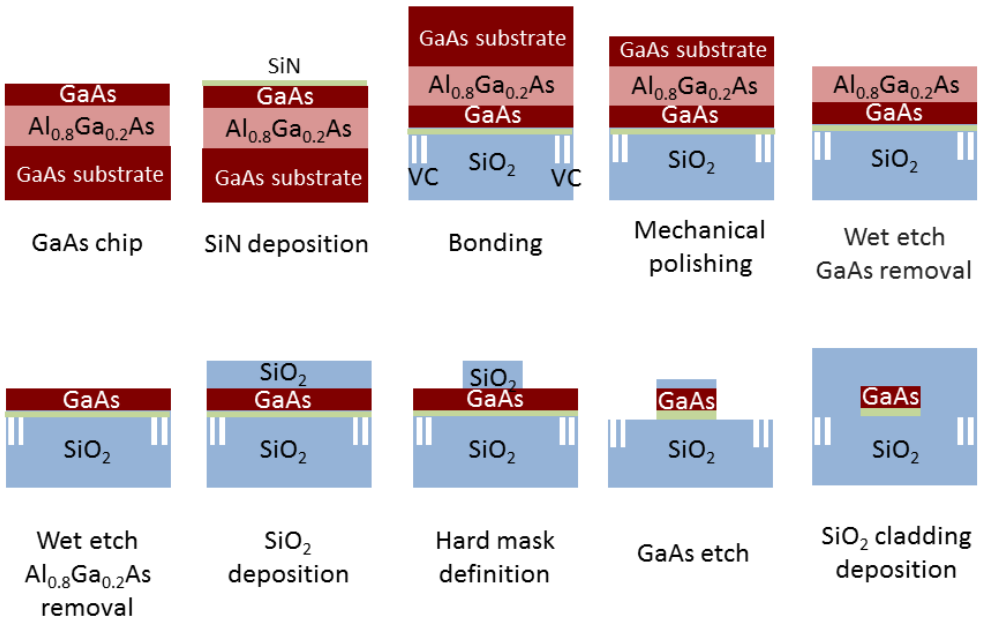

Figure. 4.1: Process flow for GaAs waveguide device fabrication.

Here we developed a process by using directly bonding technology and Si substrate [12]. The process flow is shown in Fig. 4.1. The epi is prepared by metal-organic chemical vapor deposition (MOCVD), with (Al)GaAs nonlinear on top and a sacrificial layer between nonlinear film and substrate. There are many different options for the sacrificial layer, such as AlGaAs with high Al portion or InGaP. The former one is preferred for AlGaAs integration as the high selectivity. A 5-nm-thick adhesion layer (SiN or Al_2O_3) was sputtered on the (Al)GaAs thin-film surface, to enhance the bonding strength compared to SiO_2-(Al)GaAs interface. This chip was bonded onto a Si wafer with 3-μm-thick thermal SiO_2 layer, after plasma activation. The thermal SiO_2 layer was patterned before the bonding by inductively coupled plasma (ICP) etching to form 5 × 5 μm^2 square vertical channels (VCs) with 50 μm spacing for gas release. The bonded piece was annealed for 12 hours under pressure to

enhance the bonding strength. Afterwards, mechanical polishing was applied to lap the GaAs substrate thickness down to 70 μm. The remaining GaAs substrate was removed by wet etching with H_2O_2:NH_4OH (30:1) and the sacrificial layer was removed by wet etch. Fig. 4.2 shows the picture of the bonded chip after substrate removal, with a bonding yield larger than 95%. The surface roughness of the bonded GaAs thin film on the chip is ~0.3 nm (RMS), which is very similar compared to the pre-processing surface of GaAs (~0.2 nm), both measured by atomic force microscopy.

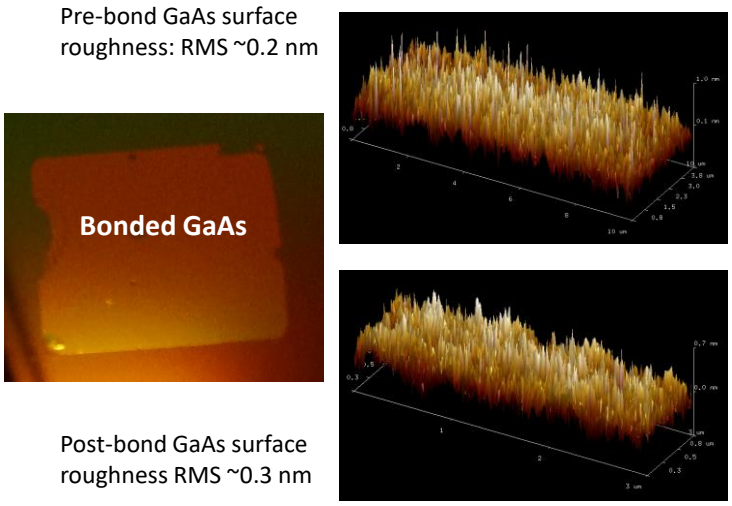

Figure. 4.2: Bonded GaAs thin film on SiO_2 after substrate removal (left), and the AFM results for surface roughness before and after bonding.

4.2.2 (Al)GaAsOI waveguide process

The key step for (Al)GaAsOI process is the waveguide etch, because the high index contrast means the loss is more sensitive to the scattering of the sidewall. In this work, after substrate removal and sacrificial layer wet etching, a layer of SiO_2 was deposited on the (Al)GaAs thin-film as hard mask. The SiO_2 layer was patterned by using Deep Ultraviolet

(DUV) lithography followed by Inductively Coupled Plasma (ICP) etching with a $CHF_3/CF_4/O_2$ gas chemistry. Afterwards, a 15 second ICP etching step with a Cl_2/N_2 gas chemistry was applied to etch the GaAs layer.

To get a smooth etching profile, the lithography and etching have been optimized to reduce the roughness. Fig. 4.3 shows the SEM image of the waveguide sidewall, as well as the cross section (right).

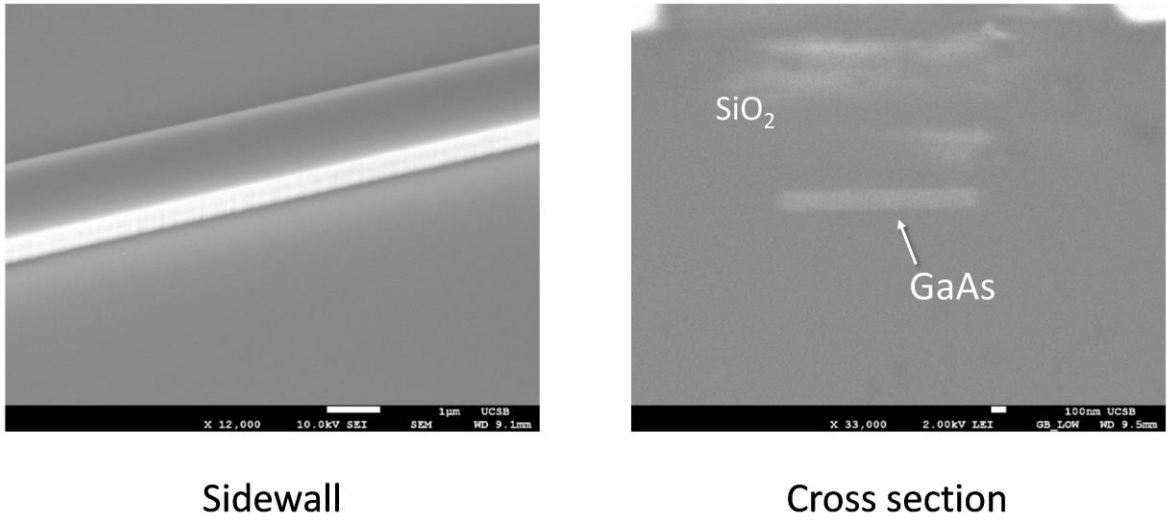

Figure. 4.3: SEM image of GaAs waveguide with SiO_2 hard mask on top after GaAs etch (left) and SEM image of the waveguide cross section (right).

4.2.3 Surface passivation

The defects states at the (Al)GaAs surface may lead to significant absorption, increasing the waveguide loss [13]. To address that, surface passivation is required in the waveguide process. In this work, we use Atomic Layer Deposit (ALD) to deposit highly uniform, conformal layer of alumina (Al_2O_3) on each side of (Al)GaAs core. The thickness of the layer is between 5 to 10 nm.

Besides the Al_2O_3, it is found that sputtered SiN layer are also beneficial for the passivation. The waveguide fully passivated by SiN shows similar propagation loss with the one with Al_2O_3. This may be explained by the theory previously proposed that the formation of stable GaN on the surface of (Al)GaAs can eliminate the defect states. Further investigation in this approach, as well as using other materials for reducing the surface absorption, would be of importance, especially when working at short wavelengths.

4.3. Waveguides for SHG

One great advantage of the (Al)GaAsOI platform is the high index contrast, which can fulfill the phase matching condition for efficient three wave mixing. This can be explained by the fact that for waveguides with submicron dimensions, the dispersion is mainly determined by waveguide geometry rather than the material dispersion. Here we take the SHG process as an example. In this case the effective refractive indices for different polarized modes of the waveguide at the pump and SH wavelength can be matched by finding the right waveguide geometry (modal phase matching).

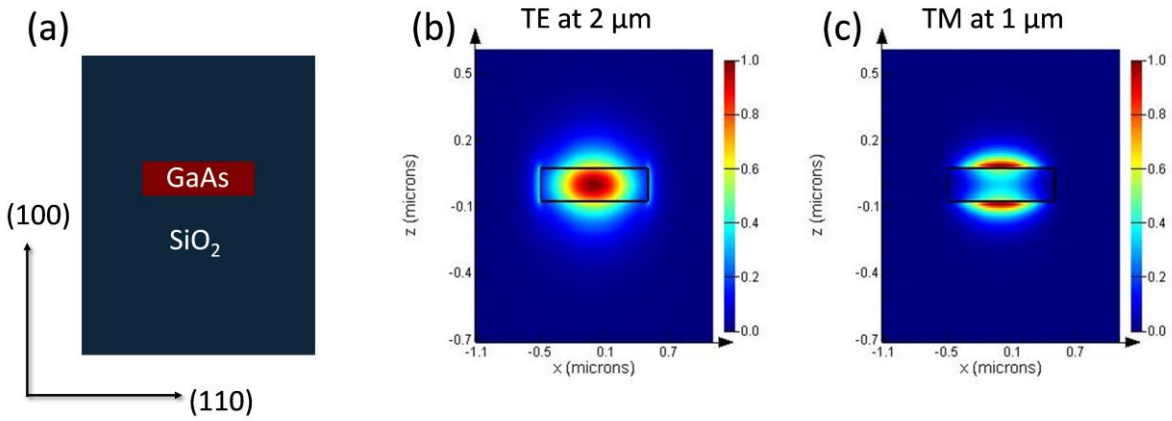

Figure. 4.4: Nonlinear waveguide design: (a) Waveguide cross section geometry; (b) Mode distribution of fundamental TE mode at 2 µm wavelength; (c) Mode distribution of fundamental TM mode at 1 µm wavelength.

The schematic cross section of a GaAs waveguide for SHG is shown in Fig. 4.4(a). Here, we designed a waveguide to achieve SHG when using a fundamental pump wavelength of 2 µm. Fig. 4.4(b) and (c) show the simulated mode distributions for the fundamental TE and TM modes at 2 and 1 µm wavelength, respectively. The effective refractive indices of the two modes is matched by tailoring the thickness and width of GaAs waveguide. Fig. 4.5(a) shows the relation between the waveguide thickness and width to achieve phase matching for a pump wavelength of 2 µm – a thicker GaAs film requires a wider waveguide to fulfill the phase matching condition. For our purposes, we chose a GaAs thickness of 150 nm, which corresponds to a waveguide width of 1.5 µm. This is a compromise between a relatively narrow waveguide to achieve a high intensity, while not too small to cause increased propagation loss due to scattering from the waveguide sidewalls. Fig. 4.5(b) shows the effective indices of the two modes as a function of waveguide width. Phase matching is fulfilled at the intersection point of the two curves.

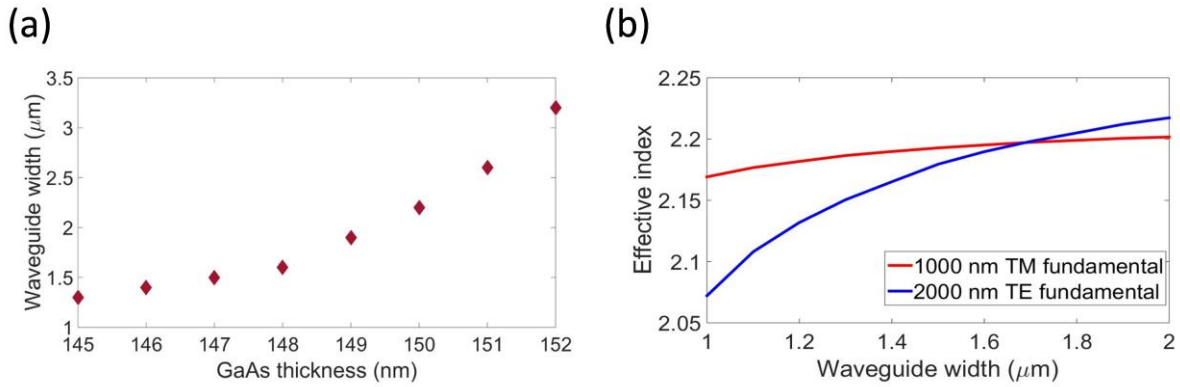

Figure. 4.5: (a) Required waveguide width to achieve phase matching for SHG at a fundamental wavelength of 2 µm as a function of the GaAs thickness; (b) Effective indices of the pump and SH

modes as a function of the waveguide width for a GaAs thickness of 150 nm at wavelengths of 2 µm and 1 µm.

The calculated normalized efficiency for the chosen waveguide geometry is 32,000% $W^{-1}cm^{-2}$. This value is one order of magnitude higher than previous reported numbers of thin film $LiNbO_3$ platform [14]. This significant increase is mainly caused by two factors: the higher nonlinear coefficient and the smaller mode size. When one compares the GaAs platform to the thin film $LiNbO_3$ waveguide platform, it can be found that the GaAs waveguide has a 4-6 times higher $\chi^{(2)}$ (d_{14}) and 4 times smaller waveguide mode size. In addition, the modal phase matching gains a factor of $(\pi/2)^2$ [15] enhancement in efficiency when compared to QPM, because the SHG light is in phase with the pump wavelength along the whole waveguide length.

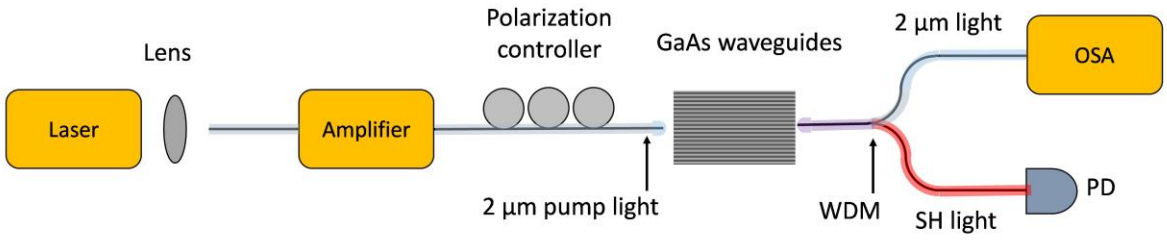

Figure. 4.6: Schematic of the SH characterization setup.

A schematic illustration of the nonlinear optical characterization setup is shown in Fig. 4.6. A 1975-2075 nm tunable CW laser (New Focus TLB6700) is used as light source. About 1 mW (0 dBm) power from the laser's free-space output is coupled into a 2 µm wavelength single mode fiber. The fiber coupled light passes through a 2 µm fiber amplifier (AdValue Photonics), which increases the pump power. A polarization controller is used afterwards to

align the polarization of the light so that the fundamental TE mode of the GaAs waveguide is excited when using a lensed fiber. The focal spot size of the lensed fiber is ~2 μm. The light from the waveguide output port is collected by another lensed fiber, which is connected to a wavelength-division multiplexer, splitting the pump and SHG light. The pump light is analyzed by an optical spectrum analyzer (OSA) and the SH power is measured by a Si photodetector, respectively.

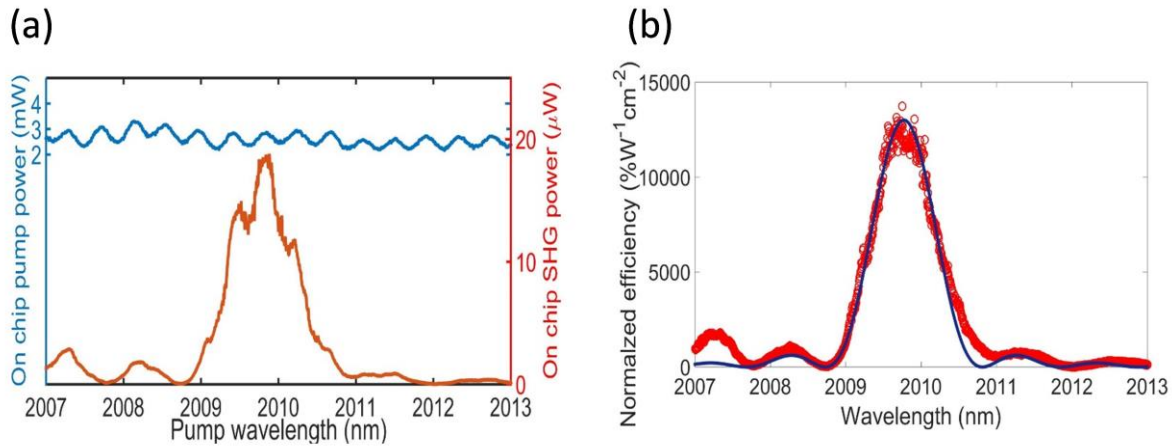

Figure. 4.7: Experimental results: (a) SHG and pump power as a function of the pump wavelength for a 1.4-mm-long waveguide with inverse taper input; (c) Single pass conversion efficiency extracted from (a).

The SHG characterization results for a 1.4-mm-long, 1.53-μm-wide waveguide are plotted in Fig. 4.7(a). The input port of the waveguide device is a 200-μm-long, 350-nm-wide waveguide, connected to the SHG waveguide section by a 100-μm-long linear taper. This was done to increase the coupling coefficient at input port, which is estimated to be around 0.45 (-3.5 dB) by experiment. The coupling coefficient for the pump and SHG light at the output port, which is a normal edge coupler with same waveguide width as the SHG

section, are estimated to be around 0.25 (-6 dB) by experiment and 0.3 (-5.2 dB) by FDTD simulation, respectively. No inverse taper was chosen on this side, as it is difficult to fabricate the desired waveguide width (150 nm) for the SH wavelength by our current lithography, which can be solved in future by using electron beam lithography. The fabricated waveguide has a propagation loss at the pump wavelength of approximately 1-2 dB/cm. This value was extracted by using the Fabry-Perot method [16] and verified by the quality factor of a ring resonator with same waveguide geometry. The low waveguide loss is a result of the smooth waveguide sidewalls (see Fig. 3 (b)), top and bottom surface (RMS ~0.3 and 0.2nm). Figure 4.7(a) presents the pump (P_{ω}) and SHG power ($P_{2\omega}$) as a function of the pump wavelength, where the plotted powers refer to the power levels inside of the waveguide. Figure 4.7(b) shows the normalized efficiency of this waveguide (Red dots), which is extracted based on the formula $P_{2\omega}/(P_{\omega}L)^2$. The maximum single pass conversion efficiency of this waveguide is about 250% W^{-1}, which corresponds to a normalized efficiency of 13,000% $W^{-1}cm^{-2}$ for a 1.4 mm long waveguide. The blue curve shows a plot of $sinc^2$ function fitted to experimental result, which indicates that the spectral shape of the measurement result closely matches the theoretically expected function. The fitted full width at half maximum (FWHM) bandwidth of the $sinc^2$ function is 0.93 nm, which is very close to the theoretical prediction of 0.90 nm, indicating good agreement.

The transmission spectra of the fundamental wavelength in Fig. 4.7 (a) shows periodic ripples, caused by the waveguide end faces, which form a low-finesse Fabry-Perot cavity. This resonance enhances the fundamental power and therefore also the generated SH power inside of the waveguide as evident in Fig. 4.7 (a) by the periodic ripples in the fundamental and SH power. The extinction ratio of the Fabry-Perot ripples is ~1 dB, which corresponds to a 0.5 dB enhancement of peak power compared to the power coupled into waveguide. As

a result, the resonance enhanced SHG efficiency (~300% W^{-1}) is about 1 dB higher than the single pass efficiency. By increasing the reflectivity of the facets, the resonance enhanced conversion efficiency can even further be improved due to the low propagation loss of the waveguide.

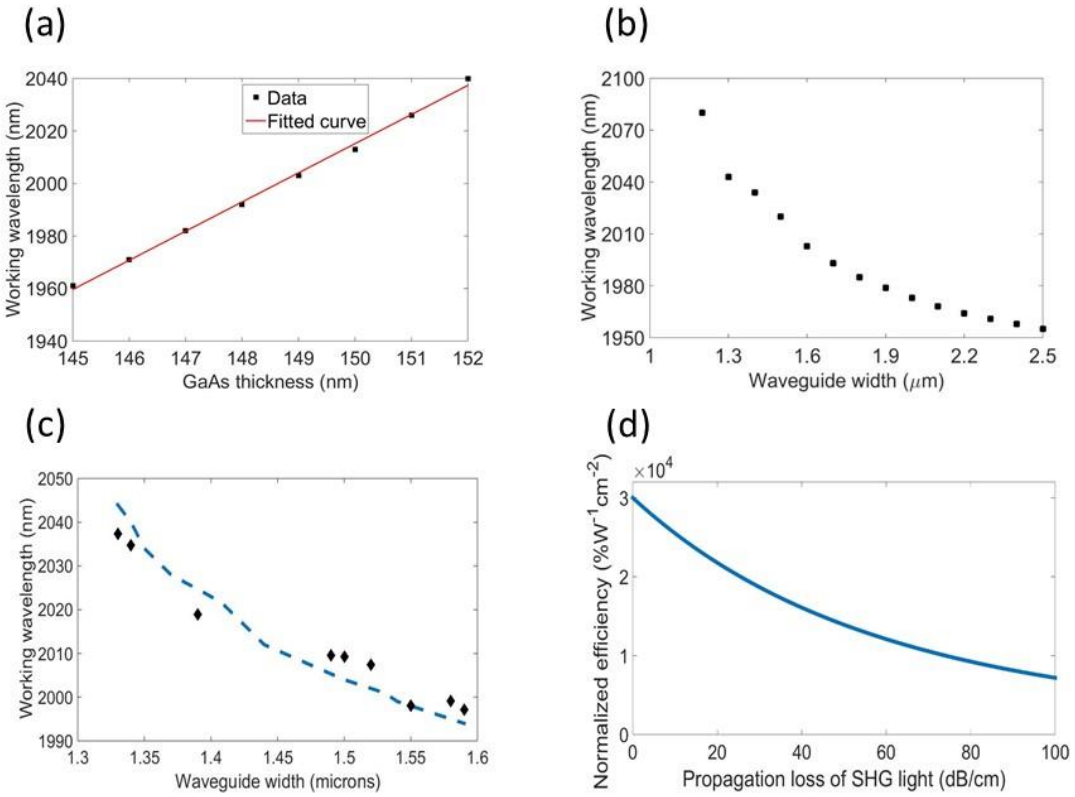

Figure. 4.8: Dependence of phase matching wavelength on the GaAs waveguide (a) thickness and (b) width; (c) Phase matching wavelength of waveguides with different widths - the black diamonds represent measurements, the blue dashed line represents simulation results; (d) Calculated efficiency over propagation loss of SH light for 1.4-mm-long waveguide, assuming 2 dB/cm loss at pump wavelength.

The normalized efficiency that we achieved (13,000% $W^{-1}cm^{-2}$) is about 2.5 times smaller compared to the simulated normalized efficiency (32,000% $W^{-1}cm^{-2}$) for the chosen waveguide geometry. A few factors may cause this discrepancy. One reason for this efficiency drop could be the non-uniformity of the GaAs waveguide geometry, especially the variation of the GaAs thickness. Figure 4.8 (a) plots the phase matching wavelength of a 1.5-μm-wide waveguide as a function of different GaAs thicknesses. It can be seen that a 1 nm change in thickness causes an 11 nm shift in the phase matching wavelength. This indicates that the GaAs thickness must be extremely uniform over the propagation length in order to achieve high conversion efficiencies. The variation of waveguide width is another uniformity concern that can impact the nonlinear optical efficiency of the waveguide. According to Fig. 4.8 (b), a 10 nm change in width shifts the phase matching wavelength by 1 nm. For characterizing the uniformity of the waveguide geometry, a chip with a size of 2.8×10 mm^2 was fabricated. The chip accommodated waveguides with different widths. The phase matching wavelength of each waveguide was tested and compared to the calculated phase matching wavelength, as shown in Fig. 4.8 (c). It can be seen that the maximum deviation of the working wavelength from the simulation is approximately 5 nm. When we assume that the working wavelength shift is predominantly caused by waveguide thickness (width), the maximum GaAs thickness (width) non-uniformity over the cm-scale chip scale is about ±0.5 nm (±50 nm). This result, along with the good fit between the measured and the theoretical bandwidth, suggest that other factors may be dominant to cause the lower measured conversion efficiency of our waveguides.

Another reason for the discrepancy between the calculated and the measured conversion efficiency is the high propagation loss of TM light at the wavelength of 1 μm. Previous reports that used AlGaAs waveguides for SHG [9], [17] found a ten times higher

propagation loss at the SH wavelength, compared to the loss at fundamental wavelength. In Fig. 5 (d) we plotted the dependence of efficiency for a 1.4-mm-long waveguide as a function of the propagation loss at a wavelength of 1 μm, assuming 2 dB/cm propagation loss at pump wavelength. It can be seen that the loss at the SH wavelength can cause a significant drop in the conversion efficiency for loss levels in the order of tens of dB/cm. According to our cut-back measurements, the propagation loss for the TM light at 1 μm waveguide is around 22 dB/cm, which causes a drop of ~25% in normalized efficiency.

Another factor that could have caused the discrepancy between the calculated and the measured SHG conversion efficiency is that we estimated the coupling for SH light based on the simulation results, which may overestimate the SH coupling efficiency and underestimate the conversion efficiency. It should also be noted that there is an uncertainty about the nonlinear coefficient of GaAs. We used Miller's rule to estimate the nonlinear optical coefficient at a wavelength of 2 μm from the measurements reported in Refs. [18], [19], which seem to be fairly consistent with each other. However, older references report even higher nonlinear optical coefficients of GaAs [6].

4.4. Micro-resonators for SHG and OPO

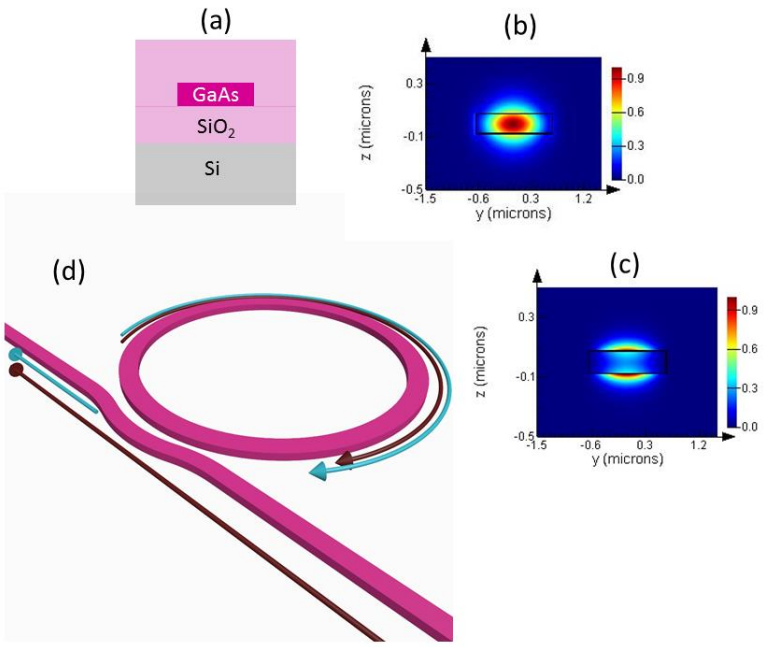

Figure. 4.9: (a) Cross section of GaAs on insulator waveguide; (b) and (c) electric field distributions for fundamental TE mode at a wavelength of 2 μm and TM mode at a wavelength of 1 μm; (d) schematic structure of ring resonator with pulley coupler.

With the highly efficient SHG waveguide we demonstrated in last section, the resonance structure can further the SHG efficiency [20], [21]. The cross section of the nonlinear optical waveguide is illustrated in Fig. 4.9 (a), where the waveguide core material (<001> oriented GaAs) is fully surrounded by silica. We choose a SHG process in the GaAs waveguide between TE-polarized pump light and TM polarized second harmonic (SH) light, determined by the non-zero susceptibility elements of the $\chi^{(2)}$ tensor. One of the key requirements for high-efficiency SHG is the phase match condition, which in <001> oriented GaAs ring resonators, can be fulfilled by [22]:

$$\left|2m_P - m_{SH}\right| = 2 \tag{4.4.1}$$

Where m_p and m_{SH} correspond to the azimuthal numbers of pump and SH light, respectively. The azimuthal number follows the relation:

$$\omega_{P,SH} \times n_{P,SH} / c = m_{P,SH} / R \tag{4.4.2}$$

Where $\omega_{P,SH}$ are the frequencies of pump and SH light, $n_{P,SH}$ are the effective indices of modes at those two frequencies and R is the radius of the ring resonator. From Eq. (4.4.1) and (4.4.2) the relations between n_P and n_{SH} can be obtained:

$$n_{SH} = (1 \pm \frac{1}{m_P}) n_P \tag{4.4.3}$$

This relation indicates that, compared to the modal phase match used in straight waveguide, where n_P and n_{SH} should be exactly matched, here we have an offset factor of $1/m_P$ between the indices at two wavelengths. In this work, the radius of the resonator we used is 100 μm, which correspond to an m_P value around 650 and m_{SH} around 1300±2. As a result, $1/m_P$ is much lower than 1, which means that we can design the waveguide geometry to match the two indices very closely, similar for the case of straight waveguide. Here we pick the waveguide of the resonator to be 150 nm thick and 1300 nm wide, which corresponds to a phase match wavelength of ~ 2 μm. The profile of the TE mode at a wavelength of 2 μm and TM mode at a wavelength of 1 μm are shown in Fig. 4.9 (c) and (d), respectively.

The ring resonator is coupled to the bus waveguide with a pulley coupler, as illustrated in Fig. 4.9 (d). The width of bus waveguide is 900 nm and the gap between bus and ring waveguides is 200 nm. These geometries mean that the resonator is highly under coupled for both wavelengths. To achieve the highest external conversion efficiency of the resonator,

one ideally has both wavelengths critically coupled [23]. However, increasing the coupling requires that either the coupling length is increased, or the gap-size is reduced between the waveguides. We did not pursue either option as a longer coupling length will impact the phase matching condition in the resonator and the gap-size was limited by the lithography step used to define the waveguides.

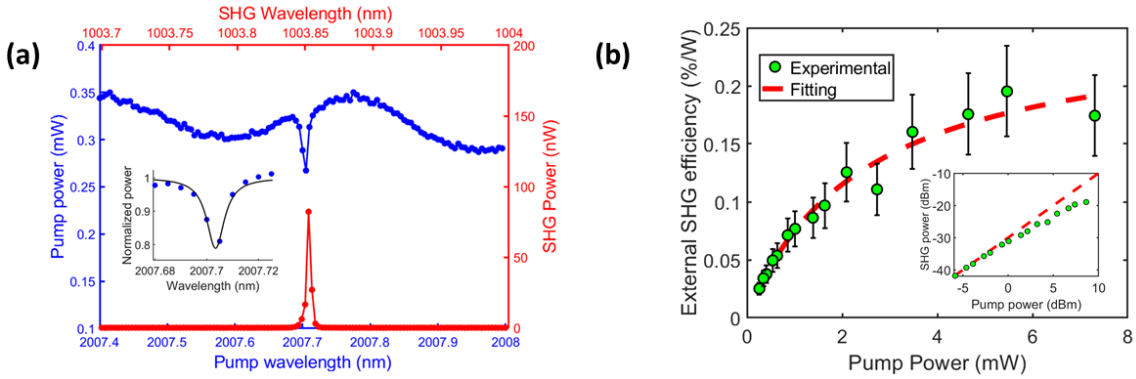

Figure. 4.10: Experimental results and analysis: (a) pump and SHG spectrum for the ring resonator, the embedded figure shows the zoomed in resonance and fitting curve; (b) dependence of external SHG conversion efficiency on the pump power, experimental results and calculation from Eq. 5, the embedded figure shows the SHG power as a function of the pump power, experimental results are compared to the case of no depletion (red dash line).

Experimentally, we characterized the devices by coupling pump light with a wavelength of around 2 μm into the bus waveguide and detect the transmitted power at the pump and SHG wavelength after splitting them using a wavelength demultiplexer. Fig. 4.10 (a) shows the wavelength response of the ring resonator for the pump light and the corresponding SH light inside the bus waveguide as a function of the pump wavelength. Based on the full width at half maximum (FWHM) (8 pm) of the fitted resonance (see inset in Fig. 4.10 (a)) at the

pump wavelength, we estimate the intrinsic quality factor of the ring resonator to be higher than 2.6×10^5 around 2 μm wavelength. This corresponds to a linear propagation loss of below 2 dB/cm. A measurement with a finer spectral resolution is currently limited by the wavelength step size of our laser. The quality factor at 1 μm is estimated to be around 5.7×10^4, based on the propagation loss (22 dB/cm) extracted from cutback measurement.

Fig. 4.10 (a) also shows that the SH power is only detected at the resonance of the pump light. The pump power P_P and SHG power P_{SH} inside the bus waveguide are estimated based on the waveguide to fiber coupling coefficients at the chip facets of 56% and 12.6%, respectively. The coupling structures are the inverse tapers designed for 2-μm light. The design of more efficient edge couplers at the SHG wavelength can be realized by using EBL lithography in the future, in which case the coupling coefficient is expected to be higher than 60%. The inset of Fig. 4.10 (b) shows the P_{SH} as a function of P_P. The red dashed line has a slope of 2 in dB scale, which corresponds to the case of having no pump power depletion. The green dots represent the experimental results, where the deviation from the red line occurs at a pump power of less than 1 mW inside the bus waveguide, of which < 200 μW power is coupled into the resonator. This indicates that a significant frequency conversion takes place inside the cavity at very low pump powers as the pump gets depleted.

The external normalized SHG efficiency for this device is around 100%/W at low pump power region, which is orders of magnitude higher compared to the efficiency of previous research on GaAs (AlGaAs) microdisks [24], [25]. When one considers that the ring resonator is highly under-coupled at both pump and SHG wavelength, the internal conversion efficiency is a better parameter for characterizing the cavity's capability for frequency conversion. Here the internal efficiency refers to SHG efficiency inside the cavity. To extract that, we use the model in Eq. (2.1.31), the correlation between η_{SH} and P_P can be built, with

two unknown constants r_{SH} and P_0. P_0 is the characteristic power constant indicating the point higher than which the depletion starts to be significant. The value of r_P can be extracted from the spectrum of pump resonance.

Fig. 4.10 (b) shows the plot of η_{SH} as a function of P_P. By fitting the model Eq. (2.1.31) based on the experimental results (green dots), we extracted the values of r_{SH} and P_0 to be 0.05 and 0.4 mW, which correspond to the red dashed curve. It can be seen that the experimental results match well with the theory. Here, we did not include the nonidealities of the cavity into our model, which will be discussed afterwards.

The following equation is used to estimate how much of the pump power that is coupled into the cavity is frequency doubled:

$$\eta_{SH\_in} = \frac{1+r_{SH}}{r_{SH}} \frac{P_{SH}}{P_P - P_{P\_t}} \tag{4.4.4}$$

Where P_{P_t} is the transmitted power of pump light, which can be determined by our experimental results. When there is 0.34 mW pump power inside bus waveguide, 61 μW of it is coupled into cavity. The internal conversion efficiency in this situation is estimated to be 4% based on Eq. (2.1.31), which correspond to an internal normalized efficiency around 65,000 %/W. Such a high internal conversion efficiency can be explained by the high nonlinear optical coefficients of GaAs compared to those of other $\chi^{(2)}$ resonators, the tight mode confinement, the efficient phase-matching and the high quality factors we achieved in this platform.

To calculate the ideal conversion efficiency for a GaAs ring resonator, it is hard to use Eq. (2.1.31) directly as *d* is not a constant value for a ring resonator due to waveguide bends. In Ref.[22], a detailed theoretical analysis has been done to deal with this problem, which will be referred to in the following.

In the low pump power region, for an ideal GaAs ring resonator, with critical couples and aligned resonances, the expected SHG power coupled outside the resonator is:

$$P_{SH} = (P_P)^2 (1-|t_{SH}|^2) \frac{|2\pi K_{\pm}|^2 \alpha_{SH}^2}{(1-\alpha_{SH}|t_{SH}|)^2} \left(\frac{\alpha_f^2 (1-|t_f|^2)}{(1-\alpha_f |t_f|)^2} \right)^2 \tag{4.4.5}$$

Where $K_{\pm}$ is the nonlinear coupling coefficients for $\Delta m = \pm 2$. In a cylindrical coordination system, it can be expressed as:

$$K\pm = \mp \frac{d_{14}}{2\varepsilon_0 \omega_0 n_P^4} \int_{-\frac{h}{2}}^{\frac{h}{2}} \tilde{Z}_{SH}(z) \tilde{Z}_P^2(z) dz \times \cdots$$
$$\times \int_{-\frac{w}{2}}^{\frac{w}{2}} r \tilde{\psi}_{SH} \left(\frac{m_P}{r} \tilde{\psi}_P \pm \frac{\partial \psi_P}{\partial r} \right)^2 dr \tag{4.4.6}$$

Where $\Psi(r)$ and $Z(z)$ come from the expression for the field distribution ($F_z = H_z$ *or* E_z) of the mode:

$$F_z \exp(i\omega t) = A(\theta)\psi(r)Z(z)\exp[i(\omega t - m\theta)] \tag{4.4.7}$$

For more details, please refer to Ref. [22]. Here, we solve the modes numerically by using Lumerical FDTD. Then through Eq. (4.4.6) we obtain the value of K_+ and K_- to be 0.0575 $W^{-1/2}$ and 0.042 $W^{-1/2}$, respectively. The external normalized conversion efficiencies are estimated to be 68,445 %/W and 36,504 %/W, respectively, which is about four times higher than the value we estimated above.

A possible reason for this discrepancy may be due to the uniformity or defects inside the cavities. Another factor which may also affects the efficiency is the mismatch between resonances, either caused by the initial structure of the ring or the thermal effect when injecting high power into the cavity. According to Ref. [26], when taking the resonance detuning into consideration, the conversion efficiency expression becomes:

$$\eta_{SH} = 4\frac{r_{SH}}{\delta_{SH}^2 + (1+r_{SH})^2}\left(\frac{r_P}{\delta_P^2 + (1+r_P)^2}\right)^2 \frac{P_P}{B} \tag{4.4.8}$$

Here $\delta_P = (\omega_{p\_r} - \omega_P)/\alpha_P$ ($\delta_{SH} = (\omega_{SH\_r} - 2\omega_P)/\alpha_{SH}$), ω_{p_r} and ω_{SH_r} correspond to the resonances of pump and SHG frequency, respectively. $\delta_P = 0$ because the pump wavelength at which we extracted the efficiency is very close to the resonance as shown in Fig. 3(a). δ_{SH} indicates the mismatch between SHG wavelength and the resonance. The conversion efficiency reaches the maximum when both pump and SHG wavelength are perfectly resonant and drops significantly when the mismatch between two resonances increases. The power built up in the cavity may cause strong thermal optic effect to shift the resonances, which may influence the conversion efficiency under different pump powers. In this experiment, at low pump power levels where the highest conversion efficiency is extracted, we did not observe an obvious thermal shift of the resonance. When the pump power was increased, the thermal shift could be observed and the pump wavelength was adjusted to follow it, whose maximum value ($^{\triangle\omega_{p\_r}}$) at highest power level is 2π × 6.4 GHz. Assuming that the dependences of resonance shifts on temperature are similar with results in Ref.[25], where $(2\triangle\omega_P)/(\triangle\omega_{SH} - 2\triangle\omega_P) = 0.077/(0.083 - 0.077) = 12.8$, we estimate the value of δ_{SH} to be ~0.1. Then by plugging δ_{SH} into Eq. (4.4.8), the maximum drop of the efficiency caused by thermal effect in this work is less than 1%.

Another factor that can influence the efficiency is the nonlinear loss. According to Ref.[27], the two photon absorption (2PA) of GaAs at 2 μm is negligible, and the three photon absorption (3PA) is ~2 cm^3/GW^2, which leads to a nonlinear loss less than 0.001 dB/cm inside the cavity under the highest power level in our experiment. This indicates that here the nonlinear loss is not a main contributor to the drop of efficiencies compared to other

factors. However, for the nonlinear applications pumped at the wavelength below 1.8 μm, GaAs will have strong 2PA loss. In that case, using AlGaAs with larger bandgap will be a better option. Furthermore, one also needs to keep in mind that GaAs can form a native oxide layer at the surface during processing, which can form interface states within the bandgap, causing additional losses [28]. Such losses can be reduced by appropriate surface passivation [13].

To further improve the conversion efficiency, a race track resonator will be a better choice compared to the ring resonators, as the phase matching condition can truly be fulfilled along the straight waveguides rather than relying on the quasi-phase matching approach in a ring resonator. If the straight section is much longer than the curved section, and aligned to the direction where the SHG interaction correspond to the non-zero susceptibility elements of the $\chi^{(2)}$ tensor, we can treat the resonator by a constant nonlinear coefficient d_{14}. For such a resonator with 1 mm perimeter, at 2 μm pump wavelength, v_P = 150 THz, $n_{P,\,SH}$ = 2.2, d_{14} = 104 pm/V, $Q_{0P} = 2.6 \times 10^5$, $Q_{0SH} = 5.7 \times 10^4$, $V_P^2 V_{SH}/V_{PPSH}^2$ = 2400 μm^3 and assuming $r_{P,SH}$ = 1, we estimate the normalized external efficiency at low power region to be 1,830,000%/W based on Eq. (2.1.31) and (2.1.31).

This strong frequency conversion indicates the great potential for resonators on this platform for on-chip nonlinear applications. A significant amount of power can be converted to the second harmonic wavelength even with a pump power below one milliwatt. These properties can make many currently inaccessible on-chip nonlinear systems with limited power budget possible, such as the on-chip self-reference of frequency comb [29], in which the pump power of the comb teeth for frequency doubling is around 10 μW. For optical parametric oscillators (OPO), the resonance structures will lead to an ultralow threshold at several micro-watts, which can readily be satisfied by the current integrated lasers and will

also bring huge benefits to quantum applications as the filtering requirements of the pump power can be relaxed [30].

4.5. Micro-resonators for frequency comb generation

The strong third order nonlinear coefficient of (Al)GaAs according to Table. 4.1 indicates a great potential for frequency comb generation on (Al)GaAsOI platform. Compared to the commonly used SiN or SiO_2 resonators, the requirement of quality factor is greatly relieved. As a result, standard foundry-based fabrication procedures can be directly used. In this section, we focus on a comb operating at C band from AlGaAs resonators.

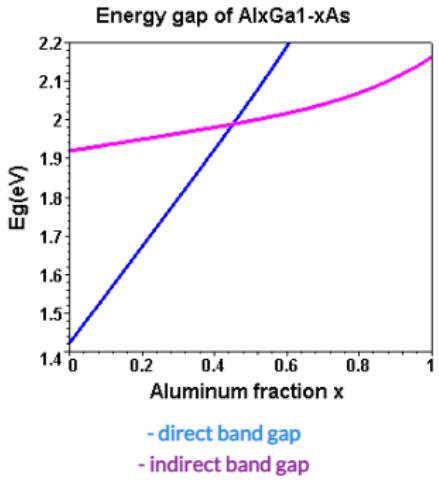

Figure. 4.11: Energy bandgap of AlGaAs [31].

One difference of the nonlinear devices operating below 1700 nm, compared to the SHG devices we discussed in previous sections, is that the material choice needs to be AlGaAs rather than GaAs to avoid TPA. Fig. 4.11 is the plots for the bandgap of $Al_xGa_{1-x}As$ as a function of the Al portion. It can be found that x needs to be set to higher than 0.15 to have bandgap larger than 1.61 eV, which correspond to a wavelength of 770 nm. In this work, we

set the Al portion to be 0.2 so that the band extended to 1.67 eV (743 nm), so that the whole C band won't suffer from TPA.

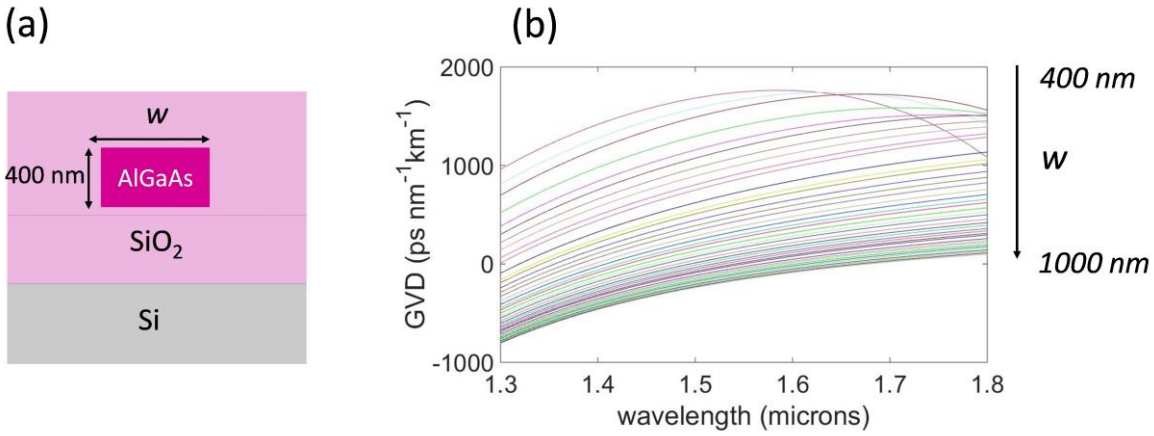

Figure. 4.12: (a) Schematic drawing of the waveguide for comb generation; (b) Simulated dispersion results under different waveguide widths.

For Kerr comb generation, an essential requirement based on the discussion in Section 2.2 is that the GVD of waveguides need to be positive (anomalous dispersion) at the pump wavelength. Fig. 4.12 shows the cross section and the simulation of GVD for $Al_{0.2}Ga_{0.8}AsOI$ waveguides on a 400 nm thick platform with different waveguide with. It can be found that for narrower waveguides the zero GVD point is blue shifted, which is preferred for broad comb generation. However, the narrower waveguide usually has higher propagation loss due to the sidewall scattering, which increases the power required for comb generation. In practice, a trade off needs to be made for that. In this work, we choose waveguide width to be around 800 nm width, whose zero-GVD wavelength is around 1450 nm.

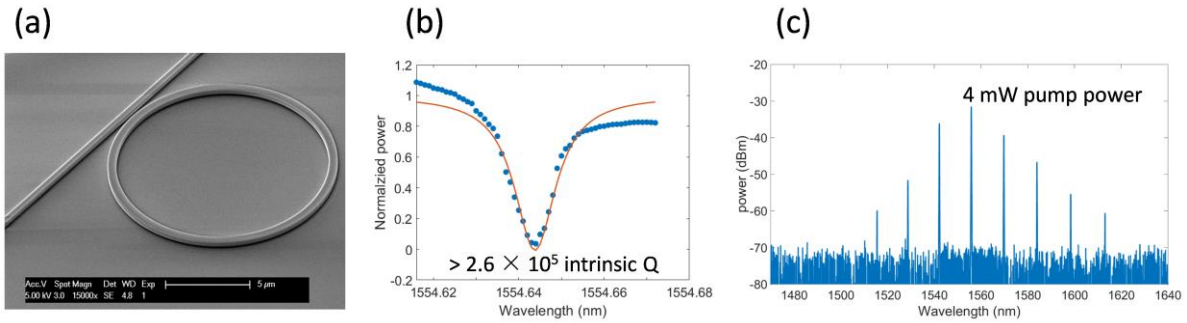

Figure. 4.13: (a) SEM image of the resonator; (b) Spectrum of the resonace for the resonator by using old fabrication process; (b) Frequency comb generation under 4 mW pump power inside bus waveguide.

We fabricated several runs of devices for comb generation. For the first set of chips whose fabrication procedure is exact the same with what we applied for SHG device, the Q is around 2.6×10^5 for a resonator with 15 μm radius, as shown in Fig. 4.13 (b). And the threshold power for comb generation is around 2 mW power inside bus waveguide, which is comparable with other efficient nonlinear platforms [4], [32].

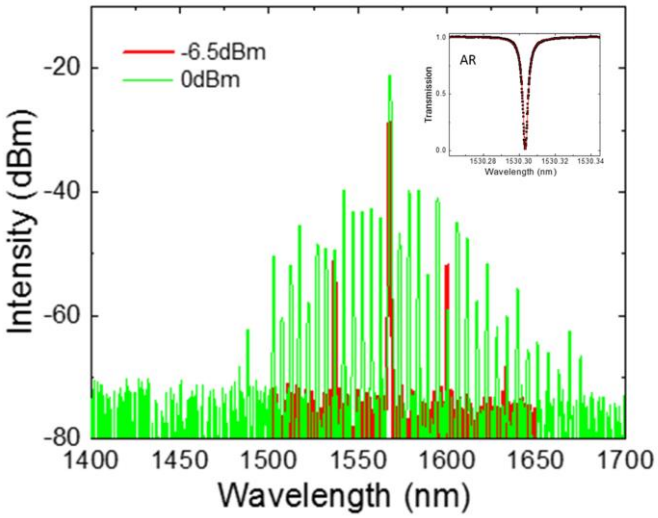

Figure. 4.14: Frequency comb generation by the resonator with optimized fabrication process. Green and red plots correspond to pump power of 1 mW and 220 μW inside bus waveguide. The inset is the resonance transmission spectrum.

To further enhance the efficiency of the comb generation, the quality factor of the resonator needs to be further improved. We optimized the fabrication procedure and then made new devices, which show much higher quality factor compared to previous resonators. The inset of Fig. 4.14 shows the transmission spectrum of one new resonator with 30 μm radius and same cross section as before. The Q is up to 1 million, which correspond to an extremely low propagation loss of 0.55 dB/cm. For such kind of high Q resonators, the measured threshold for comb generation is down to 220 μW pump power inside bus waveguide, under which the spectrum is shown in Fig. 4.14. Under only 1 mW pump power, the comb generation can already cover more than 200 nm spectrum range.

Such resonator is one of the most efficient Kerr comb generators demonstrated so far. And according to calculation, the threshold power can be further lowered to sub-100 μW level under current Q. The reason of this discrepancy may be due to the design of waveguide's geometry. Moreover, the next step is to demonstrate the soliton formation, which is expected to happen under sub-milliwatt level considering the low threshold power we obtained.

4.6. High Q resonators

The (Al)GaAsOI waveguides in this platform are delivering unpreceded low propagation loss for fully etched III-V nanowires. Furthermore, there will be great advantages if waveguides with even lower loss can be obtained, for many other applications on this

platform, which may not be strictly limited by the phase match or dispersion requirements. For example, a narrow linewidth semiconductor laser requires a long photon life-time of the cavity, which is enabled by low loss waveguide. Other applications, such as optical buffer technology [33] or optical gyroscopes [34], also demand very low propagation loss. Overall, such waveguides provide efficient links connecting all the individual photonic components together to form the whole networks in PICs.

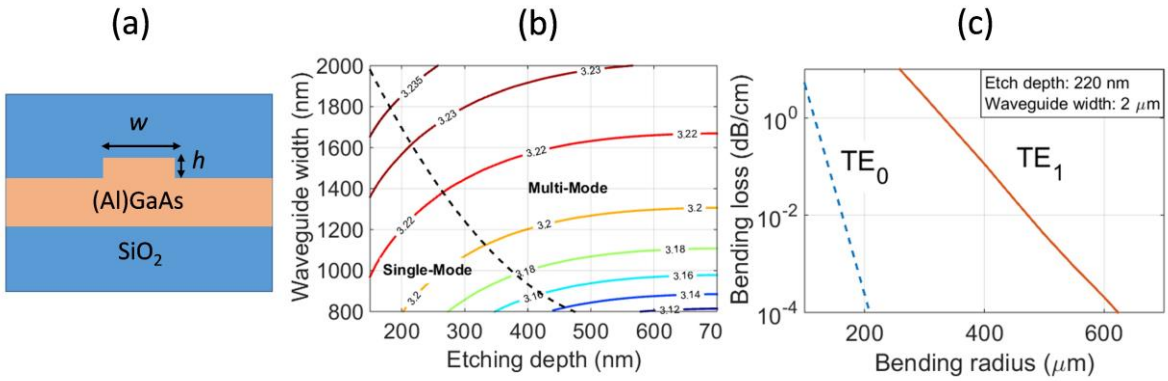

Figure. 4.15: (a) Schematic drawing of waveguide cross section; (b) Simulated effective index contour for GaAs waveguides; (c) Simulated bending loss for GaAs waveguide in this work.

Here we show one type of (Al)GaAsOI waveguide which can lead to a much lower propagation loss compared to those of fully etched ones. A schematic drawing of waveguide's cross section is shown in Fig. 4.15 (a). The waveguide core is (Al)GaAs, fully cladded with SiO_2. A shallow rib waveguide structure was chosen to reduce the interaction between optical mode and the etched sidewall, reducing scattering loss and therefore the overall loss of the waveguide. The thickness of the (Al)GaAs layer is 700 nm, which enables a high optical confinement of the waveguide mode in the vertical direction.

For such waveguide, the width *w* and etching depth *h* are two parameters that can be tailored according to specific applications. Fig. 4.15(b) presents a map of the effective index of the GaAs waveguides as a function of the width and the etch depth. It can be seen that an effective index above 3 can be achieved over a wide range, which is attractive as it enables the integration of vertically injected III-V lasers and tapers for efficient light transfer [35]. The region to the left of the dashed line represents the waveguide cross sections that support only the fundamental mode in TE polarization. A map for $Al_xGa_{1-x}As$ waveguide will be slightly different, depending on the concentration of Al in the alloy.

Another important factor needs to be taken into account when designing the waveguide geometry is the bending loss. Generally speaking, a shallower etched waveguide rib leads to a lower scattering loss. However, it also weakens the guiding of mode along horizontal direction, and thus increases the bending loss. In this work, we use an etching depth of 220 nm for our waveguides. This is about 30% of the total (Al)GaAs layer thickness, which is higher than the previously demonstrated ultra-low-loss SOI waveguide [35]. However, the larger etch depth enables a smaller bending radius and thus more compact devices. Figure 4.15(c) presents the bending loss as a function of the bending radius for the TE0 and TE1 waveguide mode. For a ring resonator with a radius of 250 μm, the bending loss limits the achievable intrinsic quality (Q) factor to around 5×10^7. Such a small radius will be beneficial for the compactness of PICs and reduce the complexity in the design of devices.

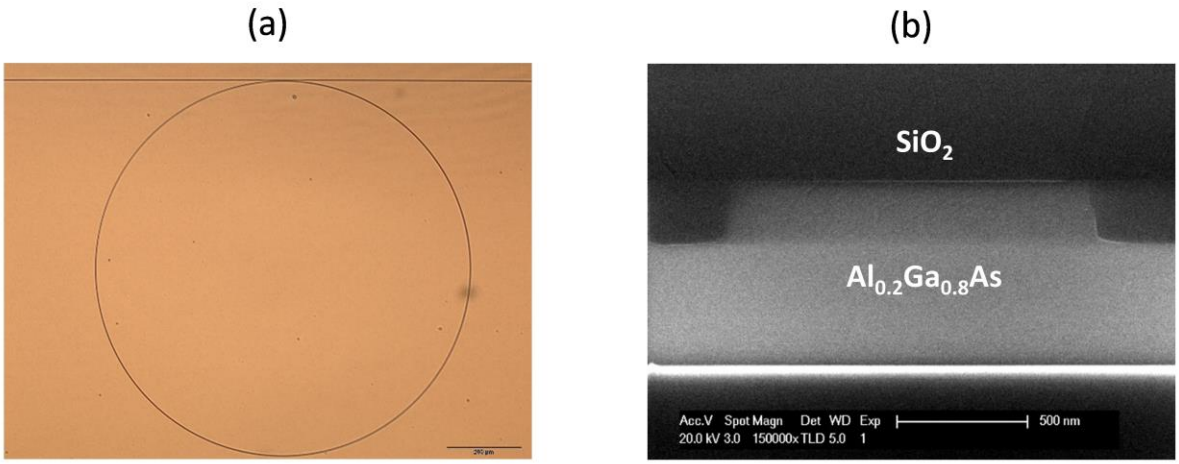

Figure. 4.16: Characteristic images of the device: (a) Microscopic top view of the resonator; (b) SEM image of the cross section of the $Al_{0.2}Ga_{0.8}As$ waveguide.

The fabrication for those waveguides is the same with the procedures for the SHG devices except the partial etch used instead of full etch. The microscopic image of the ring and the SEM image of the cross section of the waveguide is shown in Fig. 4.16 (a) and (b), respectively.

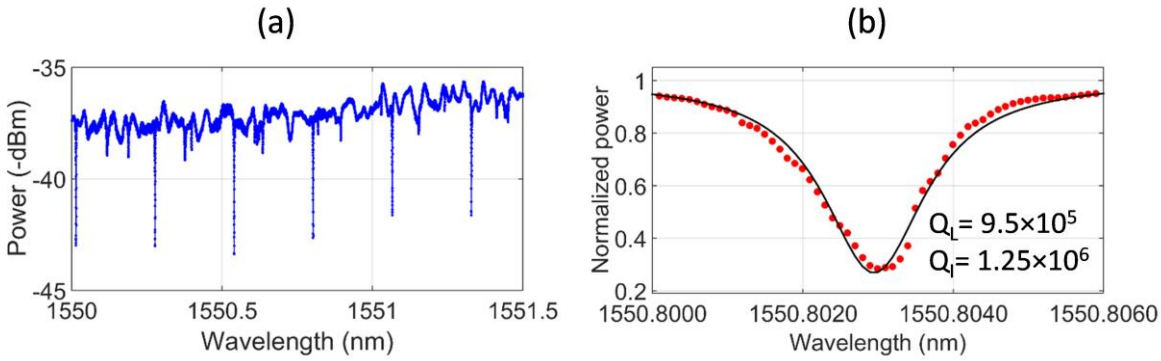

Figure. 4.17: Experimental results: (a) Resonance of GaAs on insulator resonator; (b) Zoomed in transmission spectrum the resonators in (a).

The spectral response of ring resonators been characterized to extract the propagation loss of the waveguides at C band. Fig. 4.17(a) shows the transmission spectrum of a GaAs ring resonator with a waveguide width of 2 μm and a radius of 500 μm. Fig. 4.17(b) shows the zoomed in spectral response of the resonance at a wavelength close to 1550.8 nm. The loaded and intrinsic quality factors of the resonator are 9.5×10^5 and 1.25×10^6, respectively, which correspond to a propagation loss around 0.5 dB/cm, much lower than the loss of fully etched waveguide using same fabrications. We haven't applied our new developed low loss process on those resonators, so that much higher Q can be expected in the future.

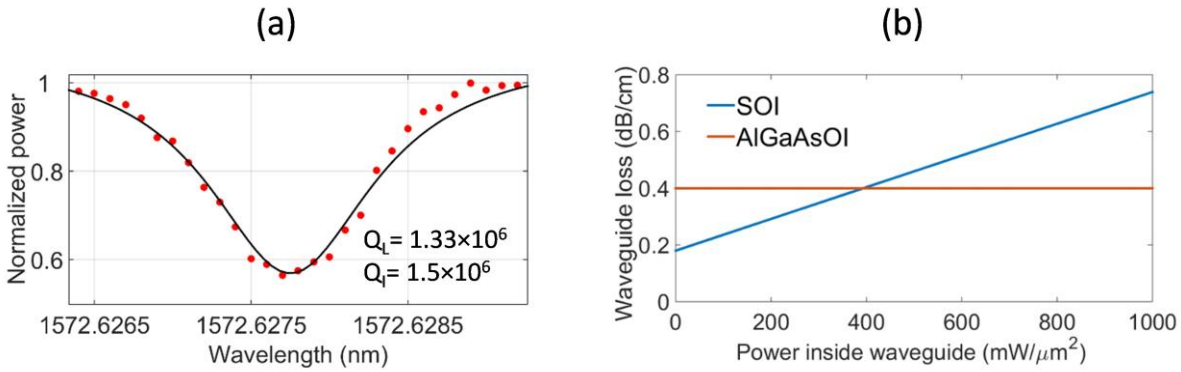

Figure. 4.18: (a) Experimental results of the resonance of $Al_{0.2}Ga_{0.8}As$ on insulator resonator; (b) Calculated waveguide loss for SOI waveguide (blue line) and AlGaAs on insulator waveguide (orange line) as a function of power intensity taking TPA at 1550 nm into account.

Fig. 4.18(a) shows the transmission spectrum of an $Al_{0.2}Ga_{0.8}As$ ring resonator, which has the same geometry as the GaAs resonator discussed above. The extracted intrinsic quality factor of this resonator is 1.5×10^6. The similar quality factors of the GaAs and $Al_{0.2}Ga_{0.8}As$ resonators indicate that a higher Al concentration does not degrade the material quality in

terms of optical waveguide loss. And the propagation loss is estimated to be around 0.4 dB/cm, one order of magnitude lower than traditional integrated III-V on silicon waveguides. Compared to the ultra-low loss SOI waveguide results in Ref. [35], in which 0.18 dB/cm propagation loss is obtained for the waveguide which is 500 nm thick with a 56 nm high, 1.8 μm wide rib, our propagation loss is two times higher. We believe that by reducing the etching ratio or increasing the rib width, the propagation loss can be further reduced to be similar or even lower than that of SOI waveguide.

To investigate the waveguide loss caused by TPA, we compare the $Al_{0.2}Ga_{0.8}As$ waveguide in this work with SOI waveguide, under different power intensity levels as shown in Fig. 4.18(b). It can be found that the demonstrated propagation loss of AlGaAs waveguides so far is higher when the waveguide is guiding a low amount of power, however for power intensity higher than 400 mW/μm^2, the waveguide loss in SOI waveguides exceeds that of the AlGaAs waveguide. For the resonator discussed in this work, at critical coupling, about 10 mW input power in bus waveguide can lead to such a level of power intensity inside the cavity, indicating that our waveguide will have a better performance even at the power level of current integrated laser.

According to previous work of GaAs microdisk [36] which have a quality factor up to 6 × 10^6, currently the loss of our waveguides are still limited by the process instead of material loss. To further improve the quality factor of the resonators, several steps of the fabrication can be further optimized. Better lithography and etch can reduce the roughness of sidewalls for lower scattering loss. And an efficient surface passivation can further suppress the photon absorption caused by defects state within the bandgap of the materials.

The high Q cavity and the low loss waveguide can be of significance in various applications. In traditional PICs, it can be used to construct ultra-narrow linewidth laser,

similar to what has been demonstrated in SOI platform [37], but with a simplified integration procedure because the low loss waveguide and gain medium can be integrated at the same time. In nonlinear photonics, a high Q AlGaAs waveguide cavity can significantly improve the efficiency of numerous nonlinear devices. Furthermore, this platform can enable the direct integration of active components such as laser on highly efficient nonlinear devices, paving the way for nonlinear PICs in the future. Many revolutionary demonstrations based on nonlinear optics, e.g. optical frequency synthesizer, optical atomic clocks, frequency comb spectroscopy, can be transferred into fully integrated PICs on single chip. In the field of quantum optics, the combination of high Q and high nonlinear waveguide provide the possibility to demonstrate the nonlinear process at single photon level. Given the fact that InAs quantum dots on GaAs is a very mature and widely used approach to generate single photons, and efficient second and third order nonlinear devices are good entangled photon generators, such a platform potentially can offer all the functionalities of a fully integrated quantum photonic circuits with great performance in the future.

4.7. Summary and outlook

In summary, we showed that the (Al)GaAsOI platform enables the state of the art efficient nonlinear process in both second and third order nonlinear effects. Such efficiency leads to significant frequency conversions under sub-milliwatt pump power, which is well below the power level provided by integrated semiconductor lasers. Furthermore, because the intrinsic compatibility of this platform with active devices, it paves a way to achieve fully integrated nonlinear PICs in the future.

Another significant meaning of this work is the demonstration of low loss III-V waveguides. Previously it was usually believed that III-V waveguides have much higher

propagation loss compared to SOI and dielectric waveguides, thus the performance of many devices is limited in pure III-V platforms. Our results prove that it is possible to reduce the previous high loss down to the level of the state of the art SOI waveguide level, at the same time eliminating TPA for high power operation and the simplification for laser integration. Those will lead to revolutionary changes to III-V photonic platforms in both research and industry.

Reference

[1] T. Komljenovic *et al.*, "Heterogeneous Silicon Photonic Integrated Circuits," *J. Light. Technol.*, vol. 34, no. 1, pp. 1–1, 2015.

[2] M. Savanier *et al.*, "Integrated cavity for a GaAs-based OPO," *CLEO Sci. Innov.*, p. JW4A.66, 2012.

[3] A. Boes, B. Corcoran, L. Chang, J. Bowers, and A. Mitchell, "Status and Potential of Lithium Niobate on Insulator (LNOI) for Photonic Integrated Circuits," *Laser Photonics Rev.*, vol. 12, no. 4, pp. 1–19, 2018.

[4] A. L. Gaeta, M. Lipson, and T. J. Kippenberg, "Photonic-chip-based frequency combs," *Nat. Photonics*, vol. 13, no. 3, pp. 158–169, Mar. 2019.

[5] B. Stern, X. Ji, Y. Okawachi, A. L. Gaeta, and M. Lipson, "Battery-operated integrated frequency comb generator," *Nature*, vol. 562, no. 7727, pp. 401–405, Oct. 2018.

[6] R. W. Boyd, *Nonlinear optics*. Burlington: Academic Press, 2008.

[7] M. Savanier *et al.*, "Near-infrared optical parametric oscillator in a III-V semiconductor waveguide," *Appl. Phys. Lett.*, vol. 103, no. 26, p. 261105, Dec. 2013.

[8] S. Mariani, A. Andronico, A. Lemaître, I. Favero, S. Ducci, and G. Leo, "Second-

harmonic generation in AlGaAs microdisks in the telecom range," *Opt. Lett.*, vol. 39, no. 10, p. 3062, May 2014.

[9] T. Matsushita, Y. Nakamura, S. Matsumoto, T. Onda, I. Shoji, and T. Kondo, "Fabrication of AlGaAs/Alox waveguides with inversion-stacked core structure for higher-order modal-phase matching devices," in *2013 Conference on Lasers and Electro-Optics Pacific Rim (CLEOPR)*, 2013, pp. 1–2.

[10] M. Pu, L. Ottaviano, E. Semenova, and K. Yvind, "Efficient frequency comb generation in AlGaAs-on-insulator," *Optica*, vol. 3, no. 8, p. 823, Aug. 2016.

[11] M. L. Davenport, L. Chang, D. Huang, N. Volet, and J. E. Bowers, "(Invited) Heterogeneous Photonic Integration by Direct Wafer Bonding," *ECS Trans.*, vol. 75, no. 9, pp. 179–183, Sep. 2016.

[12] L. Chang *et al.*, "Heterogeneously integrated GaAs waveguides on insulator for efficient frequency conversion," *Laser Photon. Rev.*, 2018.

[13] B. Guha *et al.*, "Surface-enhanced gallium arsenide photonic resonator with quality factor of 6 × 10^6," *Optica*, vol. 4, no. 2, p. 218, Feb. 2017.

[14] L. Chang, Y. Li, N. Volet, L. Wang, J. Peters, and J. E. Bowers, "Thin film wavelength converters for photonic integrated circuits," *Optica*, vol. 3, no. 5, p. 531, 2016.

[15] Li Gui, "Periodically Poled Ridge Waveguides and Photonic Wires in LiNbO3 for Efficient Nonlinear Interactions," University of Paderborn, 2010.

[16] T. Feuchter and C. Thirstrup, "High precision planar waveguide propagation loss measurement technique using a Fabry-Perot cavity," *IEEE Photonics Technol. Lett.*, vol. 6, no. 10, pp. 1244–1247, Oct. 1994.

[17] N. Morais *et al.*, "Directionally induced quasi-phase matching in homogeneous

AlGaAs waveguides," *Opt. Lett.*, vol. 42, no. 21, p. 4287, 2017.

[18] I. Shoji, T. Kondo, A. Kitamoto, M. Shirane, and R. Ito, "Absolute scale of second-order nonlinear-optical coefficients," *J. Opt. Soc. Am. B*, vol. 14, no. 9, p. 2268, Sep. 1997.

[19] T. Skauli *et al.*, "Measurement of the nonlinear coefficient of orientation-patterned GaAs and demonstration of highly efficient second-harmonic generation," *Opt. Lett.*, vol. 27, no. 8, p. 628, Apr. 2002.

[20] L. Chang *et al.*, "Strong frequency conversion in heterogeneously integrated GaAs resonators," *IPC postdeadline*, 2018.

[21] L. Chang *et al.*, "Strong frequency conversion in heterogeneously integrated GaAs resonators," *APL Photonics*, vol. 4, no. 3, p. 036103, Mar. 2019.

[22] P. S. Kuo and G. S. Solomon, "On- and off-resonance second-harmonic generation in GaAs microdisks," *Opt. Express*, vol. 19, no. 18, p. 16898, Aug. 2011.

[23] I. Breunig, "Three-wave mixing in whispering gallery resonators," *Laser Photonics Rev.*, vol. 10, no. 4, pp. 569–587, 2016.

[24] P. S. Kuo, J. Bravo-Abad, and G. S. Solomon, "Second-harmonic generation using 4-quasi-phasematching in a GaAs whispering-gallery-mode microcavity," *Nat. Commun.*, vol. 5, pp. 1–7, 2014.

[25] S. Mariani, a. Andronico, a. Lemaître, I. Favero, S. Ducci, and G. Leo, "Second-harmonic generation in AlGaAs microdisks in the telecom range," *Opt. Lett.*, vol. 39, no. 10, pp. 3062–5, 2014.

[26] X. Guo, C.-L. Zou, and H. X. Tang, "Second-harmonic generation in aluminum nitride microrings with 2500%/W conversion efficiency," *Optica*, vol. 3, no. 10, p. 1126, 2016.

[27] W. C. Hurlbut, Y.-S. Lee, K. L. Vodopyanov, P. S. Kuo, and M. M. Fejer, "Multiphoton absorption and nonlinear refraction of GaAs in the mid-infrared," *Opt. Lett.*, vol. 32, no. 6, p. 668, Mar. 2007.

[28] D. Parrain *et al.*, "Origin of optical losses in gallium arsenide disk whispering gallery resonators," *Opt. Express*, vol. 23, no. 15, p. 19656, Jul. 2015.

[29] D. T. Spencer *et al.*, "An optical-frequency synthesizer using integrated photonics," *Nature*, vol. 557, no. 7703, pp. 81–85, 2018.

[30] N. C. Harris *et al.*, "Integrated source of spectrally filtered correlated photons for large-scale quantum photonic systems," *Phys. Rev. X*, vol. 4, no. 4, pp. 1–10, 2014.

[31] "Energy band gap Eg of AlxGa1-xAs alloys." [Online]. Available: https://www.batop.de/information/Eg_AlGaAs.html.

[32] R. Summary, "Dissipative Kerr solitons in optical microresonators," *Science (80-.).*, vol. 8083, 2018.

[33] R. S. Tucker, Pei-Cheng Ku, and C. J. Chang-Hasnain, "Slow-light optical buffers: capabilities and fundamental limitations," *J. Light. Technol.*, vol. 23, no. 12, pp. 4046–4066, Dec. 2005.

[34] J. Li, M.-G. Suh, and K. Vahala, "Microresonator Brillouin gyroscope," *Optica*, vol. 4, no. 3, p. 346, Mar. 2017.

[35] M. A. Tran, D. Huang, T. Komljenovic, J. Peters, A. Malik, and J. E. Bowers, "Ultra-Low-Loss Silicon Waveguides for Heterogeneously Integrated Silicon/III-V Photonics," 2018.

[36] B. Guha *et al.*, "Surface-enhanced gallium arsenide photonic resonator with quality factor of 6 × 10^6," *Optica*, vol. 4, no. 2, p. 218, Feb. 2017.

[37] M. A. Tran, D. Huang, T. Komljenovic, J. Peters, and J. E. Bowers, "A 2.5 kHz

Linewidth Widely Tunable Laser with Booster SOA Integrated on Silicon," in *2018 IEEE International Semiconductor Laser Conference (ISLC)*, 2018, pp. 1–2.

Chapter 5

CMOS compatible nonlinear platforms

5.1. Background

The nonlinear platforms we discussed in last two chapters are delivering excellent performance for nonlinear applications. Besides the individual device level demonstrations, the (Al)GaAsOI platform also projects the future solutions for fully integrated nonlinear PICs. The current problem is that on that platform, besides the nonlinear components, many other photonic devices need to be developed, which requires time and efforts.

Another interesting approach to address the integrated nonlinear photonics system problem is adding nonlinear functionalities into CMOS compatible chips, where devices with different functionalities have been well developed. Heterogeneous integration offers the flexibility to integrate nonlinear materials onto those chips to realize the nonlinear PICs, bridging the current nonlinear research with the photonic foundry-based technology.

In a photonic CMOS platform, the materials used for building waveguide are usually Si and SiN [1]. For Si, even though it has large $\chi^{(3)}$ nonlinearity, the large TPA at telecom band makes it not desired for nonlinear applications [2]. SiN has lower material loss and larger transparent window, with no TPA at telecom band, which makes it attractive for $\chi^{(3)}$ process [3]. However, the essential problem for both Si and SiN is that they don't have $\chi^{(2)}$ effect. As

a results, the main focus of heterogeneous nonlinear photonics on CMOS platforms is to introduce large $\chi^{(2)}$ effect and take advantage of SiN for $\chi^{(3)}$ applications [4].

In this chapter, we will discuss the high quality SiN platforms for comb and supercontinuum generation. Based on this, integration of LN and (Al)GaAs onto SiN chips forms two state of the art CMOS compatible platforms for multi efficient nonlinear processes.

5.2. Silicon nitride nonlinear platform

5.2.1 Introduction

Si_3N_4 waveguides are popular for nonlinear photonics, like Kerr frequency comb and soliton generation [5]. Recently, a novel photonic Damascene process has been developed for fabricating high-confinement Si_3N_4 waveguides with high yield, mitigating common fabrication challenges [6]. The efficient stress control of this method can provide thick Si_3N_4 waveguides free of cracks, an essential prerequisite to achieve anomalous dispersion for comb and supercontinuum generations. Moreover, in this work we developed a top surface planarization method, which allows the integration of other nonlinear materials on the Si_3N_4 chips. In this session, we will focus on the $\chi^{(3)}$ process of Si_3N_4 waveguides alone. And in the next two sessions, hybrid LNOI-SiN and (Al)GaAsOI-SiN platforms will be discussed.

5.2.2 Frequency comb generation

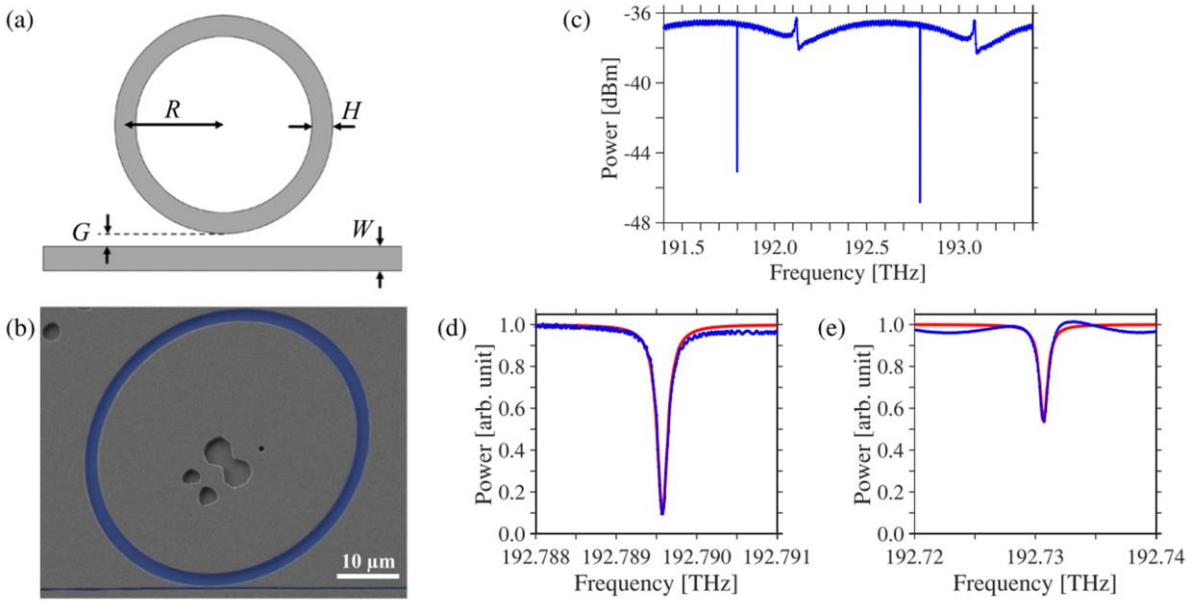

Figure. 5.1: (a) Top-view schematic and (b) SEM picture of the ring microresonator with the bus waveguide. The features visible in the central and the top left parts of (b) are remains of the stress relax checkerboard pattern. (c) Transmission spectrum measured at low EDFA power (−13 dBm) for a TE input polarization, and (d) fitting (in red) of the resonance near 192.8 THz (corresponding to a wavelength of ∼1555 nm). (e) Fitting (in red) of a resonance measured for a TM input polarization.

The devices for frequency comb generation are fabricated by low-pressure chemical vapor deposition (LPCVD) on a Si substrate. The photonic Damascene process [3] is used to deposit an 850-nm thick near stoichiometric Si3N4 layer on a prestructured substrate that includes a dense stress release pattern next to the actual waveguide pattern. Crack formation that causes high scattering losses in the waveguide is effectively prevented as the dense substrate topography suppresses stress buildup in the thin film. The Si_3N_4 waveguide is cladded to the bottom and to the top by a 3-µm thick SiO2 layer. A top view schematic and

an SEM picture of the investigated device are shown in Fig. 5.1(a) and Fig. 5.1(b), respectively. The microresonator waveguide width *H* is set to 1.6 µm, while the ring radius *R* is 22.85 µm, corresponding to a free spectral range (FSR) of ~1 THz. The bus waveguide width is 0.1µm. Different coupling strength can be achieved by varying the gap G between the bus and the ring waveguides. Critical coupling is experimentally achieved for G = 750 nm. A typical transmission spectrum is shown in Fig. 5.1(c) and Fig. 5.1(d). The measured 3-dB frequency bandwidth of the resonance around the critical coupling point is MHz, yielding a loaded Q factor of $\sim 1.4 \cdot 10^6$. A resonance measured for TM fundamental mode is shown in Fig. 5.1(e), with $Q \cong 2.59 \times 10^5$.

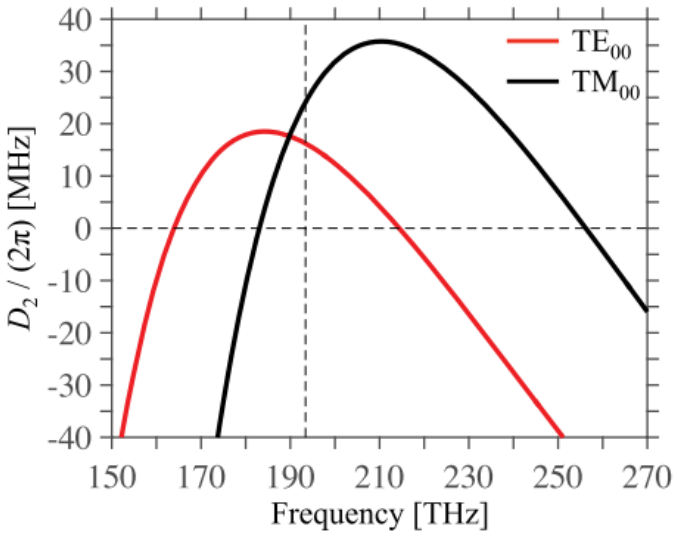

Figure. 5.2: Simulated spectra of the second-order dispersion $D_2/(2\pi)$ for the fundamental TE (in red) and TM (in black) modes. The vertical dashed line indicates the 1.55-µm wavelength.

In order to realize broadband (octave-spanning) frequency comb generation, dispersion engineering of the waveguide's group velocity dispersion (GVD) is necessary [7]. By tailoring the width and the height of the waveguide, the normal material dispersion of Si_3N_4 at

1.55-μm telecom wavelength can be compensated by an anomalous waveguide dispersion. Fig. 5.2 shows the simulated dispersion profile featuring anomalous dispersion (D_2>0) around the pump frequency of 193 THz (corresponding to 1550 nm wavelength).

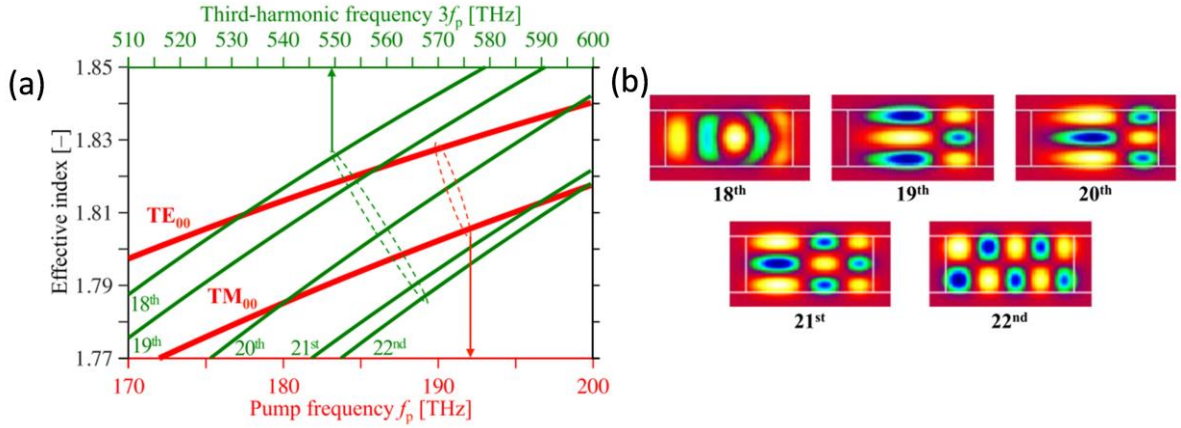

Figure. 5.3: (a) Simulated spectra of the effective index for the fundamental TE and TM modes of the ring microresonator (in red) at the pump frequency f_p, and for higher-order modes (18th to 22nd orders, in green) at the third-harmonic frequency. (b) Cross section of the intensity distributions in the ring resonator simulated for the relevant higher-order modes at 576.5 THz (or 520 nm).

The dispersion is optimized to yield broadband combs around 1550 nm wavelength. In the meanwhile, we also designed this resonator waveguide to simultaneously phase-match the IR comb and its modes at frequency tripled spectrum to form combs at green light. Efficient THG can be achieved if the wavenumber $k = 2\pi nf / c$ of the fundamental waveguide mode at the IR frequency f_P is 3 times smaller than the wavenumber of a higher-order mode at the green frequency $3\ f_P$. The effective indices n and the intensity distributions for the fundamental TE and TM modes at the pump frequency, and for higher-order modes at the TH frequency are simulated with FIMMWAVE. The phase-matching conditions are shown in

Fig. 5.3 (a). It can be seen that at some frequencies, the effective index of several higher-order TH modes matches the effective index of the fundamental TE or TM mode. Specifically, there are three matching conditions between the 18th, 19th, 20th third harmonic (TH) mode and the fundamental TE mode (for $f_P \cong$ 177.4 THz, 186.2 THz and 198.5 THz), as well as three other matching conditions between the 20th, 21st, and 22nd, TH modes and fundamental TM mode (for $f_P \cong$ 180.1 THz, 196.6 THz and 199.2 THz). Each matching condition contributes to broadening the spectral range in the frequency-converted comb lines at green.

In experiment, a tunable single-frequency CW laser source (Agilent81642A, with a typical linewidth of ~100 kHz and a tuning range of 1510-1640 nm) is used as the seed laser to pump the ring microresonator. An erbium-doped fiber amplifier (EDFA, IPG EAR-2K-C) with a maximum output power of ~ 33 dBm ($\cong$ 2W) was used to boost the pump power. The light was coupled in and out of the device through tapered lensed fibers with an anti-reflective coating. A polarization controller is positioned before the input lensed fiber to selectively couple into the fundamental TE or TM mode of the waveguide. The signal intensities in the IR and in the green spectral region are monitored respectively by a high-speed 1550-nm power sensor and by a silicon-PIN photo-detector for visible light. Two optical spectrum analyzers (Yokogawa AQ6375 for 1200-2400 nm and AQ6373B for 350-1200 nm) are used to measure their respective spectra. Using the thermal-locking technique [8], IR Kerr comb can be obtained when the pump frequency is tuned into the resonance, with an input power larger than the threshold for parametric oscillations. As the laser scans into the resonance, the buildup of power inside the ring microresonator can lead (via degenerate or non-degenerate FWM) to the generation of broadband Kerr frequency combs

[9]. For this excitation pathway, it is noted that the comb is in the high-noise regime [10]. While not attempted or observed in this work, low-noise comb states can be attained by techniques, such as δ -Δ matching or parametric seeding, or via the soliton regime.

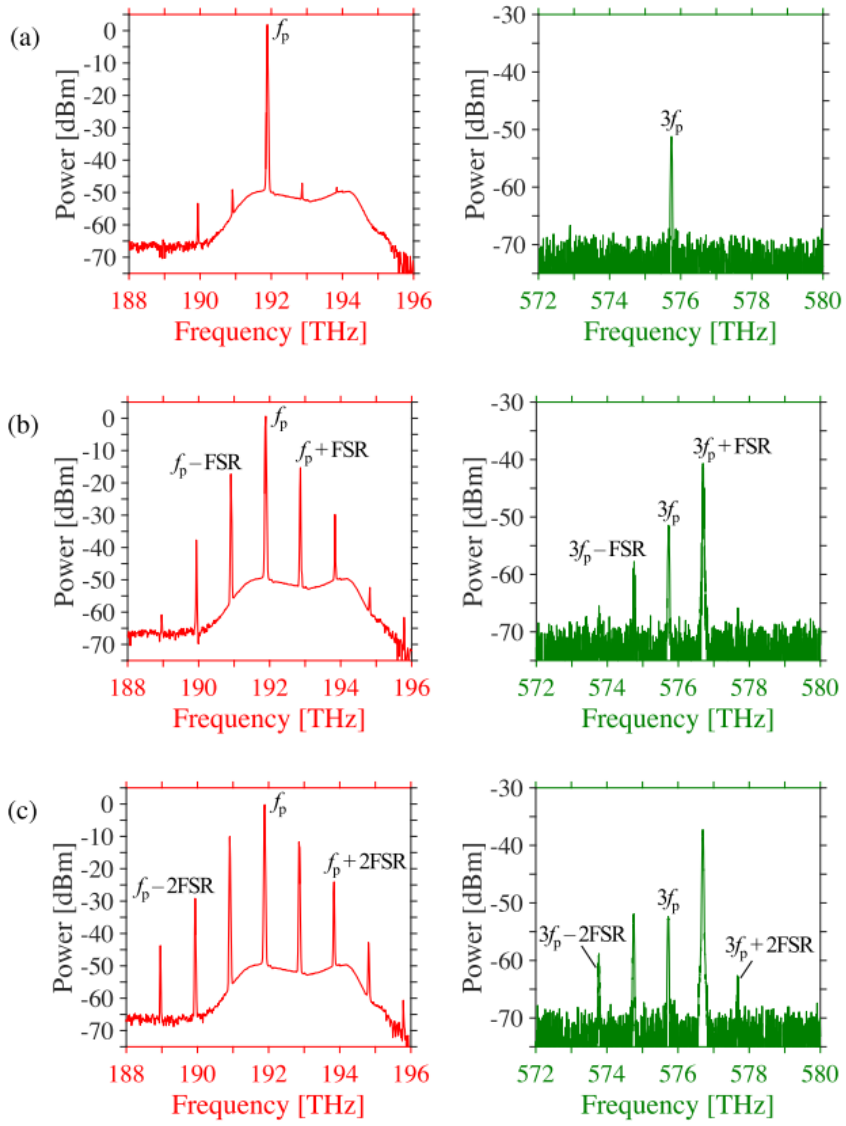

Figure. 5.4: Generation process of the IR Kerr comb (left column) and the simultaneously emitted GLC (right column), by gradually tuning the TE-polarized IR pump to the resonance near f_p ~= 191.9 THz.

The threshold value of on-chip input power for THG generation (only one frequency line in green) is estimated to as low as ~16 dBm, and the threshold for green light comb (GLC) generation (with several green lines) is ~20 dBm. The observed formation process for the IR comb and the simultaneously converted GLC is detailed in Fig. 4. The data from Fig. 5.4(a) suggest that the first (central) emitted line of the GLC is formed by the THG process, where the interaction of three photons with frequency f_P from the IR pump laser results in the creation of a photon with the tripled frequency $3\,f_P$. Tuning the pump frequency gradually into resonance, both the number and the intensity of the IR comb lines increase as the cavity circulating power strengthens.

It can be seen from Fig. 5.4(b) and Fig. 5.4(c) that as the IR comb lines strengthen, more green comb lines are simultaneously generated. The FSR of green comb is the same with that of IR comb indicates that their lines are formed by both THG as well as third-order SFG processes. In this ideal case, the newly generated components will thus be equidistant in frequency domain with respect to the IR pump. In addition, the parametric processes can be efficiently enhanced only when these frequencies coincide with the modes of the ring microresonator [11]. The phase-matching condition would thus be automatically satisfied once it is ensured for both the FWM of the IR comb and the THG of the central line of the green light comb, and it would successively lead to a cascaded frequency-tripling process through the third-order SFG.

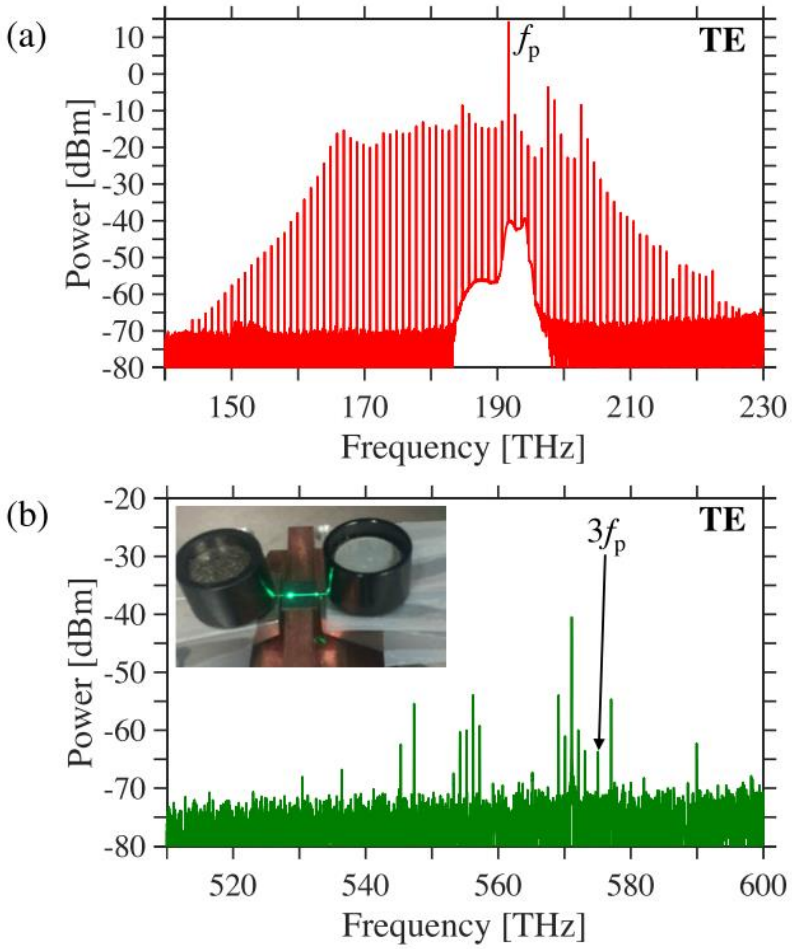

Figure. 5.5: (a) IR Kerr comb generated with a TE pump and (b) the corresponding GLC with 18 spectral lines. In (b), the inset shows a photograph of the probed device. The pump frequency f_p = 191.7 THz and both IR and green combs have FSR ~= 992.6 GHz.

At the maximum output power of the EDFA (~ 33 dBm), broadband albeit high-noise IR combs can be established. By carefully positioning the input fiber and optimizing the polarization, the combs are observed with different features with the fundamental (quasi-)TE or (quasi-)TM mode pumping. For the TE situation, as shown in Fig. 5.5, the observed IR comb exhibits a uniform envelope and covers 2/3 of an octave (144-226 THz or 1327-2082 nm). The corresponding green comb consists of 18 lines that spread from 530 THz to 590

THz (or 508-566 nm). Ideally the green comb lines would be continuous and uniform; however, some comb lines are missing in the spectrum shown in Fig. 5.5(b), which can be attributed to a resonance mismatch [12]. Besides, the simulations of Fig. 5.3 showed that phase-matching of a TH mode can be realized with different IR comb lines. As a result, several separated spectral clusters are observed in Fig. 5.5(b) with distinct strong peaks. The first and second strongest GLC lines are located at 571.1 THz and 577.0 THz, respectively. However, the pump frequency if f_P = 191.7 THz, corresponding to the THG frequency of 3 f_P =575.1 THz. In THG, all the 3 input photons are provided from the same IR comb line. When computing the efficiency bandwidth, the frequency of these 3 photons thus varies simultaneously. In contrast, for third-order SFG, the frequency of one or two input photons is fixed at the pump of the IR comb, and the frequencies of photons from other comb lines vary. Therefore, the phase-matching condition for third-order SFG is less dependent on dispersion, which is similar to the effects reported in Ref. [12]. This implies that the phase-matching requirement for the third-order SFG is less stringent than that for THG, which enables the conversion of a broader bandwidth of IR comb lines into the wider visible range. This effect is responsible for the broad bandwidth of the GLC and the nearly continuous comb lines observed experimentally.

From the simulations of Fig. 5.3, the phase-matched window with the fundamental TM mode has a better overlap with the effective working bandwidth of the employed EDFA (191-196 THz, or 1530-1570 nm) compared with that of the TE mode. This can explain why much stronger GLC is achieved in the experiments with the fundamental TM mode pumping, as shown in Fig. 5.6. The generated IR comb extends over a narrower range (158-218 THz, or 1375-1897 nm) compared to the case of TE pumping. Yet, 30 lines are detected for the

GLC, with frequencies ranging from 517 THz to 597 THz (or 502-580 nm). In the central part of the THG frequency, 17 continuous comb lines are observed, as seen in Fig. 5.6(b). Both IR comb and GLC have FSR ≅ 977.2 GHz.

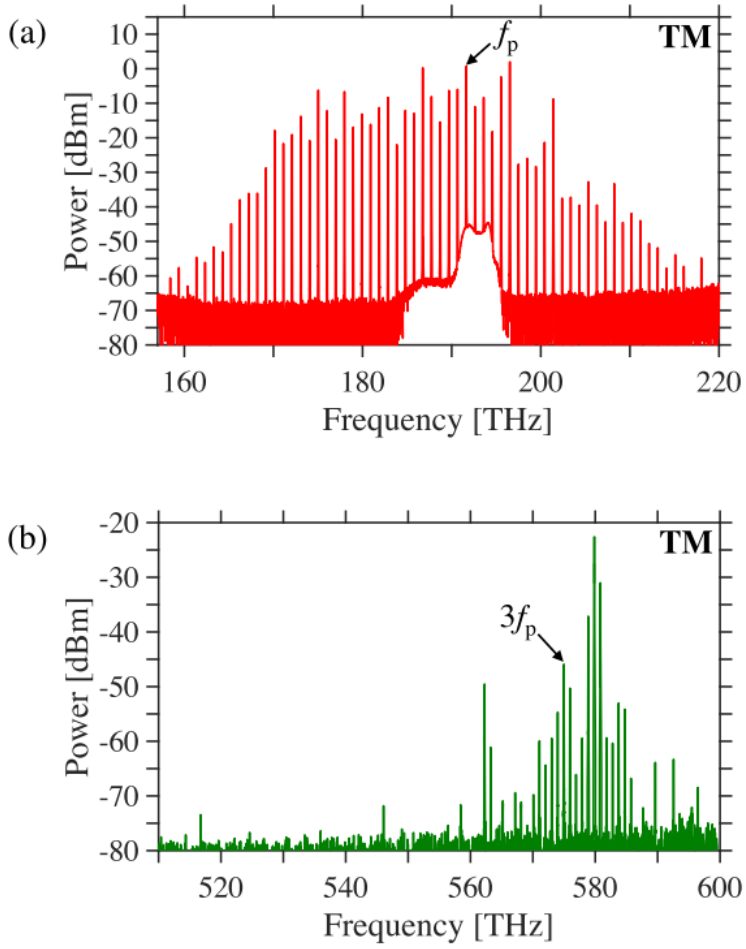

Figure. 5.6: (a) IR Kerr comb generated with a TM pump and (b) the corresponding GLC with 30 spectral lines. In (b), the inset shows a photograph of the probed device.

With TE pumping, the output power of the GLC measured with the photo-detector is about −35.2 dBm (or 0.3 μW). Losses due to coupling and propagation of the green light are estimated to 10.7 dB. Therefore, the power of the GLC in the output bus waveguide is about −24.5 dBm (or 3.5 μW). With TM pumping, the GLC power measured with the photo-

detector is about −19.6 dBm (or 11 μW), and its power in the output bus waveguide is estimated to −9.1 dBm (or 123 μW). The pump power in the input bus waveguide is estimated to 25 dBm (or 316 mW), thus yielding an on-chip conversion efficiency of −34 dB (or $4 \cdot 10^{-4}$). The net efficiency is −53 dBm (or $6 \cdot 10^{-6}$), thus more than 3 orders of magnitude larger than recently reported with AlN ring microresonators [13].

5.2.3 Supercontinuum generation

Supercontinuum generation (SCG) is a $\chi^{(3)}$ nonlinear process where laser pulses of relatively narrow bandwidth can be converted into a continuum with large spectral span [14]. SCG has numerous applications, including self-referencing frequency combs [15], microscopy [16], spectroscopy [17], and tomography [18]. SCG is traditionally accomplished using bulk crystals or nonlinear fiber, but recently, photonic waveguides (on-chip waveguides produced using nanofabrication techniques) have proven themselves as a versatile platform for SCG, offering small size, high nonlinearity, and increased control over the generated spectrum [19]. The spectral shape and efficiency of SCG are determined by the input pulse parameters, the nonlinearity of the material, and the refractive index of the waveguide, which determines the phase-matching conditions.

On our Si_3N_4 platform, besides the commonly used SCG, we developed a new approach which applied QPM to enhance the intensity of the supercontinuum in specific spectral regions determined by the modulation period.

It is well known that in the regime of anomalous GVD, the nonlinearity of the material can balance GVD and allow pulses to propagate while remaining temporally short. Such solitons can propagate indefinitely, unless perturbed [14]. However, in the presence of higher-order dispersion, some wavelengths of quasi-continuous-wave light may propagate at

the same phase velocity as the soliton. Light at these wavelengths can "leak out" of the soliton in the form of dispersive wave (DW) radiation, which is also referred to as "resonant radiation" [20] or "optical Cherenkov radiation" [21]

Periodic modulations of the waveguide change the effective area of the mode, modulating both the effective nonlinearity and the GVD, enabling QPM-DW generation. The contribution of a modulation (with period Λ) to the wave vector phase mismatch will be $k_{QPM} = 2\pi q / \Lambda$, where q is the QPM order and can be any positive or negative integer. Thus, the phase-matching condition for dispersive wave generation can be modified with that additional wavevector.

In addition to satisfying the QPM condition, three additional requirements must be met for efficient DW generation. (i) The QPM order q must be a strong Fourier component of the periodic modulation. (ii) There must be overlap between the spatial mode of the soliton and the mode of the DW. (iii) The DW must be located in a spectral region where the soliton has significant intensity, a requirement that applies regardless of the phase-matching method.

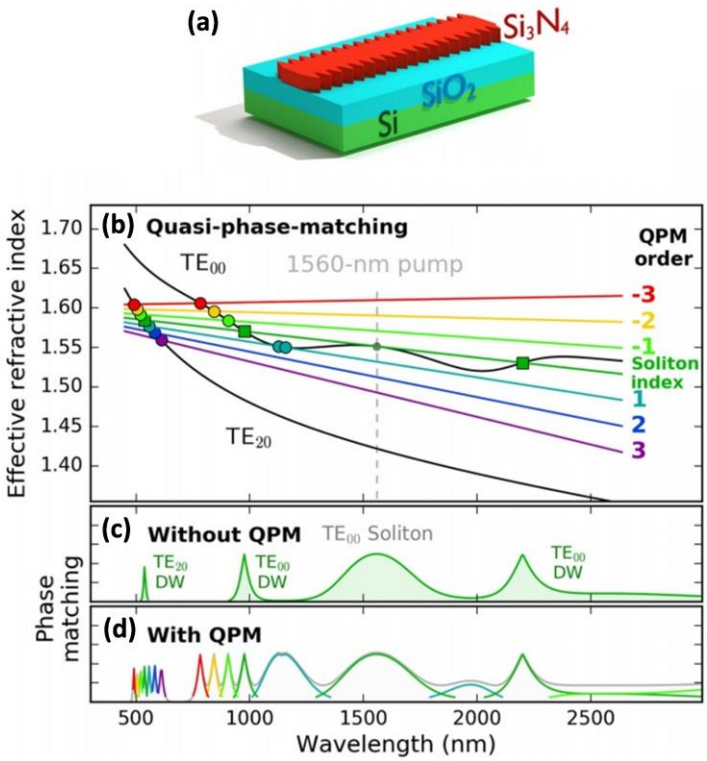

Figure. 5.7: (a) Quasi-phase-matching of supercontinuum generation in on-chip photonic waveguides can be achieved via waveguide-width modulation; (b) When the effective index of the soliton in the TE00 mode ("soliton index") intersects the effective index of a waveguide mode (black curves), phase matching to dispersive waves is achieved (green squares) and a spectrum with several peaks (c) is generated. The periodic modulation of the waveguide can enable numerous QPM orders, both positive and negative, which can allow QPMDW generation to the fundamental mode and to higher-order modes (circles), producing a spectrum with many peaks (d). Note that the index curvature is exaggerated to better show phase matching.

Here we explored a width modulated waveguide structure for QPM-DW. The width-modulated Si3N4 waveguides [Fig. 5.7(a)] are fully SiO2 clad and have a thickness of 750 nm, a maximum width of 1500 nm, and an overall length of 15 mm. Over a 6-mm central region, the width is modulated sinusoidally from 1250 to 1500 nm. Multiple waveguides are

fabricated on the same silicon chip, and each waveguide has a different width modulation period, which ranges from 5.5 to 6.5 μm.

We generate supercontinuum by coupling ~80 fs pulses of 1560-nm light from a compact 100 MHz Er-fiber frequency comb. The power is adjusted using a computer-controlled rotation mount containing a half-wave plate, which is placed before a polarizer. The polarization is set to horizontal (i.e., parallel to the Si-wafer surface and along the width dimension of the rectangular Si_3N_4 waveguide), which excites the lowest order quasi-transverse-electric (TE_{00}) mode of the waveguide. We record the spectrum at many increments of the input power using an automated system that interfaces with both the rotation mount and the optical spectrum analyzers. The waveguide modes (and their effective indices) are calculated using a vector finite difference mode solver, using published refractive indices for Si_3N_4 and SiO_2. For the width-modulated waveguides, a narrow peak appears in the spectrum in the 630-nm region [Fig. 5.8(a)], and the location of this peak changes with the width modulation period [Fig. 5.8(c)]. By calculating the refractive index of the higher order modes of the waveguide, and including the QPM effect from the periodic width modulation [Fig. 5.8(b)], we find the QPM-DW generation to the TE_{20} mode is a likely mechanism for the appearance of this peak [Fig. 5.8(c)]. The preference for QPM-DW generation to the TE20 mode is a result of the modal overlap between the TE_{20} mode at the DW wavelength (~630 nm) and the TE_{00} mode at the soliton wavelength (1560 nm). In general, modes that are symmetric in both the vertical and horizontal directions (such as the TE_{20} mode) will have much higher overlap with the fundamental mode than antisymmetric modes, and are, consequently, the most commonly used for model phase-matching schemes.

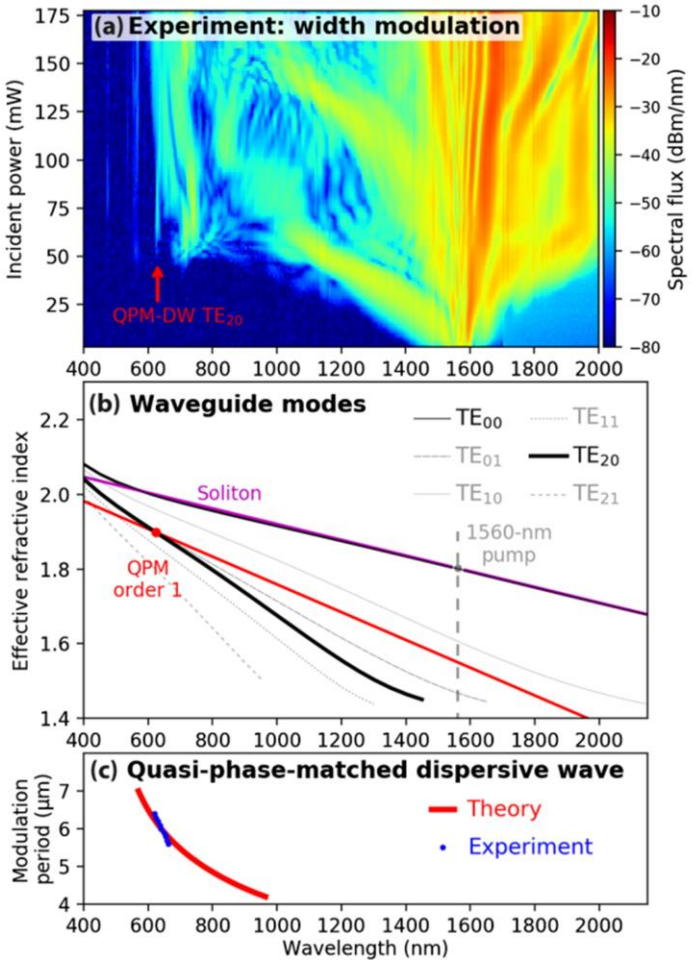

Figure. 5.8: (a) The spectrum of supercontinuum generation from a width-modulated waveguide as a function of input power. The arrow indicates the QPM DW to the TE_{20} mode. (b) The effective refractive index of various modes of the waveguide as a function of wavelength. When the index of the soliton including a first order grating effect from the 6.2-μm width-modulation (red line) crosses the TE_{20} mode, a QPM DW is generated. (c) The calculated spectral location of the TE_{20} QPM DW as a function of the width-modulation period is in agreement with experimental results. The slight difference in slope may arise from irregularities in the dimensions of the waveguides.

This is the first demonstration of QPM to produce DWs in on-chip waveguides. Previously designers of waveguide-SCG sources work in a limited parameter space: selecting

materials and selecting the dimensions of the waveguide cross section. QPM opens a new dimension in the design space for photonic waveguides, one that is largely orthogonal to the other design dimensions. This orthogonality exists both in real space, since the QPM modulations exist in the light-propagation direction, but also in the waveguide-design space, as it provides a simple vertical shift of the phase-matching conditions with no bending of the index curve [Fig. 5.7(b)]. Consequently, it allows the spectral location of DWs to be modified with minimal effect on the GVD at the pump wavelength, which enables the soliton propagation conditions to be controlled separately from the DW phase-matching conditions. For example, using QPM, DWs could be produced even for purely anomalous GVD, greatly relaxing the requirements for material dispersion and waveguide cross section. Importantly, since the GVD at the pump is known to affect the noise properties of the SCG process, the ability to manipulate the locations of the DWs separately from the GVD could enable SCG sources that are simultaneously broadband and low noise. In addition, since similar phase-matching conditions apply to SCG with picosecond pulses or continuous-wave lasers, QPM of the SCG process is likely not restricted to the regime of femtosecond pulses.

5.3 Si_3N_4-$LiNbO_3$ platform

In Chapter 3 we discussed the nonlinear platform based on the SiN- $LiNbO_3$ hybrid structures. An alternative approach for LN-SiN low-loss waveguides is to bond LN film onto SiN [22]. The Damascene process provides high quality stoichiometric Si_3N_4 layer, which can also be thicker for improved index matching for low-loss mode transitions between the Si_3N_4 and LN-Si_3N_4 waveguides. Such platform provides strong $\chi^{(2)}$ and $\chi^{(3)}$ coefficients ($\gamma \sim 1.4 W^{-1}km^{-1}$ for this work), high confinement factors, low propagation and coupling losses for waveguides.

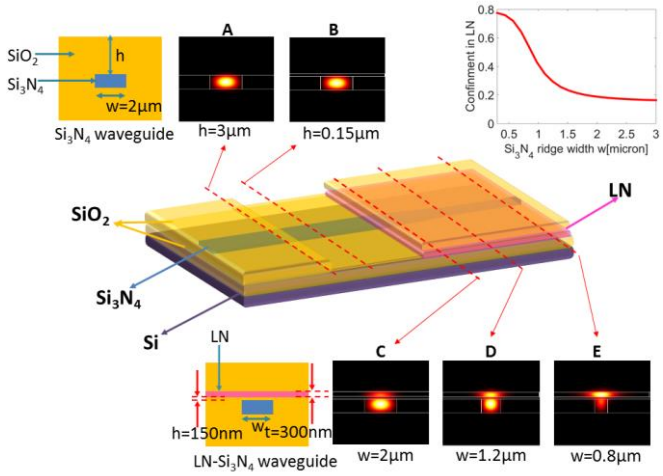

Figure. 5.9: Schematic structure of tapered mode converter connecting the two types of waveguides. The top and bottom areas show schematics of the waveguide cross-sections and simulated profiles of the fundamental TE modes at 1540 nm. Inset is the simulated confinement factor in the LN layer for LN-Si_3N_4 hybrid waveguides calculated as a function of the Si_3N_4 rib width.

The heterogeneous platform presented here consists of two types of waveguides, both illustrated in Fig. 5.9. The fully cladded Si_3N_4 waveguide for $\chi^{(3)}$ nonlinear interaction is 850 nm high and ~2 μm wide to achieve anomalous group velocity dispersion at C band. Another type is the LN- Si_3N_4 waveguide for $\chi^{(2)}$ applications, consisting of a 300-nm thick LN layer separated from a Si_3N_4 core by a 150-nm thin SiO_2 spacer. Such geometry matches the indices of these two layers.

The schematic cross-section of the LN-Si_3N_4 waveguide is shown in Fig. 5.9. Because the Si_3N_4 waveguide and the LN layer have nearly the same index, confinement factors in these two cores are sensitive to Si_3N_4 ridge width, shown in the top right inset of Fig. 5.9. The ridge width is designed to be 0.8 μm, corresponding to a confinement factor of ~0.6 in LN core.

A mode converter is designed to enable low-loss mode transition between the two types of waveguides and a schematic is shown in the center of Fig. 5.9. The Si_3N_4 input waveguide is 2-µm wide with 3-µm SiO_2 top cladding (A), and input light then passes through an abrupt change of the upper cladding to 150 nm (B). After entering the bonded area with a LN film on top, the width of the Si_3N_4 ridge decreases linearly from 2.0 µm (C) to 0.8 µm (E), adiabatically transitioning the majority of the mode upwards into the LN layer. The evolution of simulated mode distributions (performed with FIMMWAVE) for different waveguide geometries is shown in Fig. 5.9, at 1540 nm wavelength. According to simulations, the loss per LN facet (from A to E) is 0.9 dB, which is due to the abrupt index change between the Si_3N_4 and heterogeneous waveguides (B to C). Here a 150-nm thick SiO_2 spacer is introduced to reduce this index change. Further increasing the spacer thickness to 300 nm is expected to reduce the loss to 0.4 dB per facet, but this will also increase the optical mode size. This trade-off can be adjusted depending on the application.

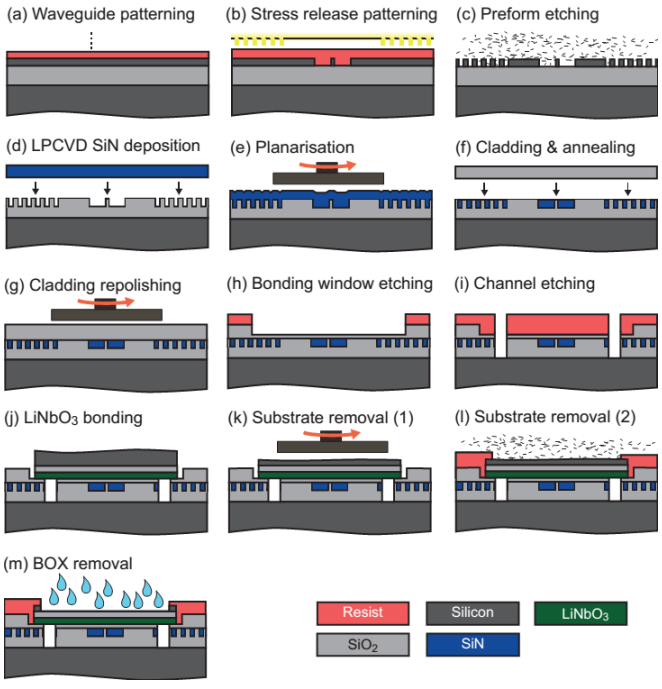

Figure. 5.10: Fabrication procedure for the LN-Si_3N_4 platform.

The device fabrication process is schematized in Fig. 5.10. The photonic Damascene process [3] is used to fabricate the Si_3N_4 waveguide devices on a 100-mm substrate and provide local openings with planar surface for LN bonding. At first, an 850-nm thick layer of nearly stoichiometric Si_3N_4 is deposited by low-pressure chemical vapor deposition (LPCVD) on a pre-structured substrate. The substrate not only includes the waveguide pattern but also a dense stress-release pattern, to avoid the formation of cracks during the Si_3N_4 deposition that cause high scattering loss. Chemical-mechanical polishing is used to remove excess Si_3N_4 after deposition, creating a planar top surface across the wafer. A 3-µm thick SiO_2 layer is then deposited on Si_3N_4 as the top cladding. A scanning electron micrograph (SEM) of the cross-section of this Si_3N_4 waveguide is shown in Fig. 5.11(a). In order to reduce the surface roughness in preparation for bonding, the deposited SiO_2 cladding layer is re-polished. Fig. 5.11(b) shows the roughness measurement of the as-deposited low temperature SiO_2 film as well as after the re-polishing step. The bonding area is then opened by dry etch, leaving a thin SiO_2 layer as spacer. Additionally, vertical channels are patterned in these areas to release the gas during bonding. After that, a chip (purchased from NANOLN) consisting of a 300-nm thick *x*-cut LN film on a 2-µm thick buried SiO_2 on a Si substrate is bonded onto the opened area after surface plasma activation. The bonded sample is then annealed to enhance the bonding strength. The integrated chip is shown in Fig. 5.11(c). Finally, mechanical polishing, dry etch and BHF have been used to remove the Si substrate and buried oxide (BOX) layer, leaving only the LN film on chip in the open area, as shown in Fig. 5.11(d).

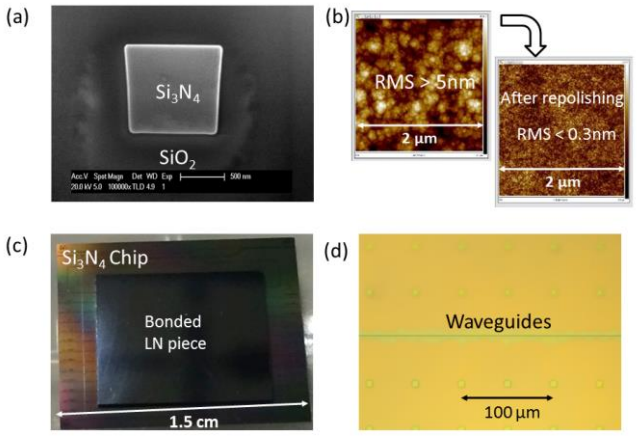

Figure. 5.11: (a) SEM cross-section of the Si_3N_4 waveguide. (b) Roughness testing results after SiO_2 deposition and repolishing. (c) Top-view of integrated LN- Si_3N_4 chip. (d) Bonded area after substrate and BOX layer removal.

For characterizing the devices, a tunable single-frequency CW laser (Keysight 81642A) with spectral range of 1.51-1.64 µm and linewidth ~0.1 MHz is used as the light source. Collimated light passes through a polarizer (Thorlabs PCB-2.5-1550) aligned to efficiently excite the TE-polarized mode of the waveguide. A focusing lens (Thorlabs C230TM-C) is used for the input coupling and a lensed fiber couples the light out of the device. An optical power sensor (Keysight 81634B) is used to monitor the transmitted power.

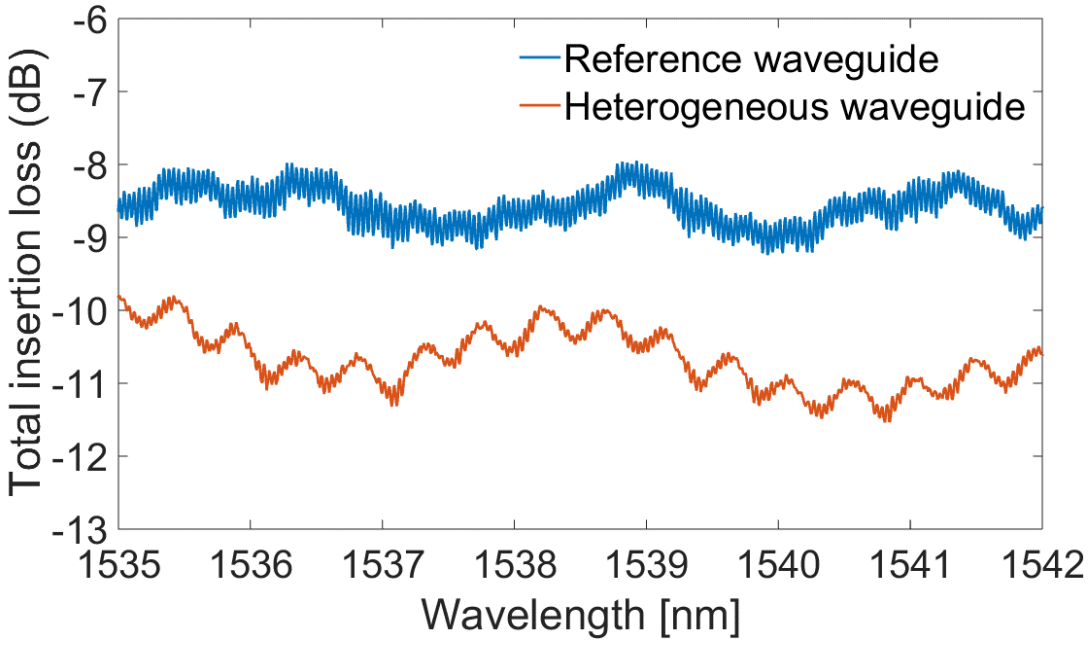

Figure. 5.12: Spectra of total insertion loss for the reference waveguide (blue) and heterogeneous waveguide (red).

The testing structure used here is a 1-cm long heterogeneous waveguide, with two tapers connecting to the Si_3N_4 waveguides. TE polarized light is coupled in and out through the Si_3N_4 waveguides. Compared to the reference Si_3N_4 waveguide with the same length, the insertion loss (fiber to fiber) of the heterogeneous waveguide is ~2 dB larger around C band, shown in Fig. 5.12. There are small ripples for heterogeneous waveguide spectrum, which may be due to the taper reflections.

Here, the insertion loss for the reference and the test structures are denoted α_{ref} and α_{test}, respectively, and their propagation loss by α_{SiN} and α_{heter}, respectively. The following equations define the total insertion loss:

$$\alpha_{ref} = \alpha_{SiN} + \alpha_c \tag{5.3.1}$$

$$\alpha_{test} = \alpha_{heter} + 2\alpha_{AB} + 2\alpha_{BC} + \alpha_c, \quad (5.3.2)$$

Where α_{AB} and α_{BC} are the losses at the A-B and B-C boundaries in Fig. 5.9 and α_c is the coupling loss in and out of the chip.

The propagation loss for the heterogeneous waveguide is obtained by subtracting Eq. (5.3.2) from Eq. (5.3.1):

$$\alpha_{heter} = \alpha_{SiN} - 2\alpha_{AB} - 2\alpha_{BC} - (\alpha_{ref} - \alpha_{test}). \quad (5.3.3)$$

The value of $\alpha_{ref} - \alpha_{test}$ is obtained from the testing results of Fig. 5.12 and α_{SiN} by the pre-mentioned measurements of resonators (0.11 dB/cm*1 cm), assuming that $\alpha_{AB} + \alpha_{BC} \cong 0.9$ dB as supported by simulations. The calculated propagation loss for the heterogeneous waveguide is (0.2 ± 0.4) dB/cm. Because the coupling loss varies among waveguides, this method may have an extra uncertainty. Here the Fabry-Perot based method is also used and a loss of (0.3 ± 0.6) dB/cm is extracted, which is in good agreement. Such a low propagation loss is comparable with the loss of a bulk LN waveguide. Considering that the waveguide area is more than one order of magnitude smaller than that of bulk waveguides, these waveguides can improve the efficiency for nonlinear applications by the same proportion without sacrificing additional propagation loss.

5.4 Si_3N_4-GaAs platform

Similar as the integration approach applied to $LiNbO_3$ in last section, nonlinear (Al)GaAs waveguide can also be heterogeneously bonded onto the Si_3N_4 chip to form a CMOS compatible nonlinear platform. The advantage of it is that (Al)GaAs offers the high nonlinear

coefficients in both $\chi^{(2)}$ and $\chi^{(3)}$, which leads to more flexibility in high performance device demonstration and system design. Furthermore, such integration paves the ways for bridging active components based on III-V with high quality Si_3N_4 nonlinear devices in the future.

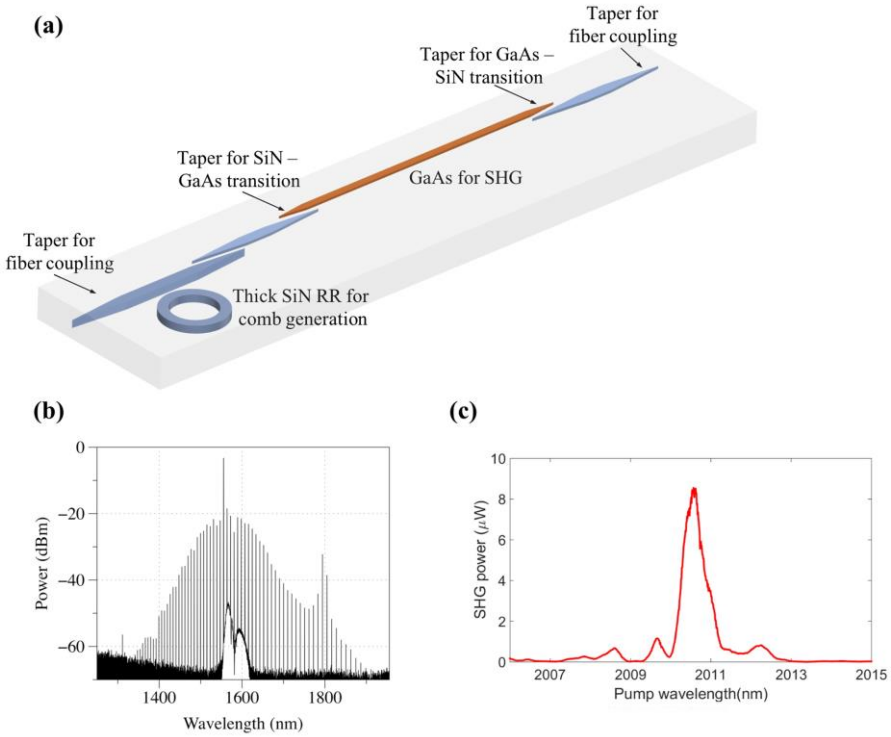

Figure. 5.13: (a) illustrates the device design of the integration of a GaAs waveguides for frequency doubling onto SiN waveguides for the optical frequency comb generation and the transitioning between the layers. (b) and (c) present the results for the generated frequency comb of the SiN ring resonator and the GaAs frequency doubler on the same chip, respectively.

The schematic drawing of one kind of structure is shown in Fig. 5.13(a). The chip is composed of three different layered structures. The bottom one is the thick Si_3N_4 waveguide, whose thickness is around 800 nm, used for frequency comb generation. The middle layer is 400 nm thick Si_3N_4 interposer circuits, whose functionality is to provide efficient coupling to

the III-V waveguides, as well as other off-chip components. The top III-V layer we used in this work is 150 nm GaAs, same with the thickness previously we used for SHG demonstrations.

The fabrication is similar to which is discussed in last section for Si_3N_4-$LiNbO_3$ chips. One difference is that there are two layers of Si_3N_4 processes instead of one. In the meantime, after substrate removal, the nonlinear layer of GaAs is etched to form the waveguides.

Linear tapers are used to bridge waveguides in different layers, whose coupling losses are below 1 dB per taper, which enable the efficient mode transitions. The measurements of nonlinear devices on this platform are shown in Fig. 5.13(b) and (c). The comb generation and the frequency coupler were characterized separately to test the performance of the heterogeneously integrated device. Figure 4(b) shows the optical frequency comb generated by Si_3N_4 resonator, whose waveguide is 1.5 micron wide and 800 nm tall, when pump power inside bus waveguide is around 13 dBm at a wavelength of around 1.55 μm. It can be seen that the frequency comb that was generated does not cover a full octave as it is required in order to achieve the desired device functionality with on-chip frequency doubling. This can be explain by: (i) The thick SiN waveguides thickness of the sample may be off, which impacts the dispersion and results in the dispersive waves being too close to the pump wavelength and not at a wavelength of 1 μm and 2 μm, as desired. (ii) The highest pump power at 1.55 μm wavelength that could be used to excite the ring resonators was limited as we observed that pump powers above 13 dBm could destroy the GaAs waveguides. We suspect that the two photon absorption (TPA) in the GaAs (especially at the narrow waveguide tapers) causes at these high intensities a significant heating of the GaAs, resulting in the waveguides getting damaged. In the future, the use of AlGaAs can relieve this problem.

On the same waveguide structure we also characterized the GaAs frequency doubler, whose waveguide width is 1.5 μm wide and height is 150 nm, similar as the devices we discussed in Chapter 4. By exciting it with a tunable 2 μm wavelength laser light and measuring the SHG as well as the pump power, we extracted the conversion efficiency of the frequency doubler, which is presented in Fig 5.13(c). The conversion efficiency (~10000 % $W^{-1}cm^{-2}$) of this frequency doubler is slightly lower to the one that we characterized compared to the results in Chapter 4, which could be due to some slight non-uniformities of the GaAs waveguide cross-section [23].

5.5 Summary and outlook

The CMOS compatible nonlinear platforms, at this point, are still at early stages and very few attempts have been made in this field. However, due to the advantage of combining frontier nonlinear photonic research with large scale, low cost production in industry, it poses a very attractive solution for the realization of fully integrated nonlinear systems o-chip, such as optical frequency synthesizer, optical atomic clock and the dual comb spectroscopy on chip.

However, even though this approach is very promising, there are still many challenges. One difficulty is that the fabrication of high quality Si_3N_4 requires extra procedures to release the high stress caused the thick film as well as to obtain low waveguide loss. One way to address that is to only use interposer Si_3N_4 which is relative thin, and integrating nonlinear materials which can satisfy the requirements for both $\chi^{(2)}$ and $\chi^{(3)}$ applications, like (Al)GaAs. Another problem is that, in order to interface the nonlinear waveguide with Si_3N_4 circuits, the two layers need to be set very closely, which requires a careful control in fabrication along

with the top cladding planarization. Moreover, the light source is still hard to integrate on Si_3N_4, which may require extra packaging efforts.

Reference

[1] T. Komljenovic *et al.*, "Heterogeneous Silicon Photonic Integrated Circuits," *J. Light. Technol.*, vol. 34, no. 1, pp. 1–1, 2015.

[2] A. D. Bristow, N. Rotenberg, and H. M. van Driel, "Two-photon absorption and Kerr coefficients of silicon for 850–2200nm," *Appl. Phys. Lett.*, vol. 90, no. 19, p. 191104, May 2007.

[3] M. H. P. Pfeiffer, J. Liu, A. S. Raja, T. Morais, B. Ghadiani, and T. J. Kippenberg, "Ultra-smooth silicon nitride waveguides based on the Damascene reflow process: fabrication and loss origins," *Optica*, vol. 5, no. 7, p. 884, Jul. 2018.

[4] D. T. Spencer *et al.*, "An optical-frequency synthesizer using integrated photonics," *Nature*, vol. 557, no. 7703, pp. 81–85, 2018.

[5] D. J. Moss, R. Morandotti, A. L. Gaeta, and M. Lipson, "New CMOS-compatible platforms based on silicon nitride and Hydex for nonlinear optics," *Nat. Photonics*, vol. 7, no. 8, pp. 597–607, Aug. 2013.

[6] M. H. P. Pfeiffer *et al.*, "Octave-spanning dissipative Kerr soliton frequency combs in Si_3N_4 microresonators," *Optica*, vol. 4, no. 7, p. 684, Jul. 2017.

[7] A. L. Gaeta, M. Lipson, and T. J. Kippenberg, "Photonic-chip-based frequency combs," *Nat. Photonics*, vol. 13, no. 3, pp. 158–169, Mar. 2019.

[8] T. Carmon, L. Yang, and K. J. Vahala, "Dynamical thermal behavior and thermal self-stability of microcavities," *Opt. Express*, vol. 12, no. 20, p. 4742, Oct. 2004.

[9] T. Herr, M. L. Gorodetsky, and T. J. Kippenberg, "Dissipative Kerr solitons in optical

microresonators."

[10] T. Herr *et al.*, "Universal formation dynamics and noise of Kerr-frequency combs in microresonators," *Nat. Photonics*, vol. 6, no. 7, pp. 480–487, Jul. 2012.

[11] T. J. Kippenberg, R. Holzwarth, and S. A. Diddams, "Microresonator-based optical frequency combs.," *Science*, vol. 332, no. 6029, pp. 555–9, Apr. 2011.

[12] S. Miller, K. Luke, Y. Okawachi, J. Cardenas, A. L. Gaeta, and M. Lipson, "On-chip frequency comb generation at visible wavelengths via simultaneous second- and third-order optical nonlinearities," *Opt. Express*, vol. 22, no. 22, p. 26517, Nov. 2014.

[13] H. Jung, R. Stoll, X. Guo, D. Fischer, and H. X. Tang, "Green, red, and IR frequency comb line generation from single IR pump in AlN microring resonator," *Optica*, vol. 1, no. 6, p. 396, Dec. 2014.

[14] J. M. Dudley, G. Genty, and S. Coen, "Supercontinuum generation in photonic crystal fiber," *Rev. Mod. Phys.*, vol. 78, no. 4, pp. 1135–1184, Oct. 2006.

[15] R. Holzwarth, T. Udem, T. W. Hänsch, J. C. Knight, W. J. Wadsworth, and P. S. J. Russell, "Optical Frequency Synthesizer for Precision Spectroscopy," *Phys. Rev. Lett.*, vol. 85, no. 11, pp. 2264–2267, Sep. 2000.

[16] T. Betz *et al.*, "Excitation beyond the monochromatic laser limit: simultaneous 3-D confocal and multiphoton microscopy with a tapered fiber as white-light laser source," *J. Biomed. Opt.*, vol. 10, no. 5, p. 054009, 2005.

[17] I. Coddington, N. Newbury, and W. Swann, "Dual-comb spectroscopy," *Optica*, vol. 3, no. 4, p. 414, Apr. 2016.

[18] S. Moon and D. Y. Kim, "Ultra-high-speed optical coherence tomography with a stretched pulse supercontinuum source," *Opt. Express*, vol. 14, no. 24, p. 11575, Nov. 2006.

[19] A. Klenner *et al.*, "Gigahertz frequency comb offset stabilization based on supercontinuum generation in silicon nitride waveguides," *Opt. Express*, vol. 24, no. 10, p. 11043, May 2016.

[20] R. Driben, A. V. Yulin, and A. Efimov, "Resonant radiation from oscillating higher order solitons," *Opt. Express*, vol. 23, no. 15, p. 19112, Jul. 2015.

[21] N. Akhmediev and M. Karlsson, "Cherenkov radiation emitted by solitons in optical fibers," *Phys. Rev. A*, vol. 51, no. 3, pp. 2602–2607, Mar. 1995.

[22] L. Chang *et al.*, "Heterogeneous integration of lithium niobate and silicon nitride waveguides for wafer-scale photonic integrated circuits on silicon," *Opt. Lett.*, vol. 42, no. 4, p. 803, 2017.

[23] L. Chang *et al.*, "Heterogeneously integrated GaAs waveguides on insulator for efficient frequency conversion," *Laser Photon. Rev.*, 2018.

Chapter 6

Nonlinear photonic systems

6.1. Background

The area of integrated individual nonlinear devices has seen explosive growth in last few years [1]–[3]. However, system level developments based on nonlinear photonic devices have been very sparse so far. In most cases, the on-chip nonlinear devices are interfaced with fibers [4], to replace traditional nonlinear components in optics systems. Even though the smaller

mode volume and flexibility of engineering the geometry offered by waveguides lead to better performance at device level, the fiber to chip coupling loss, reflection at the facet and the requirement for other bulky equipment takes away almost all the benefits offered by photonic integration.

Some attempts have been made for the integration for nonlinear photonic system by using chip to chip coupling [5], [6]. This approach can, to a certain level, combine various of photonic components together to form nonlinear system based on photonics approach. Beyond that, the (Al)GaAsOI platform we demonstrated in this work provides an ultimate solution for the fully integrated nonlinear PICs in the future.

In this chapter, we will take an important demonstration, optical frequency synthesizers [7], as an example, to show the way to realize the nonlinear system based on integrated photonics. Other applications and opportunities offered by nonlinear photonics as well as the future path to the fully integrated PICs, will also be discussed.

6.2. Optical frequency synthesizer based on integrated photonics

6.2.1 Introduction

The electronics revolution that began in the mid-twentieth century was driven in part by advances related to the synthesis of radio and microwave-frequency signals for applications in radar, navigation and communications systems. This formed a foundation for more recent technologies of wide impact, such as the Global Positioning System and cellular communications. Direct-digital synthesis now operates at >10 GHz rates with watt-scale power. Despite the ubiquity of electronic synthesis, no comparable technology existed for electromagnetic signals in the optical domain until the introduction of the self-referenced optical-frequency comb [8]. An optical-frequency comb can provide the critical phase-

coherent link between microwave and optical domains, with an output consisting of an array of optical modes having frequencies given exactly by $\nu_n = n\ f_{\mathrm{rep}} + f_{\mathrm{ceo}}$, where f_{rep} and f_{ceo} are microwave frequencies and n is an integer. Over the past two decades, optical-frequency synthesizers using mode-locked-laser frequency combs have been demonstrated [9]. The optical-synthesizer output, derived from a reference clock, is invaluable for coherent light detection and ranging, atomic and molecular spectroscopy and optical communications. Optical-frequency-comb technology has also matured so that a typical erbium-fiber comb system requires approximately 2 W of optical pump power [10].

A new opportunity for chip-integrated optical-frequency synthesis has emerged with development in heterogeneously integrated photonics [11] and photonic-chip microresonator frequency combs, or microcombs [12]. Microresonators pumped by a continuous-wave (CW) laser generate a parametric four-wave mixing comb in dielectric media. Relying on waveguide confinement and high nonlinearity of the integrated photonics, microresonators provide a route to comb generation with only milliwatts of input power and high pump-conversion efficiency. Precise waveguide group-velocity dispersion (GVD) control [13], combined with the realization of low-noise dissipative Kerr solitons (DKSs) [14], has led to octave-spanning optical spectra with dispersive waves to enhance the signal-to-noise ratio in microcomb carrier-envelope-offset frequency (f_{ceo}) detection. In parallel, through heterogeneous integration, it has become possible to seamlessly combine active and passive components, such as semiconductor lasers and amplifiers, electro-optic modulators, passive waveguides, photodiodes and complementary metal–oxide–semiconductor (CMOS) electronics on a silicon-chip platform [15], and specifically to implement phase-locking of integrated lasers to microcombs [16]. Our work makes use of Kerr-soliton frequency combs and silicon photonics to realize optical-frequency synthesis derived phase-coherently from an electronic clock.

6.2.2 Experiments

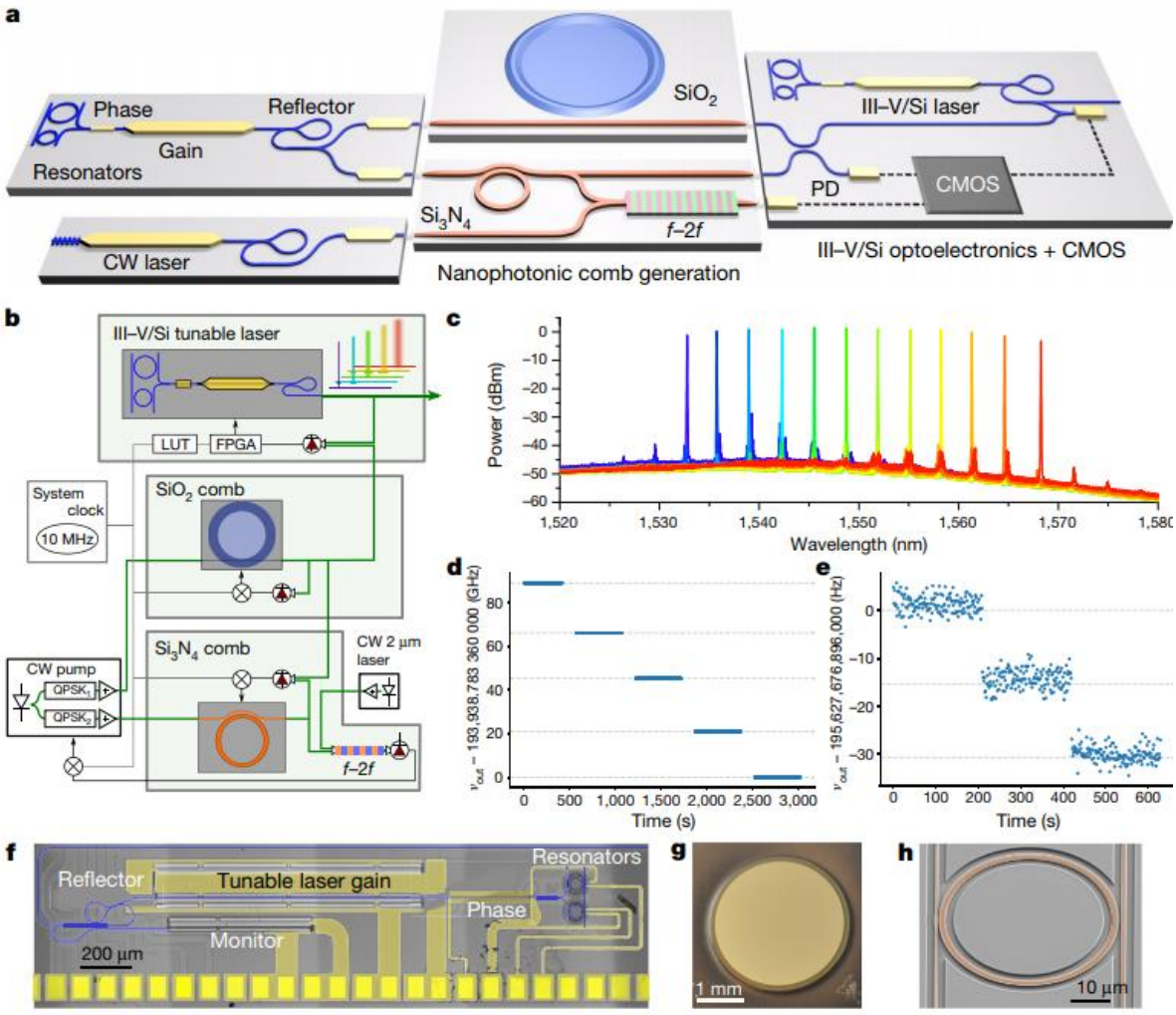

Figure. 6.1: **Accurate optical synthesis with an integrated laser and DKS dual-comb system.** a, Conceptual integrated optical-frequency synthesizer with digital control and f–2 f stabilization, using the microcombs and tunable laser of this work. PD, photodetector. b, Our optical synthesizer is composed of an integrated tunable laser and chip-based Kerr-comb generators. Green boxes indicate the tabletop subsystems including the chips, and how they connect. The CW pumping laser for some experiments is a second integrated laser; see Methods. The tunable laser is synthesized by phase-locking to the stabilized combs, using a look-up table (LUT) and FPGA. QPSK, quadrature phase shift key modulator. c, Optical spectra of the laser across 32 nm. d, e, Measurements of the

synthesizer output as it is stepped. The data indicate the deviation between the synthesizer output vout and its setpoint for mode-hopping across the 22-GHz SiO2 modes (d) and for application of precise frequency steps of 15.36Hz (e). f, Scanning electron microscope (SEM) image of the heterogeneous III–V/Si tunable laser with false colour electrodes (yellow) and waveguides (blue). g, Photograph of the SiO2-based wedge microresonator. h, SEM image of the Si_3N_4 THz resonator with false colour imposed on the waveguide regions.

Mirroring the framework of most traditional optical and microwave synthesizers, our system is composed of a tunable laser oscillator that we phase-lock to a stabilized microcomb reference. Figure 6.1(a) presents the concept of a future integrated synthesizer, and Fig. 6.1(b) indicates the connections between the integrated tunable laser and the chip-based Kerr-comb components that are used in this work. We use the C-band tunability, narrow linewidth and rapid frequency control of a III–V/silicon ring-resonator [11] laser as the synthesizer output, and the phase-coherent microwave-to-optical connection of a fully stabilized DKS frequency comb. The DKS dual comb consists of an octave-bandwidth, silicon nitride comb with 1 THz mode spacing and a C-band-spanning, fused-silica comb with 22 GHz mode spacing. By phase-stabilizing both comb spacings ($f_{\mathrm{rep,THz}}$ and $f_{\mathrm{rep,GHz}}$) and the silicon nitride comb's offset frequency, $f_{\mathrm{ceo,THz}}$, we establish the precise factor of 19,403,904 phase-coherent multiplication from 10 MHz to the optical domain. With this tunable-laser and frequency-comb system, we demonstrate synthesis across a 4-THz segment of the C-band by programming and dynamically stepping the output frequency; see Fig. 6.1(c)-(e). As the role of any synthesizer is to output a phase-coherent multiplied version of the input clock, we characterize the optical synthesizer primarily through its fluctuations with an out-of-loop frequency comb derived from the same clock. A fully integrated synthesizer, realized by

using, improving and connecting the chip components that we describe, would be a powerful tool for many applications.

To demonstrate the optical-frequency synthesizer, we carry out a series of experiments characterizing its output frequency. Standard spectrometer or interferometer measurements readily verify system performance at the megahertz (or 10^{-8}) level. By measuring the synthesizer with an auxiliary self-referenced erbium-fiber comb, we constrain the frequency error between the output and the synthesizer's setpoint to <1.5 Hz. Beyond demonstration of the integrated-photonics architecture, the core result of our work is verification that the synthesizer offers sufficient phase control and synchronization in microwave-to-optical conversion (as do the auxiliary comb and our frequency-counting electronics) to reveal a stable phase correlation between the CW output and the radiofrequency (RF) clock. Hence, the statistical fluctuations that lead to the synthesizer's instability, and our measurement of these, offer the complete description of the synthesizer's frequency performance.

The chip-based integrated components of the synthesizer—the tunable laser (Fig. 6.1(f)) and DKS frequency combs (Fig. 6.1(g) and (h))—and their key connections with non-integrated components are emphasized in Fig. 6.1(b). An external cavity pump laser is used to generate both of the DKS combs, using independent control with single-sideband frequency shifters and erbium amplification for each comb. An octave-spanning single-pulse soliton is generated in a Si_3N_4 planar waveguide-coupled resonator. In addition to the anomalous GVD profile, waveguide-dispersion engineering creates dispersive-wave peaks in optical power that appear at 999 nm and 2,190 nm, owing to the zero-integrated GVD starting from the pump wavelength. With a radius of 23 μm, the threshold for octave-spanning spectra is brought to below 50 mW of on-chip pump power, at the expense of a $f_{\mathrm{rep,THz}}$ of 1.014 THz that cannot be easily photodetected and reduced to a microwave

frequency with conventional electronics. Rather, we rely on a second frequency comb to bridge the gap between Si_3N_4 THz comb modes.

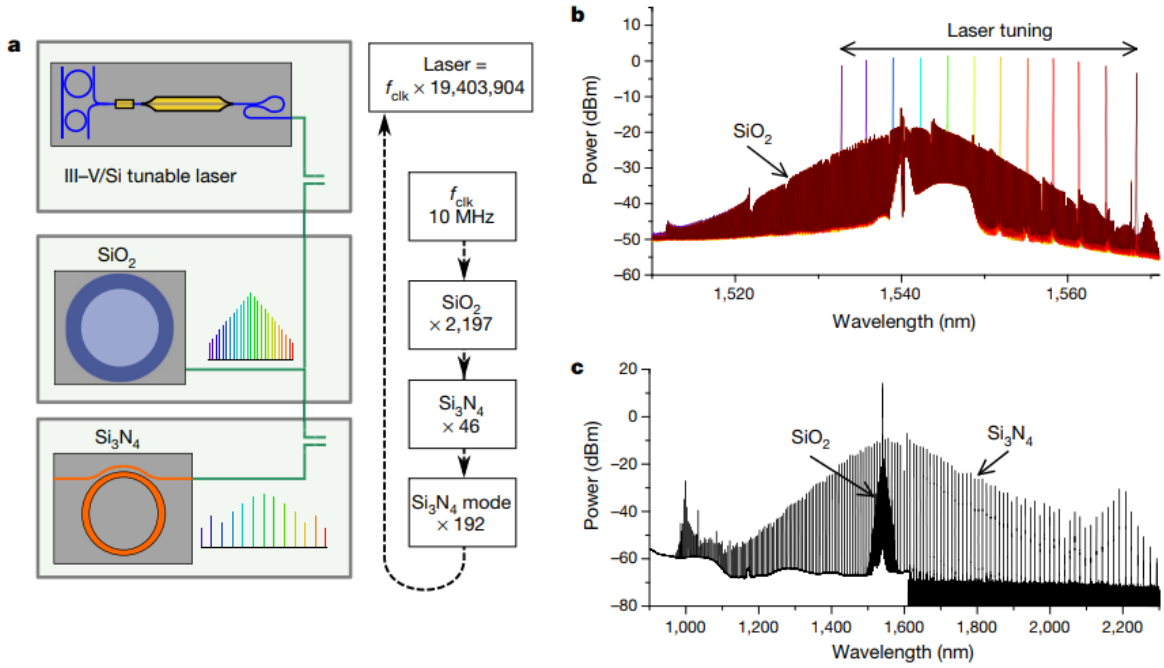

Figure. 6.2: **Optical spectra of the integrated devices.** a, Schematic diagram of spectral combination with the integrated devices, and the frequency chain used to multiply the 10-MHz clock to the optical domain. b, Combined spectrum of the SiO_2 22-GHz wedge microcomb and the heterogeneously integrated iii–v/Si tunable laser in the telecommunication C-band. c, Combined spectrum of the octave-spanning Si_3N_4 THz microcomb and the 22-GHz SiO2 wedge microcomb, as measured on two optical spectrum analysers.

To do this, an SiO_2 wedge-based whispering-gallery-mode resonator with a quality factor (Q) of 180 million is used to create a DKS frequency comb at $f_{rep,GHz} \approx 22$ GHz (ref. [17]). As the threshold for soliton-comb generation scales inversely to both the repetition rate and Q^2, use of a SiO_2 device is important for low-power operation. The repetition frequency of 22 GHz is photodetected and phase-locked to the RF clock. This first step in the microwave-

to-optical frequency chain (Fig. 6.2(a)) from $f_{clk} = 10$ MHz to 22 GHz partially stabilizes the SiO_2 reference comb to guide tunable laser synthesis; see Fig. 6.2(b). The second step is detection of the 1.014 THz frequency spacing between Si_3N_4 comb teeth, which we accomplish using the 46th relative comb line from the SiO_2 comb. Operationally, we measure $f_{rep,THz}$ by detecting the optical heterodyne beat note between the two combs 1 THz away from the pump. We phase-lock this signal to a synthesized radiofrequency, $f_1 = \alpha f_{clk}$ (where α is the ratio of two integers), after removing the relative contributions from the single-sideband frequency shifters and feeding back to the frequency of the Si_3N_4 pump laser. Thus, we stabilize $f_{rep,THz}$ and transfer the f_{clk} stability to 1.014 THz. The frequency of each of the Si_3N_4 THz comb lines with negative offset frequency and mode number $N = 192$ is then given by:

$$\begin{aligned} \nu_{THz} &= N f_{rep,THz} - f_{ceo,THz} \\ \nu_{THz,pump} &= 192(46 f_{rep,GHz} + \alpha f_{clk}) - f_{ceo,THz} \end{aligned} \tag{6.2.1}$$

Next, $f_{ceo,THz}$ locking is achieved by using the octave-spanning relationship of the THz lines at 1,998 nm and dispersive wave peak at 999 nm (Fig. 6.2(c)). To aid *f–2f* self-referencing (which enables determination of the absolute frequency of each comb line), an independent diode laser and thulium-doped fiber amplifier at 1,998 nm supply 9 mW to a PPLN waveguide device to achieve 34 dB signal-to-noise ratio (SNR) on $f_{ceo,THz}$. Similar monolithic second-harmonic generation and amplifier technologies have been demonstrated and could be integrated with our system. After detecting two heterodyne beats with the THz comb, f_{999} and f_{1998}, each beat note is digitally divided by 64 and 32, respectively, and frequency mixing yields an $f_{ceo,THz}$ signal, $f_{ceo,THz}/64 = f_{999}/64 - f_{1998}/32$. Phase-locking this signal to a radiofrequency $f_2 = \beta f_{clk}$, through feedback to the Si_3N_4 pump power, completes the transfer of stability from f_{clk} to all the THz comb lines spanning 130 THz to 300 THz.

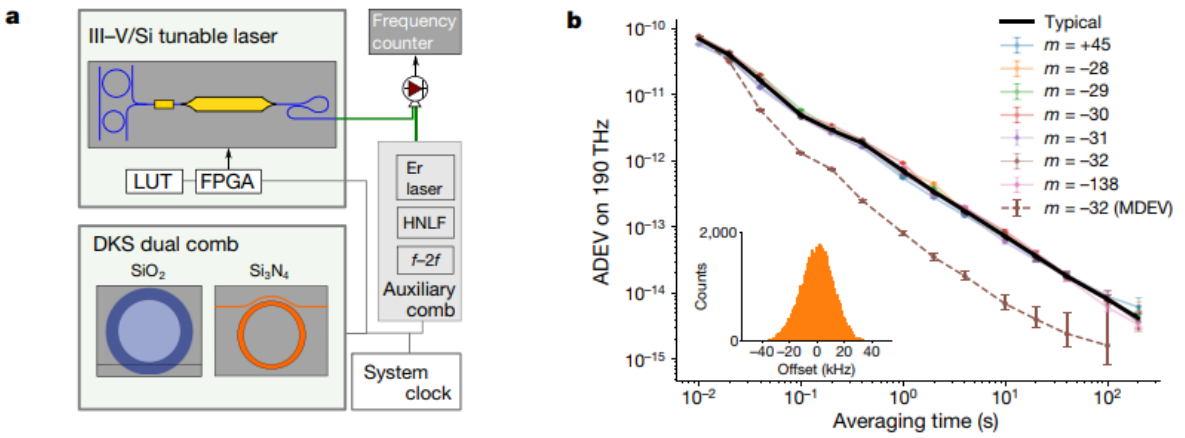

m	Approx. λ (nm)	Nominal frequency (Hz)	Uncertainty$_{200\,s}$
+45	1,532.46	195,627,803,557,000	6.2×10^{-15}
−28	1,545.10	194,027,822,248,000	3.9×10^{-15}
−29	1,545.28	194,004,949,561,000	4.6×10^{-15}
−30	1,545.45	193,984,168,686,000	3.9×10^{-15}
−31	1,545.64	193,959,801,079,000	3.6×10^{-15}
−32	1,545.81	193,938,783,360,000	3.7×10^{-15}
−138	1,564.72	191,594,676,255,000	3.3×10^{-15}

Figure. 6.3: **Stable optical synthesis with out-of-loop verification.** a, Tunable laser locking, and frequency counting with the auxiliary comb. HNLF, highly nonlinear fibre. b, Measured overlapping Allan deviation (ADEV) and modified Allan deviation (MDEV) of the frequency synthesizer. In comparing 10-ms counter-gate time acquisitions, the 1/τ slope is consistent with a stable, phase-locked synthesizer, and the histograms of 500 s of data (inset for relative mode m=−28 only) show a Gaussian profile. Error bars indicating 95% confidence intervals are derived using flicker noise estimates. c, Table of nominal frequencies and uncertainty at 200 s as the synthesizer is stepped across the C-band. d, Overview of the accuracy and precision of the synthesizer frequency. The ADEV at 100 s is used to estimate the uncertainty of each synthesizer output, and the weighted mean of the seven data points is reported with a 95% (*t* distribution) confidence interval.

The dual-stabilized combs serve as the backbone to guide the heterogeneously integrated III–V/Si tunable laser for arbitrary optical-frequency synthesis across the

C-band. The tunable laser consists of InGaAsP multiple-quantum-well epitaxial material that is wafer-bonded onto a lithographically patterned silicon-on-insulator wafer. Bias heaters integrated on the laser's Si-based resonant reflectors and phase section are used to shift the lasing wavelength for initial alignment to the comb lines. By using Si waveguides that have low loss relative to standard telecommunication-grade InP waveguide technology, reduced linewidths of about 300 kHz are achieved. The combined optical spectrum of the SiO_2 comb and integrated laser's tuning range is shown in Fig. 6.2(b). Heterodyning with the DKS dual-comb signal at a relative mode *m* from the pump creates a signal, f_{beat}^{laser}, for input to a field-programmable gate array (FPGA)-based phased-locked-loop (PLL, Fig. 6.3(a)) with a local oscillator of $f_3 = \gamma f_{clk}$, and digital division of 512. This final laser lock to the DKS dual comb produces a fully stabilized, tunable synthesizer output,

$$\begin{aligned} \nu_{out} &= \nu_{THz,pump} + m f_{rep,GHz} + f_{beat}^{laser} \\ &= f_{clk}[192(46\times 2{,}197+\alpha) + 2197m - 64\beta + 512\gamma] \end{aligned} \tag{6.2.2}$$

This expression shows that the output of our integrated-photonics synthesizer is uniquely and precisely defined relative to the input clock frequency in terms of user-chosen integers and ratios of integers (α, β, γ).

Agile tuning across SiO_2 comb lines (varying *m*) and hertz-level tuning resolution on the same comb line (varying γ) have already been presented in Fig. 6.2(b) and Fig. 6.1(c), demonstrating synthesizer operation. To explore our synthesizer's phase coherence, we perform an out-of-loop optical-frequency characterization by heterodyning ν_{out} against an auxiliary erbium-fiber laser frequency comb that is fully

stabilized to the same f_{clk}. Fig. 6.3 shows results from a study of the tunability and phase-locked operation of the synthesizer across all comb frequencies by locking to five adjacent SiO_2 comb lines, and to the highest and lowest wavelengths of the laser tuning range. Overlapping Allan deviation (ADEV) analysis of the counted beat notes against the auxiliary comb show the instability improving as $<10^{-12}/\tau$ for all recorded averaging times τ, and reaching an average instability of $(4.2 \pm 0.4) \times 10^{-15}$ at 200 s (Fig. 6.3(b),(c)). More sophisticated triangular averaging analysis using the modified Allan deviation (MDEV) yields an order of magnitude better instability of $(9.2 \pm 1.4) \times 10^{-14}$ at 1 s. Still, the $1/\tau$ dependence of the ADEV data, which characterizes the fluctuations of the optical-frequency synthesizer, indicates the stable phase relationship between the RF clock and the synthesized optical frequencies. Moreover, the synthesizer performance is consistent with the hydrogen-maser RF clock used in the experiments, indicating that our phase locks of the tunable laser, the Kerr combs and the auxiliary erbium-fiber comb contribute negligible noise. This is the most fundamental metric of an optical synthesizer. From the mean values of the measured beats with the auxiliary comb, we can further analyze potential deviations of the synthesizer output from equation (6.2.2). Data compiled from the seven experiments are shown in Fig. 6.3(d) with 100-s ADEV error bars plotted, and the weighted mean of all data sets with a 95% confidence interval is (1.2 ± 1.5) Hz. Thus, based on these initial data, we conclude that our integrated-photonics optical synthesizer accurately reproduces the input clock

reference within an uncertainty of 7.7×10^{-15}, competitive with commercial optical synthesizers (5×10^{-13} instability at 1 s and accurate to 10^{-14} at 120 s).

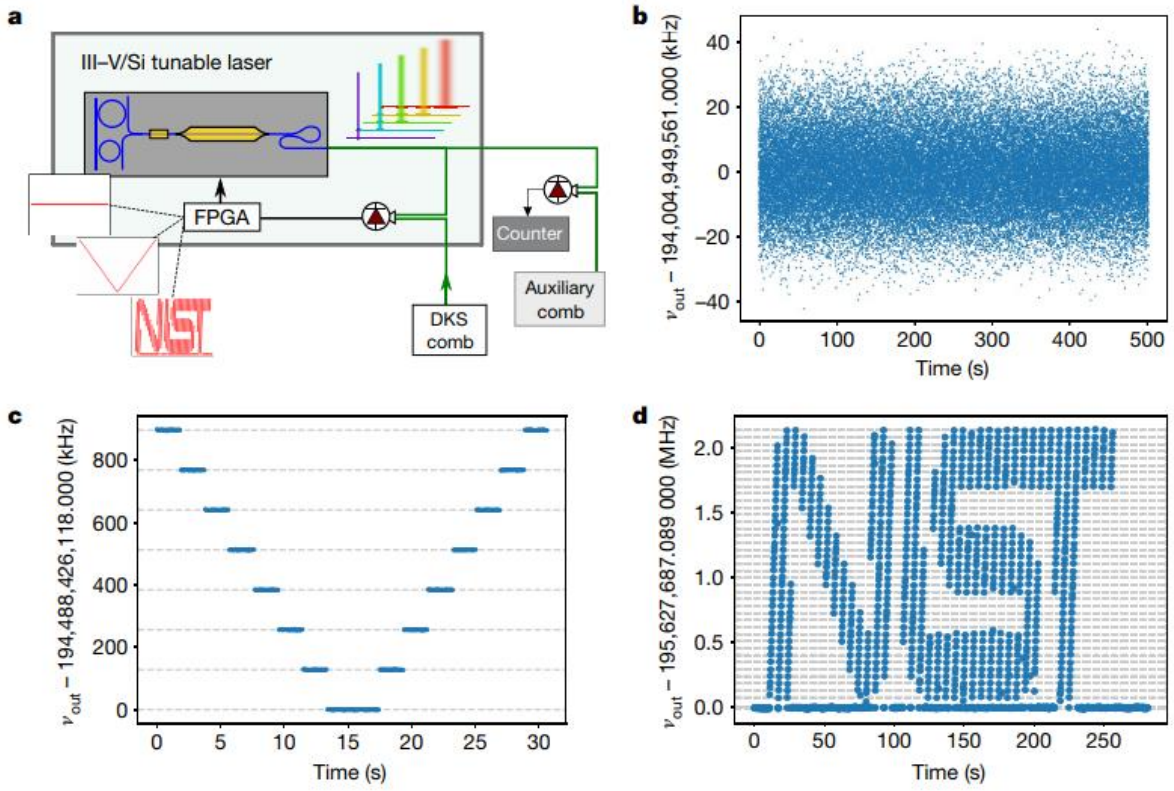

Figure. 6.4: **Arbitrary control of the optical-frequency synthesizer.** a, Stepwise control of the tunable-laser offset phase-lock to the DKS comb and frequency counting. b, Deviation between the synthesizer output vout and constant setpoint for 500 s at a 10-ms gate time. c, Bidirectional linear ramp of the synthesizer via step control of the laser offset PLL setpoint (100-ms gate). d, Arbitrary frequency control of the synthesizer across 40 frequency setpoints to write "NIST". A 30-ms gate time is used to oversample each frequency setpoint by 5 (150-ms pause per point), and every fifth data point is displayed.

To demonstrate the tunability of the optical-frequency synthesizer, we perform two different types of tuning while the laser is locked to the stabilized comb system

(Fig. 6.4). As a baseline, without changing the setpoint of the tunable laser phase-lock, the raw data of the counted auxiliary comb beat note are shown in Fig. 6.4(b) after subtraction of the nominally expected frequency for 500 s. We then apply a bidirectional linear ramp over eight levels with a 2-s pause at each level to ensure successful locking (Fig. 6.4(c)). Finally, we programed a series of setpoint frequencies to the FPGA PLL box to write out the National Institute of Standards and Technology (NIST) logo (Fig. 6.4(d)). Excellent agreement is found between the expected offset frequencies and the counted beat-note frequencies for all cases, illustrating good dynamic control of the synthesizer.

In summary, the experiments that we present, performed with an optical-frequency synthesizer constructed from integrated photonics, demonstrate that this technology has achieved the high precision and accuracy that formerly has been confined to tabletop mode-locked laser frequency-comb devices. For further integration of the laser and Kerr combs used in our experiments, targeted improvements should be made to increase microresonator Q for lower-power operation, to improve the intensity of the Si_3N_4 comb dispersive waves for f–$2f$ stabilization, and to improve the efficiency of second-harmonic generation, guided by the applications that are envisaged for the device.

6.2.3 Devices

The heterogeneously integrated III–V/Si device includes a tunable laser and a semiconductor optical amplifier (SOA). At room temperature, the laser emits up to 4 mW CW power, and the SOA provides an on-chip small-signal gain >10 dB. The

laser contains a gain section, a phase section and two microresonators designed for high quality factor. The gain section and the SOA consist of electrically pumped InP-based quantum wells heterogeneously integrated on a Si waveguide. Thermal heating of the Si microresonators and passive phase section is performed with current injection to metal heaters above the waveguides. By intentionally mismatching the radii of the microresonators to make use of the Vernier effect, we can use a narrowband intracavity optical filter to select the desired longitudinal mode for lasing with high side-mode suppression ratio. Precise wavelength tuning and linewidth narrowing is performed by heating the phase section. Phase-locking of the laser to the microcomb is performed by electronically dividing the beat note by 512 and using FPGA-based digital PLL + PI^2D feedback (that is, a proportional–integral–derivative controller with two-stage integration) to the gain section of the laser. Other works have also demonstrated high-bandwidth optical-PLL phase locks to frequency combs. In the current system, the tunable laser can lock to either the SiO_2 or Si_3N_4comb lines, which we have shown for $m = -138$, or 3 THz red of the pump laser. The DC linear tuning coefficient of the tunable laser is approximately 200 MHz mA^{-1}.

A commercial external cavity diode laser is used as the shared pump for both microresonator comb generators in all the synthesizer experiments. The output of a 3-dB splitter goes to separate $LiNbO_3$single-sideband modulators and erbium-doped fibre amplifiers for each device. Frequency detuning from each microcomb resonance for soliton generation is controlled with an amplified voltage-controlled oscillator and arbitrary waveform generator that produces a voltage ramp. Although complex

soliton crystals can form in these devices, single solitons are generated through linear voltage ramps of 5 GHz in 100 ns and 100 MHz in 3 μs, for the Si_3N_4 and SiO_2 microcombs, respectively. Once initiated, feedback to each voltage-controlled oscillator controls $f_{rep,GHz}$ and $f_{rep,THz}$ for the appropriate device. Intensity modulation on the Si_3N_4 microcomb to control $f_{ceo,THz}$ is performed with a free-space acousto-optic modulator, although on-chip SOAs are expected to be viable as well. Lensed fibres with a 2.5-μm spot size are used to couple light on and off the Si_3N_4 chip with 7 dB of insertion loss per facet. During operation, the on-chip pump power for the Si_3N_4 microcomb is about 160 mW, or ten times the threshold for soliton generation. Tapered single-mode fibre is used to couple 80 mW to the SiO_2microcomb for soliton generation at 12 times the soliton threshold. Recent results show that this platform can be integrated with Si_3N_4 bus waveguides. An offset Pound–Drever–Hall lock is required after ramping to keep the SiO_2 pump frequency at 22 MHz red detuned from resonance.

During operation of the optical-frequency synthesizer, the separate single-sideband modulators for each microcomb device create a detectable offset in pump frequencies, about 5 GHz in our experiment. This is readily subtracted from or added to the necessary heterodyne beat notes in the system using an electronic frequency mixer, specifically after $f_{rep,THz}$ detection between comb lines and after the III–V/Si laser heterodyne with the DKS comb. The calibrated gain sign of the tunable-laser feedback loop ensures that the tunable laser is on the appropriate side of the SiO_2 comb modes when electronically subtracting or adding this offset, and

knowledge of the absolute difference in pump frequencies is not required for accurate optical-frequency synthesis. We observe non-zero synthesis error when the SNR of any heterodyne beat falls well below the optimal level of 30 dB, but measurements reported here were acquired with sufficient SNR. We also observe and minimize contributions from out-of-loop optical and electrical path lengths, alignment drift, and glitches during long acquisitions. The RF synthesis and phase-locking electronics used in the experiments are benchtop scale, but in the future would make use of CMOS integration.

The auxiliary comb used for out-of-loop verification of the optical-frequency synthesizer consists of a 250-MHz erbium-fibre mode-locked laser frequency comb. The laser output is amplified and spectrally broadened to an octave to enable self-referenced detection of the carrier envelope offset frequency, f_{ceo}. The fourth harmonic of f_{rep} is phase-locked to a reference synthesizer at 999.999 544 MHz, and f_{ceo} is electronically divided by 8 and phase-locked to another synthesizer at 20 MHz. Both of these synthesizers are referenced to the same f_{clk} that is the input to the integrated-photonics synthesizer, yielding a comb against which any frequency of the microcomb or tunable laser output can be compared.

The beat-note frequency between the integrated-photonics synthesizer and the erbium-fibre frequency comb is amplified and bandpass-filtered (45 MHz bandwidth), after which a zero-dead-time frequency counter registers the frequency for a fixed gate time. The rectangular binning, or Π-mode, is used during measurement and for the ADEV analysis. The MDEV analysis applies a triangular

averaging window to the frequency data for further information on the noise type. With this analysis, a $\tau^{2/3}$ slope shows the desired white phase noise performance, and deviation from this slope reveals unwanted flicker phase noise contributes to system performance at longer averaging times. Because the degrees of freedom depend on noise type, we take the conservative estimate of flicker phase noise to derive 95% confidence intervals. The tunable laser PLL also contains an in-loop frequency counter, which showed tight phase-locking of the laser to the microcomb at $<10^{-13}/\tau$, limited by the resolution of the counter. All RF synthesizers in the experimental set-up, auxiliary comb and frequency counter are tied to the same hydrogen maser signal, serving as f_{clk}.

6.2.4 Integration of the system

Even though the system level demonstration discussed above, which is using fibers to interface different components, delivered state of the art performance of optical frequency synthesizing. The scale of it is still relative large, with a high power consumption. A more compact version, without relying on extra bulky equipment, will be essential to reduce the size and cost. Here by levering the heterogeneous nonlinear photonics technology as we discussed in Chapter 5, the chip combing the Si_3N_4 THz comb source, SHG waveguide and the interposer Si_3N_4 passive circuits for wavelength filtering and mixing have been demonstrated, which is shown in Fig. 6.5 (b). Then by packaging all the optical chips and electrical components together, a system with all the functionalities of an optical synthesizer can be integrated in a package which is smaller than 1 cm^3, shown in Fig. 6.5 (c). This demonstration projects to reduce the footprint and power consumption by 1000X.

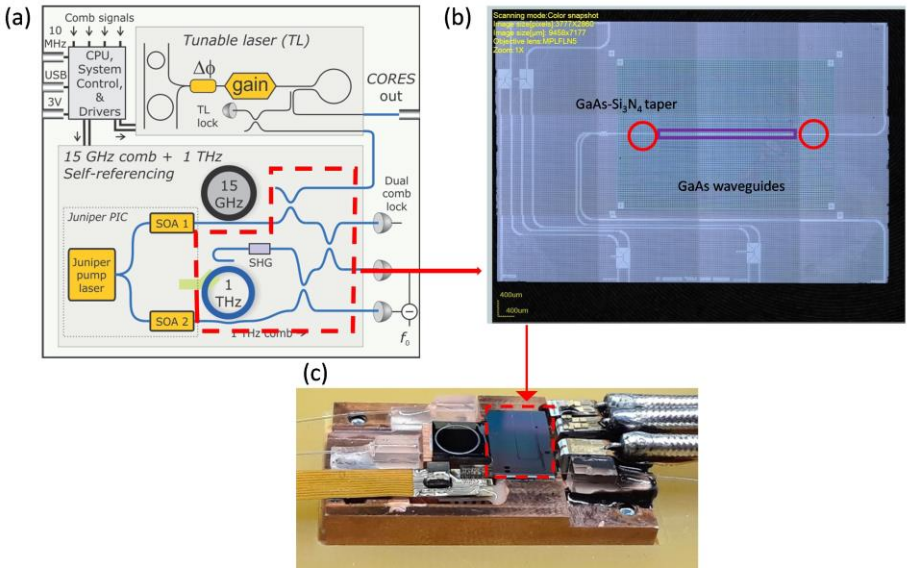

Figure. 6.5: **Integration of an optical frequency synthesizer.** (a) Schematic drawing of the system; (b) Interposer chip combing multi photonic components together; (c) A compact optical frequency synthesizer in a package.

6.3 Other nonlinear photonic systems

Besides the optical frequency synthesizer, integrated nonlinear photonics can also lead to many other system level demonstrations, which project to revolutionize almost every area of photonics. For example, in communication, one micro-resonator on chip for frequency comb generation can replace thousands of parallel lasers and thus improve the system energy efficiency [18]. Thus it can enable the massively parallel coherent communications. In optical metrology, two frequency combs with slightly different FSR can be used for dual-comb spectroscopy [4], doing measurements in both near and mid-infrared directly on chip, by converting the long wavelength signals to RF ones in photodetectors. Furthermore, similar as the approach we used for frequency synthesizers, a fully integrated atomic clock on chip can

also be enabled by locking the optical frequency to reference and synthesize a radio frequency [19].

6.4 Summary and outlook

Even though the future for nonlinear photonic systems is very promising, many difficulties need to be overcome beforehand. Packaging based on chip to chip and chip to fiber coupling provide a solution in certain circumstances to assemble all the components together, but it is limited by the cost and scalability. Especially for complex systems requiring multi-chips, the extra loss and instability introduced by facets will significantly reduce the system's performance.

Heterogeneous nonlinear photonics is the most promising way to address those problems. Specifically, as we discussed in Chapter 4, the most challenging part for nonlinear photonics integration, which is to bridge the active devices with nonlinear components, can be achieved in our (Al)GaAsOI platform. A future development of the integrated laser in this platform will be the next essential step. Finally, we expect the nonlinear PICs to be realized on a single chip, which will greatly reduce the scale, cost and power consumption of current nonlinear system, and open up many new opportunities in academia and industry.

Reference

[1] T. Herr, M. L. Gorodetsky, and T. J. Kippenberg, "Dissipative Kerr solitons in optical microresonators."

[2] L. Chang, Y. Li, N. Volet, L. Wang, J. Peters, and J. E. Bowers, "Thin film

wavelength converters for photonic integrated circuits," *Optica*, vol. 3, no. 5, p. 531, 2016.

[3] N. T. Otterstrom, R. O. Behunin, E. A. Kittlaus, Z. Wang, and P. T. Rakich, "A silicon Brillouin laser.," *Science*, vol. 360, no. 6393, pp. 1113–1116, Jun. 2018.

[4] I. Coddington, N. Newbury, and W. Swann, "Dual-comb spectroscopy," *Optica*, vol. 3, no. 4, p. 414, Apr. 2016.

[5] B. Stern, X. Ji, Y. Okawachi, A. L. Gaeta, and M. Lipson, "Battery-operated integrated frequency comb generator," *Nature*, vol. 562, no. 7727, pp. 401–405, Oct. 2018.

[6] A. S. Raja *et al.*, "Electrically pumped photonic integrated soliton microcomb," *Nat. Commun.*, vol. 10, no. 1, p. 680, Dec. 2019.

[7] D. T. Spencer *et al.*, "An optical-frequency synthesizer using integrated photonics," *Nature*, vol. 557, no. 7703, pp. 81–85, 2018.

[8] J. L. Hall, "Nobel Lecture: Defining and measuring optical frequencies," *Rev. Mod. Phys.*, vol. 78, no. 4, pp. 1279–1295, Nov. 2006.

[9] J. Jost, J. Hall, and J. Ye, "Continuously tunable, precise, single frequency

optical signal generator," *Opt. Express*, vol. 10, no. 12, p. 515, Jun. 2002.

[10] L. C. Sinclair *et al.*, "Operation of an optically coherent frequency comb outside the metrology lab," *Opt. Express*, vol. 22, no. 6, p. 6996, Mar. 2014.

[11] T. Komljenovic *et al.*, "Heterogeneous Silicon Photonic Integrated Circuits," *J. Light. Technol.*, vol. 34, no. 1, pp. 1–1, 2015.

[12] A. L. Gaeta, M. Lipson, and T. J. Kippenberg, "Photonic-chip-based frequency combs," *Nat. Photonics*, vol. 13, no. 3, pp. 158–169, Mar. 2019.

[13] Y. Okawachi *et al.*, "Bandwidth shaping of microresonator-based frequency combs via dispersion engineering," *Opt. Lett.*, vol. 39, no. 12, p. 3535, Jun. 2014.

[14] R. Summary, "Dissipative Kerr solitons in optical microresonators," *Science (80-.).*, vol. 8083, 2018.

[15] D. J. Moss, R. Morandotti, A. L. Gaeta, and M. Lipson, "New CMOS-compatible platforms based on silicon nitride and Hydex for nonlinear optics," *Nat. Photonics*, vol. 7, no. 8, pp. 597–607, Aug. 2013.

[16] S. Arafin *et al.*, "Power-Efficient Kerr Frequency Comb Based Tunable Optical Source," *IEEE Photonics J.*, vol. 9, no. 3, pp. 1–14, Jun. 2017.

[17] X. Yi, Q.-F. Yang, K. Y. Yang, M.-G. Suh, and K. Vahala, “Soliton frequency comb at microwave rates in a high-Q silica microresonator,” *Optica*, vol. 2, no. 12, p. 1078, Dec. 2015.

[18] P. Marin-Palomo *et al.*, “Microresonator-based solitons for massively parallel coherent optical communications,” *Nature*, vol. 546, no. 7657, pp. 274–279, Jun. 2017.

[19] Z. L. Newman *et al.*, “Photonic integration of an optical atomic clock,” Nov. 2018.

Chapter 7

Conclusions

7.1. Review

This dissertation outlines the successful demonstration of state of the art nonlinear photonic platforms by heterogeneous nonlinear photonics technology. Based on those platforms, multi nonlinear devices covering both second and third order nonlinear processes, have been developed with record high efficiencies.

In heterogeneous lithium niobate on insulator platform, the hybrid SiN-LNOI waveguides enabled, for the first time, low propagation loss (<0.3 dB/cm) of thin film LN waveguide, which is similar or even lower compared to those of previous bulky LN waveguides. Such waveguide has sub-micron scale mode volume, which provides great potential for high efficient nonlinear and modulation applications. Moreover, we developed the first periodic poling method for thin film LN and constructed the first thin film PPLN waveguide, whose normalized SHG efficiency is up to 780 $\%W^{-1}cm^{-2}$, more than one order of magnitude higher than those of previous PPLN devices.

The heterogeneous (Aluminum) Gallium Arsenide on insulator platform, provides ultra-high efficient and fully integration compatible solutions for future nonlinear PICs and quantum photonic circuits. The waveguides on this platform exhibit the record high SHG

normalized efficiency beyond 13,000%W^{-1}, and the SHG resonators shows ultra-high internal conversion efficiency around 65,000%W^{-1}. After optimization of our fabrication, fully etched AlGaAs nanowire resonator exhibits a high Q up to 1 million, which leads to a low threshold power for frequency comb generation about 220 μW.

With the heterogeneous integration technology, LNOI and (Al)GaAsOI have also been successfully integrated onto high quality Si_3N_4 chip, which not only have high-Q resonator for frequency comb generation and waveguides for supercontinuum generation, but also leverage the mature CMOS compatible technology for building the whole PICs. The taper bridging Si_3N_4 waveguides and highly nonlinear materials show very efficient mode transition (< 1 dB/taper), which pose a promising approach to add nonlinear and active devices into the CMOS compatible nonlinear systems.

In system level, based on nonlinear photonics devices, our team demonstrated a system to synthesize the absolute frequency of a lightwave signal. The laser frequency output of our synthesizer is programmed by a microwave clock across 4 THz near 1550 nm with 1 Hz resolution. The synthesizer is exceptionally stable with a synthesis error of 7.7×10^{-15} or below across the telecommunication C-band. Many applications of optical-frequency sources could benefit from the high-precision optical synthesis presented here. Leveraging high-volume semiconductor processing built around advanced materials could allow such low-cost, low-power and compact integrated-photonics devices to be widely used.

7.2. Perspective

The efficient nonlinear processes demonstrated on those heterogeneous platforms, will greatly relieve the power requirements for nonlinear system when directly pumped by on-chip lasers in the future. Even at sub-milliwatt region, a significant amount of power can be

converted from pump to other wavelengths. In the meanwhile, the great flexibility of the phase match and dispersion engineering, offered by the high index contrast and the small mode sizes, enables the generation of extremely wide spectrum range covering from visible to mid-IR on one platform.

Particularly, the (Al)GaAsOI platform, paves the way to revolutionary fully integrated nonlinear PICs in the future, which will accommodate the state of the art nonlinear devices, along with lasers, amplifiers, modulators, photodetectors and other photonic components on the same chip. The nonlinear components will be used for a wide range of nonlinear optical processes, including frequency comb generations, SHG, OPO, as well as opto-mechanical applications. The nonlinear PICs will not only miniaturize optical systems from bench scale setups to single chip level for a wide range of applications, e.g. the quantum computation and communication, classic telecommunication, spectroscopy, metrology and others, but they will also lead to a leap in efficiencies and performances of nonlinear devices. Key to this approach is the use of heterogeneous and/or epitaxial integration of III-V semiconductors to combine the best elements of the nonlinear photonic system. Specifically the integrated quantum well (QW) or quantum dots (QD) on the nonlinear waveguide layer can be used for building strong pump lasers, single photon emitters, amplifiers, and photodetectors. As such, the fully integrated photonic chip combines fundamental research with intelligent selection of breakthrough technologies to provide revolutionary performance in a variety of nonlinear systems.

Furthermore, the technology originated from our work will also benefit many other areas besides nonlinear photonics. In traditionally III-V based PICs, our low loss III-V waveguides with high index contrast can greatly improve the performance of many components, e.g. the narrow linewidth lasers and photonic buffer devices. The high Q resonators and strong

nonlinear properties will also enable studies of nonlinear optics in extreme regimes, which will be used for generation and processing of quantum information by extreme nonlinearities.